Chem Soc Rev

REVIEW ARTICLE

View Article Online
View Journal | View Issue

Cite this: *Chem. Soc. Rev.*, 2020, **49**, 3005

Nanoporous carbon for electrochemical capacitive energy storage

Hui Shao,†[ab] Yih-Chyng Wu,†[ab] Zifeng Lin,*[c] Pierre-Louis Taberna[ab] and Patrice Simon*[abd]

The urgent need for efficient energy storage devices has stimulated a great deal of research on electrochemical double layer capacitors (EDLCs). This review aims at summarizing the recent progress in nanoporous carbons, as the most commonly used EDLC electrode materials in the field of capacitive energy storage, from the viewpoint of materials science and characterization techniques. We discuss the key advances in the fundamental understanding of the charge storage mechanism in nanoporous carbon-based electrodes, including the double layer formation in confined nanopores. Special attention will be also paid to the important development of advanced *in situ* analytical techniques as well as theoretical studies to better understand the carbon pore structure, electrolyte ion environment and ion fluxes in these confined pores. We also highlight the recent progress in advanced electrolytes for EDLCs. The better understanding of the charge storage mechanism of nanoporous carbon-based electrodes and the rational design of electrolytes should shed light on developing the next-generation of EDLCs.

Received 22nd January 2020

DOI: 10.1039/d0cs00059k

rsc.li/chem-soc-rev

1. Introduction

Reducing the consumption of fossil fuels and developing renewable and sustainable energy sources have been considered to be effective strategies to tackle the climate change crisis. To address such issues, more efficient electrical energy conversion and storage devices are required.[1] The most commonly used electrochemical energy storage technologies today are batteries and supercapacitors. Batteries store energy through

[a] *Université Paul Sabatier, CIRIMAT UMR CNRS 5085, 118 route de Narbonne, 31062 Toulouse, France. E-mail: simon@chimie.ups-tlse.fr*
[b] *Réseau sur le Stockage Electrochimique de l'Energie (RS2E), FR CNRS 3459, France*
[c] *College of Materials Science and Engineering, Sichuan University, Chengdu 610065, P. R. China. E-mail: linzifeng@scu.edu.cn*
[d] *Institut Universitaire de France, 1, Rue des Ecoles, 75005 Paris, France*
† These authors contributed equally to this work.

Hui Shao

Hui Shao is currently a PhD candidate in CIRIMAT, Université Paul Sabatier (Toulouse, France), under the supervision of Prof. Patrice Simon and Dr Pierre-Louis Taberna. His work is mainly focused on developing new materials for energy storage applications, including carbon materials, 2D MXenes, and nanostructure materials. He is also interested in the electrochemical principles of supercapacitor systems.

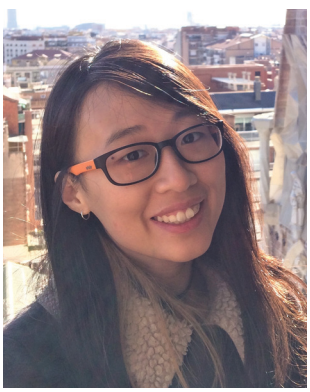

Yih-Chyng Wu

Yih-Chyng Wu received her dual BS degree in Chemical Engineering from National Taiwan University of Science and Technology and Katholieke Universiteit Leuven. She joined the Erasmus Mundus Joint Master Degree in Materials Science and Electrochemistry. Currently, she is a PhD candidate in CIRIMAT, Université Paul Sabatier (Toulouse, France) under the supervision of Prof. Patrice Simon and Dr Pierre-Louis Taberna. Her research work is focused on manipulating the electrochemical quartz crystal microbalance and other electrochemical related techniques to study the interfaces between electrolytes and electrode materials and the charge storage mechanisms of energy storage materials.

faradaic reactions of electrode materials with electrolytes, usually along with chemical interconversions and phase changes, providing high energy supplement, with energy densities of a few hundreds of W h kg^{-1}. However, these battery-type faradaic reactions undergo sluggish kinetics and material irreversible processes, leading to limited power performance and lifetime.[2] By contrast, supercapacitors store the charge at the electrode/electrolyte interface, *via* physical ion adsorption/desorption process, for electrochemical double-layer capacitors (EDLCs); through fast and non-diffusion limited faradaic reactions for pseudocapacitive materials.[3,4] These fast and highly reversible storage mechanisms make supercapacitors promising candidates for energy storage devices with high power density and a long cycling life,[5] which are nowadays used in a broad range of applications where high power delivery and/or uptake is needed, such as energy harvesting.[6,7] However, the energy density ($\sim$10 W h kg^{-1} for the best commercial devices) still hampers the spread of this technology over a wider range of applications.

Zifeng Lin

Zifeng Lin received his PhD degree from the Université Paul Sabatier (Toulouse, France) in 2017, under the supervision of Prof. Patrice Simon and Dr Pierre-Louis Taberna. After a year's postdoctoral research training in the same group, he joined Sichuan University (China) in 2018 as a Research Fellow (PI). His research interests are in the area of nanostructured materials for energy storage devices including electrochemical capacitors and metal ion batteries.

1.1 Basic operating principles of EDLCs

As mentioned above, EDLCs are capacitive energy storage devices that store energy through a non-faradaic mechanism. Like batteries, a supercapacitor device contains two electrodes immersed in an electrolyte (see Fig. 1), with an ionically conducting, porous separator placed in-between to prevent electrical short circuits. Basically, when an external voltage is applied between the EDLC electrodes, the electronic charge that accumulates at electrode surfaces is balanced by the adsorption of the ions of opposite ionic charge from the electrolyte. The capacitance C created by this charge separation at the electrode/electrolyte interface, resulting from electrostatic charge separation, is given by[8]

$$\frac{C}{A} = \frac{\varepsilon_r \varepsilon_0}{d} \quad (1)$$

where ε_0 (8.85×10^{-12} F m^{-1}) is the permittivity of the vacuum, ε_r is the relative dielectric constant of the electrolyte which is dimensionless, d (m) is the average approaching distance of ions to the electrode surface, and A (m^2) is the accessible surface area of the electrode. This capacitance is often called the electrochemical double layer capacitance, or double layer capacitance. Considering conventional values for the relative dielectric constant of the electrolyte (less than about 100) and the approaching distance d (a few 10^{-10} m), the double layer capacitance values span the range of a few tens μF cm^{-2}. Materials with a high specific surface area (m^2 g^{-1}) have then been used to increase the total electrode capacitance. Among the potential candidates, porous carbon meets all the requirements because of its large specific surface area (>1500 m^2 g^{-1} can be achieved), electrical conductivity, electrochemical stability and low cost.[9–11] Following these principles, Becker proposed the first patent using a porous carbon electrode and an aqueous electrolyte in 1957.[12] Later on, Sohio Corporation designed another apparatus also using carbon materials along with an

Pierre-Louis Taberna

Pierre-Louis Taberna received his PhD in Electrochemistry Science from Pierre et Marie Curie University (Paris, France) and he is currently CNRS research director at CIRIMAT institute, Université Paul Sabatier (Toulouse, France). His research activities have been devoted for more than twenty years to electrochemical characterization and modification of interfaces for electrochemical energy storage and conversion applications.

Patrice Simon

Patrice Simon is currently a distinguished professor of Materials Sciences at Université Paul Sabatier (Toulouse, France) and serves as Deputy director of the French network on electrochemical energy storage (RS2E). He received his PhD in 1995 from Ecole Nationale Supérieure de Chimie, Toulouse. He was appointed as Assistant Professor—Chair of Electrochemistry—at Conservatoire National des Arts et Métiers in Paris, and joint Université Paul Sabatier in 2001. His research activities are focused on the modification of material/electrolyte interfaces in electrodes for electrochemical energy storage devices, including batteries and electrochemical capacitors.

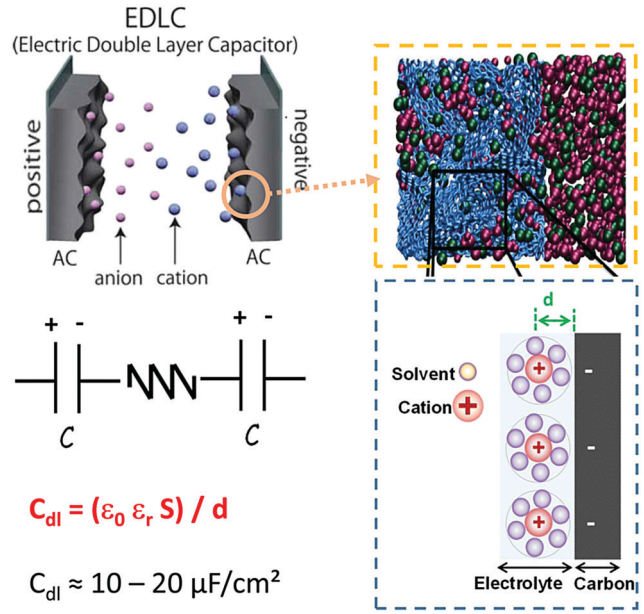

Fig. 1 The upper left panel gives the schematic representation of an electric double layer capacitor (EDLC) using porous carbon materials as electrode materials. The upper right panel shows the simulation EDL cell consisting of a porous electrode filled with an ionic liquid (blue: carbon atoms, red: cation, and green: anion). The bottom left panel gives the equivalent circuit of an EDLC and the bottom right panel gives a schematic representation of EDL formation of a negative electrode. Adapted from ref. 23 with permission from Royal Society of Chemistry (copyright 2012).

organic electrolyte, and NEC Corporation marketed the first supercapacitor devices in 1971.[13] Today, supercapacitors are everywhere, from micro-farad-sized computer electronics to thousands-farad-sized rubber-tired gantry crane.

Tremendous efforts had been focused initially on the fabrication of high SSA carbons (such as activated carbons) since eqn (1) suggested that higher SSA leads to higher specific capacitance. In 2006, several groups observed an unexpected capacitance increase by using nanoporous carbons with tunable pore structures in the subnanometer range,[14,15] revealing that not only the SSA but also the carbon pore structures, such as average pore size and pore size distribution,[16,17] have significant impacts on the carbon electrode performance. The discovery of a drastic capacitance increase when the ions were confined in sub-nanopores (<1 nm) of porous carbon materials, that is in pores less than the size of the solvated ions, has not only resulted in a two-times increase of the energy density of commercial devices but has also led to revisit the fundamental concepts of the EDL charging in confined carbon nanopores. Since then, alternative EDL theories and models have been proposed and developed to understand the charge storage mechanisms in nanoporous carbons. This has been made possible by the important development of theoretical studies as well as analytical techniques to better understand the ion environment and ion fluxes in these confined pores.

This review aims at summarizing the recent progress in the field of capacitive energy storage using nanoporous carbon materials, from the viewpoint of materials science and the characterization techniques. In particular, we will focus on the charge storage mechanisms of the nanoporous carbon-based electrode in EDLCs, from classical theories to the most recent models. Simulations and advanced *in situ* techniques have been since then extensively developed and will be reviewed in the following. Finally, perspectives will be given as a guideline for building supercapacitors with improved performance.

1.2 Key characteristics of EDLCs

As mentioned earlier, a supercapacitor cell contains two parallel electrodes, in which the positive and negative electrodes are equivalent to two capacitors assembled in series (see Fig. 1); therefore, the capacitance C_{cell} of the device is expressed as

$$C_{cell} = \frac{C_+ C_-}{C_+ + C_-} \quad (2)$$

where C_+ and C_- are the capacitances of the positive and negative electrode, respectively. Similar to batteries, the two main performance metrics used to characterize EDLC devices are the energy and power density. The energy E (W h) is given by

$$E = \frac{1}{2} C_{cell} \Delta U^2 \frac{1}{3600} \quad (3)$$

where U is the operating voltage window (V). The maximum power P_{max} (W) supply of the supercapacitors is given by

$$P_{max} = \frac{{U_{max}}^2}{4R_s} \quad (4)$$

where R_s is the series resistance (Ω). And the average power P_a (W) is associated with the energy delivered per unit time (s) and can be expressed as

$$P_a = \frac{E}{t_D} \quad (5)$$

where t_D is the discharge time.

From a practical point of view, the energy and power of EDLCs can be presented and compared on a gravimetric (per weight), volumetric (per volume), or areal (per area) basis. It is worth noting that selecting suitable performance characteristics is essential for reporting new materials and electrode architectures, and the reader can refer to several papers recently published reporting best practices for interpreting the performances of electrochemical energy storage systems.[18–21] To summarize, energy and power densities based on cell stack volume or total cell weight should be reported in Ragone plots instead of values normalized to the active material weight.[18,19] In the case of microdevices and some flexible electronics which have a negligible mass loading (tens of μg) or an extremely thin film (hundreds of nm), the volumetric or areal energy density is more appropriate than gravimetric parameters.[18,22]

The key challenge EDLCs are facing is their energy density improvement to increase their operating time beyond one minute. This results in finding strategies to improve the cell voltage and/or the capacitance, such as shown in eqn (3). Basically, the capacitance of porous carbon electrodes is controlled by the carbon/electrolyte interface, and this will

be the core of the present paper and extensively discussed in the next sections. The cell voltage of EDLCs is limited by the electrochemical stability of the electrolyte, as well as the presence of impurities (surface groups) on the carbon electrode. With the operating voltage in aqueous-based electrolytes being limited to about 1.23 V, because of water electrolysis, non-aqueous electrolytes are preferentially used since they can provide cell voltage beyond 3 V.[24,25] Advanced electrolytes which have been recently proposed for EDLC devices will be briefly described in Section 4 at the end of this paper, but the reader will find more detailed information on the electrolytes from other literature.[26–28]

To sum up, choosing the suitable electrode material and electrolyte matrix remains the core issue to enhance the performance of EDLC devices.

2. EDL capacitance at the porous carbon/electrolyte interface

2.1 EDL models based on 2D electrodes

The first EDL model proposed by Helmholtz[8] described the charge separation at the electrode/electrolyte interface considering a planar electrode surface. In this model (Fig. 2a), the charges accumulated at the electrode surface are balanced by electrostatic adsorption from the electrolyte of a counterion monolayer, resulting in two layers of opposite charges at the interface. This model is analogous to the conventional parallel-plate dielectric capacitors, and the Helmholtz layer capacitance can be therefore expressed as eqn (1).

The areal capacitance (per cm^2) of the Helmholtz layer (C_H) can be normalized by ε_r the electrolyte dielectric constant and d the thickness of the Helmholtz layer, both of them depending on the selected electrolytes. The dielectric constant value of bulk water is around 78,[29] and it falls in the range of 1 to 100 at room temperature for most of the solvents used in EDLC applications.[25,29,30] However, one should note that the dielectric constant would be arguably nonvalid at such scale (sub-nanometer) and it has been found to be smaller than that of the electrolyte bulk.[29] The Helmholtz model suggests a linear potential drop within the Helmholtz layer. However, the surface excess charges of the electrode are unlikely to be entirely counterbalanced by the Helmholtz layer, especially in the case of low concentration solutions.[25] Also, the counterion layer from the electrolyte side cannot be formed as a single static compact layer due to the ion movement from thermal fluctuation. The Gouy–Chapman model,[31,32] as presented in Fig. 2b, includes a diffuse layer between the electrode and bulk electrolyte to take into account the thermal fluctuation according to the Poisson–Boltzmann equation.[12] The ion distribution of the diffuse layer highly depends on the distance since the electrostatic attractions decrease from the electrode surface to the electrolyte bulk. The average thickness of the diffuse layer (also called Debye length, λ_D) for monovalent

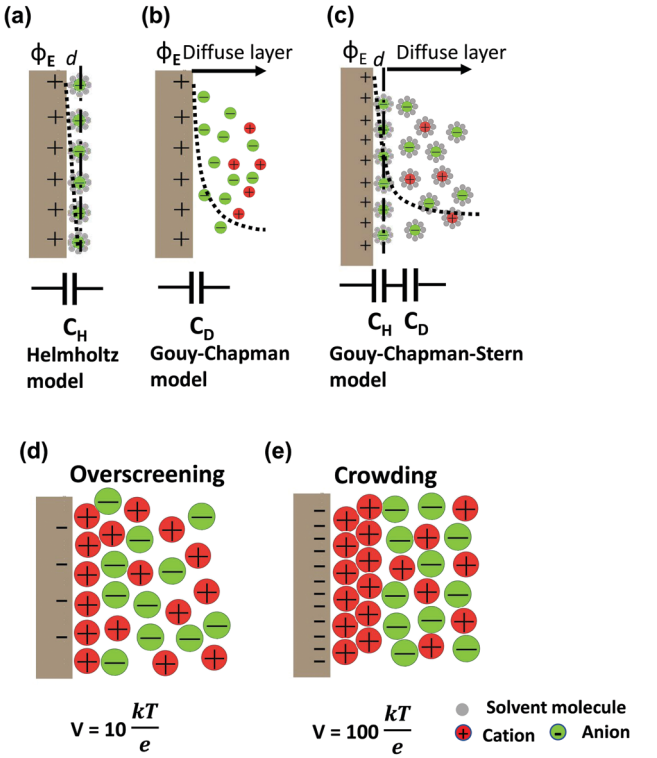

Fig. 2 Schematic diagrams of EDL models based on the positive polarized (ϕ_E) 2D electrodes in an electrolyte with solvent: (a) Helmholtz model, (b) Gouy–Chapman model, and (c) Gouy–Chapman–Stern model. The dashed lines indicate the potential drop (ϕ) in each model. The bottom insets present the simplified equivalent circuits. DEL formation of ionic liquid electrolytes by a simple phenomenological theory: (d) overscreening effect at a moderate voltage, $V = 10k_BT/e$ (0.26 V) and (e) crowding effect at a high voltage, $V = 100k_BT/e$ (2.6 V). Adopted from ref. 38 with permission from American Physical Society (copyright 2011).

electrolytes is defined as

$$\lambda_D = \sqrt{\frac{\varepsilon_r \varepsilon_0 RT}{2(zF)^2 C_0}} \quad (6)$$

where ε_0 and ε_r are respectively the vacuum dielectric constant (F m^{-1}) and the relative permittivity of the electrolyte (dimensionless), R is the ideal gas constant (J mol^{-1}), T is the absolute temperature (K), F is the Faraday constant (C mol^{-1}) and C_0 is the bulk electrolyte concentration (mol m^{-3}). Capacitance C_D of the diffuse layer can be calculated from the Poisson–Boltzmann equation, leading to

$$C_D = \frac{\varepsilon_r \varepsilon_0}{\lambda_D} \cosh\left(\frac{zF\phi}{2RT}\right) \quad (7)$$

where ϕ is the electrical potential (volts); F, the Faraday constant (C mol^{-1}); R, the ideal gas constant (J mol^{-1}); T, the temperature (K); ε_0 and ε_r, respectively the vacuum dielectric constant and the relative dielectric constant (F m^{-1}). According to (7), the differential capacitance C_D (F cm^{-2}) of the Gouy–Chapman model is then no longer constant. Instead, the model predicts a kind of "U" shape of the differential capacitance with the electrode potential, which is in accordance with the

experimental results observed using NaF solutions in contact with Hg in low concentration solutions.[33] Also, the capacitances experimentally measured (a few tens of μF cm^{-2} in aqueous electrolytes for instance) were far below those predicted from the model (a few hundreds of μF cm^{-2}).[34] Indeed, one major flaw of the Gouy–Chapman model is to consider point charges which can virtually approach the surface at zero distance leading to an infinite capacitance. To address these issues, Stern modified the Gouy–Chapman model by considering an actual size for ions which led to an additional compact layer (Stern layer) in series with the diffuse layer (Fig. 2c);[35] the compact layer is identical with the Helmholtz layer from the physics point of view, whose thickness is x_H (m). The EDL capacitance of this Gouy–Chapman–Stern model is given by

$$\frac{1}{C_{DL}} = \frac{1}{C_H} + \frac{1}{C_D} = \frac{x_H}{\varepsilon_0 \varepsilon_r} + \frac{\lambda_D}{\varepsilon_0 \varepsilon_r \cosh\left(\frac{zF\phi}{2RT}\right)} \quad (8)$$

where C_H and C_D are the capacitances of the Stern (Helmholtz) layer and the diffuse layer, respectively (both in F m^{-2}). The total EDL capacitance is governed by the smallest capacitance between C_H and C_D. In highly concentrated electrolytes, the diffuse layer thickness (λ_D) drops to zero so that the Helmholtz capacitance (C_H) is the only one to be considered. The Gouy–Chapman–Stern model was indeed a milestone that depicted a more realistic gross feature of the EDL, which is close to some experimental observations. However, this model still suffers from some limitations. For instance, it does not take into account the effects of ion–ion correlation, which are important, especially in solvent-free ionic liquid systems.[25,36] Besides, some chemical interactions between the electrode surface and species from the electrolyte, also known as specific adsorption, may also impact the EDL formation.[34] Moreover, previous literature suggested that considering a linear potential drop within the compact layer was inappropriate in the case of high electrode polarization in high concentration electrolytes.[25,37] However, the Gouy–Chapman–Stern model provided a constructive and predictive interpretation of the EDL that had led to the development of the EDLC field over the past few decades.

The EDL formation at planar electrodes in solvent-free ionic liquid electrolytes deviates from predictions of classical models based on dilute-solution approximation.[36] Unlike solvent-containing electrolytes, the absence of solvent molecules for screening the charge between cations and anions in ionic liquids results in strong ion–ion correlations. The orientations and rearrangements of non-spherical shaped ion chains triggered by the polarization and complex force fields make it even more difficult to depict the electrode/ionic liquid interface structure.[25] Kornyshev's group predicted the existence of a differential capacitance–potential curve with bell-like and camel-like shapes based on mean-field theory,[36] which was further confirmed by experimental and simulation studies.[39–43] For potential below the potential of zero charge (PZC) range, an over-screening effect is proposed due to the ion–ion correlations (see Fig. 2d), leading to the formation of a first counterion layer with an excess charge compared to the electrode. For even larger polarization below PZC, a crowding effect is predicted at higher voltage (*vs.* PZC), when the increased polarization suppresses the over-screening and leads to the formation of counterions approaching the inner layer (Fig. 2e).[36,38] On a flat electrode, the global view is now that the EDL is formed by a stacking of multilayers of ions, as evidenced from both experimental and modeling observations.[41,43–47] Monolayered interfacial structures[48,49] and a controversial dilute electrolyte-like picture[50] have also been proposed. Using molecular dynamics simulation based on coarse grained models, Kirchner *et al.* suggested a structural transition from multiple alternating layers of counter- and co-ions to a surface-frozen monolayer of counterions at certain charge densities.[51]

2.2 High surface area carbons for EDLC electrodes

According to IUPAC,[52] pores can be classified into three categories, namely micropores (0.2 to 2 nm), mesopores (2 to 50 nm), and macropores (>50 nm). The smallest pores – micropores – can be sub-divided into super- (>0.7 nm) and ultra-micropores (<0.7 nm). Micropores are then nanosized. For the sake of clarity, in the next sections, we will refer to nanopores as pore size of nanoporous and sub-nanoporous dimensions.

As mentioned above, nanoporous carbons have been widely used as EDLC electrode materials. First, an extremely high specific surface area (beyond 2000 m^2 g^{-1}) as well as tunable average pore size and pore size distribution can be achieved using various processes, including activation, carbonization, *etc.*[5] Carbon materials also have excellent electrochemical stability in both aqueous and non-aqueous systems. The operating voltage windows of carbon-based EDLCs were usually limited by the decomposition potential of electrolytes instead of the carbon electrodes. Their electrical conductivity allows for a limited ohmic drop during electrochemical polarization. Finally, they can be prepared from low cost, abundant bio-sourced precursors using cheap processes.[11]

Fig. 3 shows that various kinds of carbon materials with several dimensionalities can be used for EDLC applications, from 0-dimensional (0D) non-porous carbon onions, to 1D (carbon nanotubes and carbon fibers), 2D (graphene), and 3D porous carbons (activated carbons, templated carbons, carbide-derived carbons). A few examples of various carbons used in EDLCs are summarized in Table 1.

Activated carbons (ACs) are amorphous porous carbons containing mainly sp^2 carbon atoms. They are prepared from physical (thermal) and/or chemical activation of various types of natural or synthetic organic precursors.[11] In general, pre-carbonization is required before the activation process when natural precursors are used as carbon precursors. Physical activation takes place in the high temperature range of 600–1200 °C under oxidizing atmospheres (such as steam and CO_2), while chemical activation requires a lower temperature range of 300–600 °C using chemical reagents (such as KOH, $ZnCl_2$, *etc.*). ACs are highly porous with a broad range of pore sizes from a few tens of nanometers to a few nanometers, resulting in high SSA, mainly ranging from 1000 to 2000 m^2 g^{-1}. The SSA and pore size distribution are predominantly determined

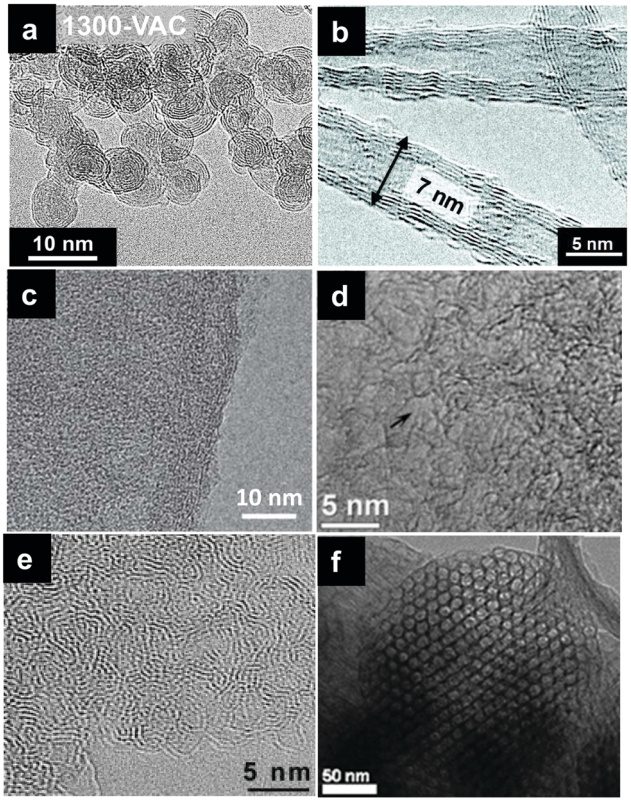

Fig. 3 Transmission electron micrographs (TEM) of various carbons with several dimensionalities for EDLCs: (a) OLCs,[94] (b) CNTs,[76] (c) graphene,[92] (d) ACs,[95] (e) CDCs,[65] and (f) TCs,[96] with permission from Elsevier (copyright 2015), 2011 American Chemical Society, Springer Nature (copyright 2014), Elsevier (copyright 2019), Elsevier (copyright 2006), and Royal Society of Chemistry (copyright 2009), respectively.

by carbon precursors and the activation process. Owing to their relatively good electrical properties and high SSA, and especially the low cost compared to other carbon materials, ACs have been widely used as supercapacitor electrode materials. AC based supercapacitors show a long cycle life span ($>10^6$ cycles), making ACs the best option as supercapacitor electrodes in commercial devices. The electrochemical performances of AC based electrodes have been significantly improved during the past few years, exceeding 200 F g^{-1} in nonaqueous based electrolytes.[16,53–55] This has been mainly achieved by tuning the mean pore size and pore size distribution in the micropore range, below 1.5 nm (see below). In aqueous electrolytes, AC electrodes enable the delivery of capacitance ranging from 100 to 300 F g^{-1} depending on pore size distribution and surface chemistry, but the penalty is the low energy density associated with the limited voltage window.[56,57]

Carbide-derived carbons (CDCs) are produced by selective etching of metals from various metal carbides, with TiC being the most used.[58] CDCs offer the key advantage of fine-tuning their pore size (below 2 nm) and pore size distribution by adjusting the synthesis parameters such as temperature and time; the carbon structures and particle size are defined by the carbide precursors.[59] Generally, CDCs exhibit high BET SSA ranging from 1000 to 2000 m^2 g^{-1} and a narrow pore size distribution in the nanometer and sub-nanometer range. Taking TiC-CDCs as an example, their average pore sizes vary from 0.68 to 1.1 nm which can be tunable with 0.05 nm accuracy by changing the chlorination temperature in the range of 500 to 1000 °C.[14] Owing to their controlled, narrow pore size distribution in the micropore range, CDCs have been extensively used as model materials to understand the fundamental of EDL formation in porous materials[14,60] and have helped in identifying the capacitance increase in nanopores (see later). TiC-CDCs showing a specific capacitance value of 160 F g^{-1} were reported in an ionic liquid, which showed a high volumetric capacitance of 85 F cm^{-3}, higher than standard ACs at that time.[60] Later on, several approaches have been proposed to design CDCs with high EDL capacitance and high-rate performance, including reducing the CDC particle size[61] and adding mesopores.[62–64] Interestingly, CDCs have moved into real products since they are now used in commercial EDLCs.[65]

Templated carbons (TCs) are obtained by template-assisted carbonization of carbon precursors and subsequent removal of the templates. This approach leads to carbon materials with precise control of the pore size in the mesopore range, which is of great significance for electrode materials of supercapacitors.[66] The pore structures of TCs can be controlled by using two kinds of templates, namely hard template (such as zeolites, mesoporous silicas, and metal oxides) and soft template (such as metal–organic frameworks and block copolymer surfactants).[10] Numerous publications based on TCs have been published during the last decade; here we provide a few examples. Zeolite templated carbons (ZTC) produced by acetylene CVD can achieve a high capacitance of 140 to 190 F g^{-1} (70 to 85 F cm^{-3}) in organic-based electrolytes.[67,68] Such materials are interesting for conducting basic studies of ion transfer and adsorption in nanopores. However, the commercial development is limited by the cost of production.

Carbon onions, also called onion-like carbons (OLCs), are spherical or polyhedral carbon nanoparticles, consisting of concentric defective sp^2-hybridized carbon multiple shells, with a small size around a few tens of nanometers. Among a number of synthetic routes for preparing OLCs, thermal treatment of detonation nanodiamond powders is the most practical method.[69–71] Since OLC particles are non-porous, they exhibit a limited external SSA of 300–600 m^2 g^{-1}, together with a high interparticle pore volume around 1 cm^3 g^{-1}.[72] The pore structure of OLC electrodes consists predominantly of micro and mesopores existing between the OLC particles. However, due to the non-porous particles, the whole surface is highly accessible to electrolyte ions. As a result, OLC-based electrodes can achieve a limited capacitance of 50 F g^{-1},[73,74] with an excellent power ability due to the highly accessible external surface area. In summary, OLCs are not good candidates to increase the capacitance of EDLC electrodes but can deliver high power.[75,76] Besides, OLCs with a particle size around 10 nm are also employed as conductive additives for EDLCs.[77,78]

Carbon nanotubes (CNTs) are large cylindrical carbon materials consisting of a hexagonal arrangement of sp^2 hybridized

Table 1 Examples of carbon materials for EDLCs

Carbon	Electrode materials	SSA[a] (m^2 g^{-1})	Electrolyte (mol l^{-1})	C_g[b] (F g^{-1}) C_v (F cm^{-3})	Voltage (V)	Test conditions	High-rate test c_g[b] (F g^{-1}), c_v (F cm^{-3})	Ref.
ACs	PICACTIF SC	2315 (B)	TEAMS (1.7)	125 (g)	2	10 mA cm^{-2} (2el)	—	53
	Ppy-AC	3432 (B) 2244 (D)	$EMIBF_4$	256 (g)	2.3	1 mV s^{-1} (2el)	150 (g) 100 mV s^{-1}	55
	AC-W800	3967 (B) 2387 (D)	$TEABF_4$ (1)	236 (g) 100 (v)	2.3	1 mV s^{-1} (2el)	173 (g) 100 mV s^{-1}	54
	B-AC	2841 (B)	KOH (2)	330 (g)	1	1 A g^{-1} (3el)	238 (g) 10 A g^{-1}	57
CDCs	TiC-CDC	1270 (B)	$TEABF_4$ (1.5)	145 (g) 80 (v)	2.3	5 mA cm^{-2} (2el)	128 (g) 100 mA cm^{-2}	14
	TiC-CDC	1270 (B)	EMITFSI	160 (g) 85 (v)	3	5 mA cm^{-2} (2el)	—	60
	OM-CDC	2364 (B)	H_2SO_4 (1)	188 (g)	0.6	0.1 A g^{-1} (2el)	140 (g) 20 A g^{-1}	64
	Mesoporous-CDC	2250 (B)	TEA BF_4 (1)	170 (g)	2	0.1 A g^{-1} (2el)	150 (g) 17 A g^{-1}	62
TCs	ZTC	2940 (B)	TEA BF_4 (1)	168 (g)	2	0.05 A g^{-1} (3el)	153 (g) 2 A g^{-1}	67
	ZTC-L	2910 (B)	$TEABF_4$ (1)	75 (v)	2	1 A g^{-1} (3el)	60 (v) 20 A g^{-1}	68
	MCNAs	1266 (B)	$TEABF_4$ (1)	152 (g)	2.5	5 mV s^{-1} (2el)	—	97
	Z-900	1075 (B)	H_2SO_4 (0.5)	214 (g)	1.2	5 mV s^{-1} (3el)	115 (g) 100 mV s^{-1}	98
OCLs	ND-1200	500 (B)	$TEABF_4$ (1.5)	38 (g)	2.3	5 mA cm^{-2} (2el)	30 (g) 200 mA cm^{-2}	73
	1700-VAC	364 (B) 340 (D)	$TEABF_4$ (1)	20 (g)	2.7	1 mV s^{-1} (2el)	18 (g) 1 V s^{-1}	94
CNTs	MWCNT	200 (B)	$TEABF_4$ (1.5)	18 (g)	2.3	5 mA cm^{-2} (2el)	16 (g) 200 mA cm^{-2}	73
Graphene	a-MEGO	2400 (B)	$BMIMBF_4$ (1)	165 (g) 60 (v)	3.5	1.4 A g^{-1} (2el)	164 (g) 5.7 A g^{-1}	90
	HGF	830 (B)	$EMIBF_4$ (1)	262 (g) 186 (v)	3.5	1 A g^{-1} (2el)	190 (g) 20 A g^{-1}	92
	EM-CCG	167 (B)	$EMIBF_4$ (1)	167 (g)	3.5	1 A g^{-1} (2el)	135 (g) 10 A g^{-1}	89

[a] B and D represent SSA obtained from the BET and DFT method, respectively. [b] g and v give the specific gravimetric and volumetric capacitance, respectively.

carbon atoms, which are formed by rolling up a single sheet of graphene (single-walled carbon nanotubes, SWCNTs) or by rolling up multiple sheets of graphene (multiwalled carbon nanotubes, MWCNTs).[79] To date, the commonly used synthesis techniques for CNTs are arc discharge, laser ablation, and chemical vapor deposition (CVD).[80] The SSA of CNTs ranges from 100 to 1000 m^2 g^{-1}.[81] CNTs can exhibit narrow pore size distribution, but the internal pores are unlikely to contribute to EDL capacitance due to the ion diffusion limitation inside the carbon walls and because of the absence of the inner electric field in regular operating conditions. Instead, similar to OLCs, the external surface of CNTs can be used to form exohedral capacitors, leading to a moderate capacitance below 100 F g^{-1}.[59] However, the highly accessible external surface and excellent electric conductivity make CNTs suitable candidates for high power devices,[59] even under extreme climatic conditions.[76] In addition, CNTs have been used as model materials in simulation experiments to study the double layer formation inside or outside the tube.[82–84]

Graphene, one of the most studied two-dimensional materials, can be synthesized by (1) "bottom-up" approaches, such as CVD, epitaxial growth and chemical synthesis, and (2) "top-down" methods, including the micromechanical and liquid-phase exfoliation of graphite and the reduction of graphene oxide (rGO).[85] A single graphene sheet has a high theoretical SSA of 2630 m^2 g^{-1} and a high intrinsic capacitance of about 21 μF cm^{-2}.[86,87] However, these excellent properties at the single layer graphene scale do not translate at large macroscopic scale due to the restacking issue.[85] In order to enhance the performance of graphene-based EDLCs, extensive efforts have been made to address such a restacking issue. One promising approach is to pre-insert molecules between the graphene layers or build 3D structures based on 2D rGO.[88–91] For example, porous holey graphene (HGF) material showed an impressive capacitance beyond 200 F g^{-1} and high gravimetric and volumetric stack energy densities[92] owing to the creation of 3D ionic pathways, but the synthesis process has to be carefully controlled to prepare porous graphene with suitable structure

and surface composition. In summary, graphene and graphene-based materials show some interesting performance at the lab level, but the cost issue and the lack of techniques for industrial-scale high-quality graphene electrode production still hamper their commercial development. However, as an ideal 2D carbon surface, graphene offers great opportunities as a model surface material to develop some fundamental studies on the understanding of EDL formation in real and simulation experiments.[93]

2.3 Capacitance in nanoporous carbon-based electrodes

There are numerous parameters that affect the electrochemical performance of nanoporous carbon material-based EDLC electrodes, such as conductivity, the presence of surface groups, and most importantly, SSA, pore size, and PSD. Although most of the carbons can achieve high conductivity owing to their high density of electronic states at the Fermi level, still a few carbons exhibit semiconducting properties, such as SWCNTs with certain diameter and helicity[99] or bilayer graphene.[100] This semiconducting character was suggested to account for the observed current drop near the potential of zero charge (PZC) in a cyclic voltammogram (CV), resulting in a butterfly-shaped CV in a three electrode system and a trapezoid-shaped CV in a two electrode device, indicating that EDL capacitance in some carbon-based electrodes was not independent of the charging state.[29] In addition, Xie *et al.* identified that the quantum capacitance *versus* gate potential has a symmetric V-shape with a minimum at the Dirac point in single- and bilayer graphene.[87] Efforts have been made to modify the quantum capacitance of graphene by increasing its charge carrier density *via* N-doping approach, leading to an enhanced interfacial capacitance.[101] However, more evidence on how the quantum capacitance quantitatively affects the electrode capacitance is needed. Besides, the presence of surface groups has strong impacts on the electrochemical performance of carbon-based electrodes, especially in aqueous systems. The surface groups such as –O and –OH are frequently present as impurities in activated carbons or rGO materials, coming from the synthesis and/or activated process. In addition, –N groups are used as the dopant to improve the electrochemical performance of carbons. These surface groups contribute to the capacitance in aqueous electrolytes by adding a pseudocapacitive contribution, which is beyond the scope of this review. Most importantly, the capacitance of carbon-based electrodes in the EDLC system is strongly correlated to the SSA and pore structures.

A comprehensive characterization of the surface and textural properties is crucial to understand how the SSA and pore structures affect the electrochemical performance of porous carbon-based EDLCs since SSA is strongly connected to the pore structures. However, porous carbons are complex materials with various structures, including local graphitized and/or disorder carbon arrangements, that it is unrealistic to completely depict their real local- and long-range structures.[102,103] Nevertheless, many experimental techniques, including gas sorption, electron microscopy, Raman spectroscopy, nuclear magnetic resonance spectroscopy, X-ray scattering, neutron scattering, and recently developed *in situ* techniques, have made sound progress in this way.[104] In addition, complementary simulation techniques (such as the Monte Carlo method and density functional theory) and analysis models (pair distribution function) were also proposed to unravel the pore structures of porous carbons.[104] Among these techniques, the gas sorption technique is the most commonly used one owing to its non-destructive nature and relatively low cost. Importantly, it can be used to characterize the textural properties of porous materials with a wide range of SSA and pore size distributions.[105] The next section will focus on the surface area and pore structure characterization based on the gas sorption technique; other advanced techniques mentioned above will be presented in Section 3.

Gas sorption technique. From the general point of view, the characteristics of porous carbons, including SSA, average pore size, pore size distribution, and porous volume, can be estimated from experimental gas sorption isotherms by using various theoretical models.[106] The probe gas and the appropriate model should be carefully selected to evaluate the SSA and pore textures of porous carbons, especially when micropores (<2 nm) are involved. N_2 gas sorption (cross-sectional area of 0.162 nm^2) at its boiling temperature (77 K) has been used for a while as a standard gas probe for porous carbons to collect the adsorption isotherm. However, since in pores smaller than 2 nm the interaction of the surface is increasing, it has been pointed out that the nitrogen quadrupole moment brings out some discrepancies because of the orientation of the adsorbed nitrogen molecules on the porous carbon surface[107] which in turn also affects the micropore filling pressure, limiting the accessibility of probe nitrogen to be adsorbed in micropores. Consequently, the nitrogen adsorption isotherm might not be reliable to construe the accurate information of SSA and pore size distribution of micropore sized carbon.[107] As an alternative, Ar (cross-sectional area of 0.166 nm^2) gas sorption at its liquid temperature of 87 K was used to measure the SSA and PSD of porous carbons. The slightly higher measurement temperature with Ar, compared to that with nitrogen at 77 K, together with a relatively high micropore filling pressure (10^{-5} to 10^{-3} *vs.* 10^{-7} to 10^{-5} with N_2) results in high gas molecule diffusion, improving the resolution of gas adsorption isotherms in the micropore range. These advantages make Ar a more interesting gas probe to characterize nanoporous carbons. However, for ultra-micropores, the low operating temperature for nitrogen and argon gas limits the kinetics of the gas adsorption process. Carbon dioxide (diameter of 0.33 nm) adsorption at 273 K can serve as a suitable probe to assess the ultra-micropores, taking advantage of the high operating temperature (room temperature) which allows the probe molecule to characterize micropores as small as 0.4 nm, owing to the fast diffusion of gas molecules.[108] It is worth noting that CO_2 is not suitable for porous carbons containing a large amount of surface groups because the quadrupole moment of CO_2 is even higher than that of N_2.[105]

Once the adsorption isotherm has been made, one should select the appropriate model to fit the isotherm to get the SSA, pore volume and PSD. The Brunauer–Emmett–Teller (BET) equation was considered as the standard model to evaluate

the surface area, denoted as S_{BET}, for decades.[109] However, now it is well known that this simplified model cannot clearly distinguish between monolayer–multilayer adsorption and micropore filling in microporous materials, leading to significant inaccuracies in the SSA and pore size distributions.[110] Various classical macroscopic methods including models based on the Kelvin equation and Dubinin–Radushkevitch related approaches were also applied to interpret the gas isotherm, but the lack of description of molecular packing at the local level limits their applicability. DFT-based models and simulation from the microscopic level are now considered as more effective methods to analyze the data of gas sorption experiments.[111] Non-local density functional theory (NLDFT)-based models firstly proposed by Lastoskie *et al.* to characterize nanoporous carbons have led to significantly improved accuracies.[102,112,113] Thommes *et al.* proposed the quenched solid density functional theory (QSDFT) that takes into account the effects of surface heterogeneity, leading to a more reliable evaluation of porosity in nanoporous carbons.[105,110,114]

Although the description of the "real" surface of nanoporous carbon still remains challenging as outlined above, reliable porous carbon characteristics such as SSA, pore volume and PSD can be assessed by gas adsorption with a carefully selected gas probe and analysis model. Also, porosity obtained from other techniques (such as scattering methods) showed a good agreement with gas adsorption.[115,116] This makes reasonable the comparison of the textural parameters of different porous carbons obtained from gas adsorption measurements, to further understand the correlation between electrochemical performance and porosity.

Capacitance *vs.* SSA. According to the Gouy–Chapman–Stern model, the double layer capacitance (C_{DL}) is proportional to the EDL surface area, which has been triggering tremendous efforts to increase the EDLC performance by increasing the SSA of carbon materials. Initial research on activated carbon was then directed towards increasing the pore volume by developing high SSA and refining the activation process. However, it was quickly established that the gravimetric capacitance of activated carbons was limited even for the most porous samples exhibiting a very high SSA.[16,53,117,118] As pointed out by Ruoff *et al.*, the area-normalized capacitance of various porous carbon-based electrodes decreased to 4–5 μF cm^{-2} when the SSA was larger than 1500 m^2 g^{-1}.[119] Barbieri *et al.* have attributed this capacitance saturation at ultrahigh SSA to a space charge capacitance, which originates from a space charge gradient layer on the electrode side.[118] Additionally, the presence of micropores was considered to be mainly at the origin of the capacitance limitation. Specifically, the narrow sub-nanometer size micropores in porous carbons were believed to be too small in size to accommodate the electrolyte ions, which excluded any EDL contribution from these non-accessible pores; such an ion sieving effect was previously suggested as another explanation.[17,120,121]

As a result, no direct clear trend could be established between SSA and capacitance.

Capacitance *vs.* pore size. There was a long-held axiom stating that carbon pore size larger than the solvated ion size was needed so that pores could be accessible to the electrolyte ions.[117] In other words, porous carbon with a pore size smaller than the solvated electrolyte ions does not contribute to EDL capacitance and thus was considered useless. Taking into account the commonly used electrolytes, the sizes of bare ions and ions with solvation shells vary from a few to tens of Å. For instance, the size of the bare tetraethylammonium cation is around 0.68 nm, and its solvation shell in acetonitrile (ACN) increases the size of the solvated ion to 1.3 nm. Under this circumstance, large micropore and mesopore carbons seem to be the most suitable candidates for allowing a high capacitance.

However, several groups reported high capacitance by using microporous carbons with sub-nanometer pores in various electrolyte systems.[14,15,122,123] Taking advantage of the tunable pore structure of CDCs, Chmiola *et al.* reported in 2006 high gravimetric and volumetric capacitance for CDC pore size below 1 nm.[14] The specific gravimetric capacitance normalized by BET SSA (C/S_{BET}) obtained from Ar gas sorption (see Fig. 4a) revealed a capacitance increase for carbon pore size smaller than 1 nm. In addition, DFT SSA-normalized capacitance was also calculated at that time and the same capacitance increase was obtained, which indicated that the underestimation of SSA of microporous carbons by the BET model was not the cause of the increasing trend of C/S_{BET}.[14] Raymundo-Pinero *et al.* reported a similar increasing trend of capacitance using microporous ACs in both aqueous and non-aqueous electrolytes. They suggested that pore filling was more efficient for EDL formation when the pore size is around 0.7 nm in aqueous and 0.8 nm in organic electrolytes, respectively.[15] The EDL capacitance increase in sub-nanometer pores was defying the traditional views of ion adsorption and EDL formation in carbon electrodes.[5] Partial ion desolvation was proposed to explain the enhanced capacitance in sub-nanometer pores: owing to the distortion of the solvation when entering nanosized pores, the ion could get closer to the carbon wall so that the d in eqn (1) is decreased (Fig. 4c), confirming previous experimental observations made on nanoporous carbons under polarization.[17,124–126] Later on, by monitoring the potential change of each electrode of a symmetric system using a silver quasi-reference electrode, a different EDL capacitance behavior at negative and positive electrodes was reported by Chmiola *et al.*,[127] which confirmed partial desolvation during the charge/discharge process.

The desolvation effect was further studied by using advanced *in situ* techniques and simulation approaches, and this is the focus of Section 3. All the sets of results make this ion desolvation a universal phenomenon for virtually all nanoporous carbons because of the pore size dispersion and presence of ultranarrow (sub-nanometer) pores.[128]

However, because of the presence of the solvation shell that affects the effective ion size, it was not clear whether an optimum pore size could be achieved to maximize the capacitance. To this end, CDCs with various controlled pore sizes and PSD were characterized in a solvent-free electrolyte, ethyl-methylimidazolium-bis(trifluoromethane-sulfonyl)imide (EMITFSI).[60] Solvent-free electrolytes rule out the solvation effect, and EMI^+ and $TFSI^-$ have similar ion sizes (0.79 and 0.76 nm in the longest

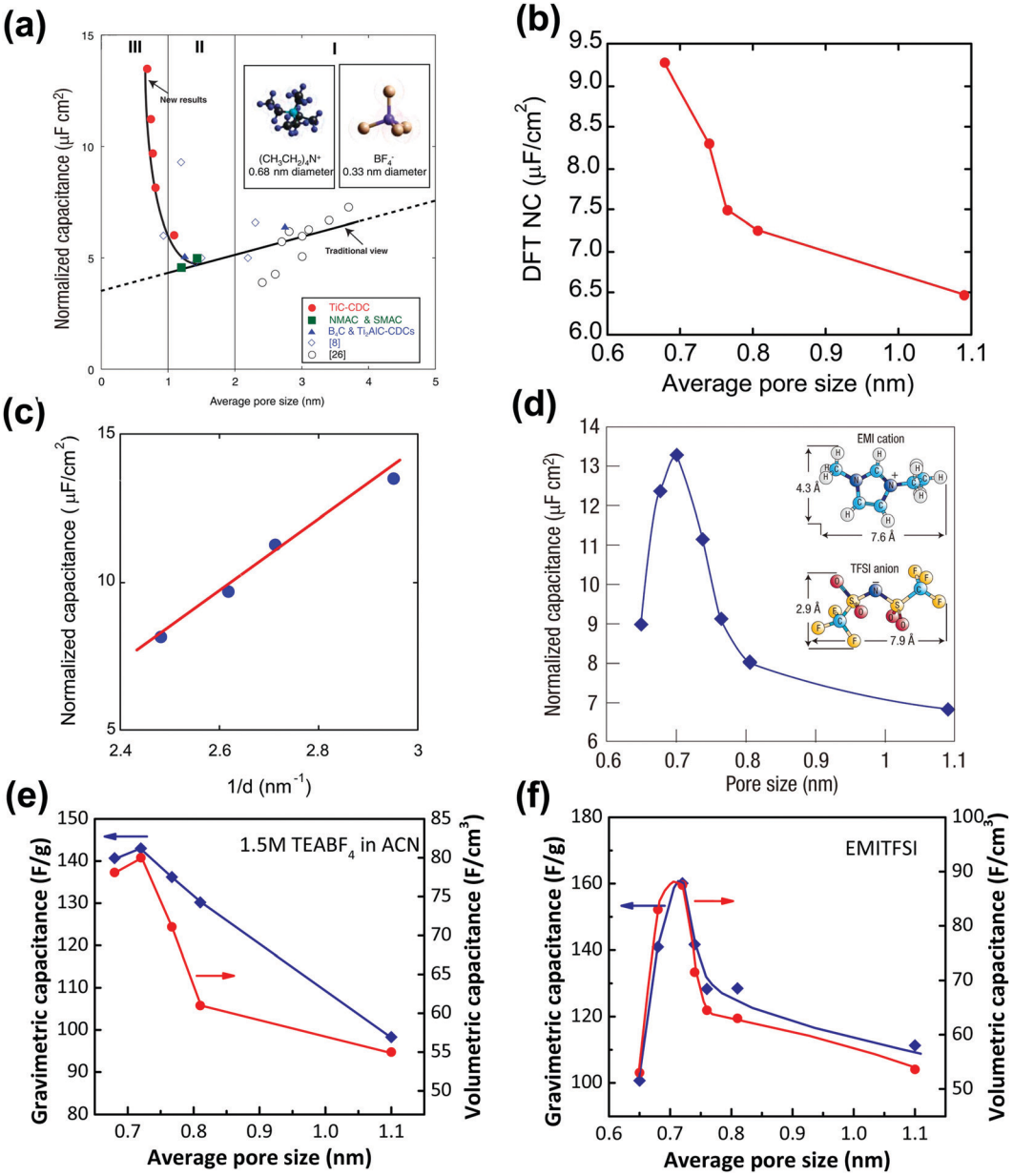

Fig. 4 Plots of specific capacitance normalized by SSA *vs.* average pore size obtained for various CDC electrodes in 1.5 M $TEABF_4$ in ACN (a) and (b), and in neat EMITFSI ionic liquid (d). Please note: SSA was obtained from the BET method for (a) and (d), and from the DFT method for (b). (c) Plots of normalized capacitance *vs.* the average distance from the charge ion center to the pore wall of various CDCs. Plots of specific gravimetric and volumetric capacitance *vs.* pore size of CDC electrodes in 1.5 M $TEABF_4$ in ACN (e) and in neat EMITFSI ionic liquid (f). Panels (a, b, c, and e) are reproduced from ref. 14 with permission from American Association for the Advancement of Science (copyright 2006), panel (d) is reproduced from ref. 5 with permission from Springer Nature (copyright 2008), and panel (f) is reproduced from ref. 60 with permission from American Chemical Society (copyright 2008).

dimension for TFSI and EMI ions, respectively).[60,127] Fig. 4d shows the change of the normalized capacitance of various CDC electrodes *vs.* pore size in the EMITFSI electrolyte. The same trend was also reported for the change of the specific gravimetric and volumetric capacitance *vs.* the carbon pore size. The capacitance reaches a maximum when the ion size is close to the carbon mean pore size. This result was a major finding since (i) it shows that high capacitance could be achieved when the ion was confined in pores of the same dimension, and (ii) it evidences that the conventional way to describe the EDL formation using the Gouy–Chapman model in these confined nanopores was not valid anymore. This has led to an important work from both experimental and modelling point of view to explain this behavior, which will be discussed in Section 3.

Although numerous experimental and modeling studies confirmed the capacitance increase in nanopores, Centeno *et al.* reported a "regular pattern", depicting a constant specific capacitance contribution of all micro- and mesopores in porous carbon-based EDLCs.[129,130] The constant capacitance claimed

by Centeno *et al.* was the capacitance normalized by surface area (S), where S was determined by using different probe molecules.[129,130] In ref. 129, Centeno *et al.* attributed the increase of surface-related capacitance (C/S) reported by Chmiola *et al.*[14] to the shortcoming of the BET method for SSA determination, despite the fact that similar capacitance increase in the sub-nanometer range pores was also observed by using NLDFT SSA.[14]

Nevertheless, this controversy raised a very important discussion about the trend of C/S *vs.* pore size, and it is important to define the limitations of the approach. To begin with, the commonly used pore size in the literature is average pore size, since porous carbon with ideal monodisperse pore size distribution does not yet exist. The mean pore size is generally defined as the pore size where the value of 50% of cumulative porous volume is reached.[131] Moreover, most of the porous carbons exhibit a dispersed, broad PSD, which makes the use of average pore size to describe the porosity inaccurate unless these carbons have unimodal pore size distribution.[132] Therefore, porous carbons with a narrow unimodal pore size distribution such as CDCs are preferred to be used for the experimental verification of C/S *vs.* pore size. Then, unlike SSA which can only be obtained based on the use of a gas probe with finite dimension and modeling, the specific gravimetric or volumetric capacitance C can be accurately measured by electrochemical experiments by measuring the capacitance, the weight, and the volume of carbon films. As shown in Fig. 4e and f, there is a similar correlation between the specific gravimetric capacitance and pore size, as well as specific volumetric capacitance.[14,60] Also, some works specifically designed to address this question confirmed the increasing trend of capacitance in micropores (see also Section 3). For instance, Galhena *et al.* confirmed the correlation between capacitance and pore size by *in situ* tuning the interlayer constrictions (measured by XRD) of a graphene oxide paper in an organic electrolyte, eliminating any potential interference factors that may originate from the complex porosity evaluations.[133] A similar increasing trend of capacitance in the sub-nanometer pore size (referred to as interlayer spacing in this case) range was reported by the same group and the maximum capacitance was obtained when the pore size matched the desolvated ion size.[133]

Although gravimetric and volumetric capacitances are better to be used since they are based on reliable experimental measurements, the use of SSA-normalized capacitance is interesting for fundamental studies of the EDL formation at porous carbon electrodes. As mentioned above, the porosity is determined by the size of the molecular probe used, and there is no doubt that this affects the SSA value used to normalize the capacitance. In ref. 130, Centeno *et al.* investigated three microporous carbon monoliths – average pore size in the micropore range – in 1 M solution of $TEABF_4$ in ACN. They selected a cut-off at $S_{>0.63}$ (that is the surface of pores above 0.63 nm, around 75% of the S_{total}) to determine the SSA-normalized capacitance, which subsequently leads to the absence of capacitance change with the average carbon pore size.[130] Note that, the computed neat ion size of TEA cation and BF_4 anion is around 0.68 and 0.44 nm, respectively,[134] and the specific value of 0.63 nm is the size of carbon tetrachloride used as a molecular probe in the porosity evaluation. $S_{>0.63}$ was then interpreted as the accessible surface area of the carbon monoliths for both TEA^+ cation and BF_4^- anion. However, this might be misleading since experimental evidence suggested that cations could be distorted when entering small pores under electric polarization.[135] For instance, Ania *et al.* studied a microporous carbon with an average pore size centered at 0.58 nm with about 60% of pores smaller than the neat TEA cation in the same electrolyte as ref. 130; still, a high capacitance of 92 F g^{-1} was obtained.[135] As illustrated in Fig. 5a, pores with a size of about 0.6 nm could allow distorted desolvated TEA^+ to be squeezed inside, which at least indicated that pores smaller than 0.63 nm could be accessible for TEA^+ to contribute to EDL capacitance. This is even more true when using BF_4^-, since its computed size is around 0.44 nm and it is assumed that such ions can access pores less than 0.63 nm, which makes

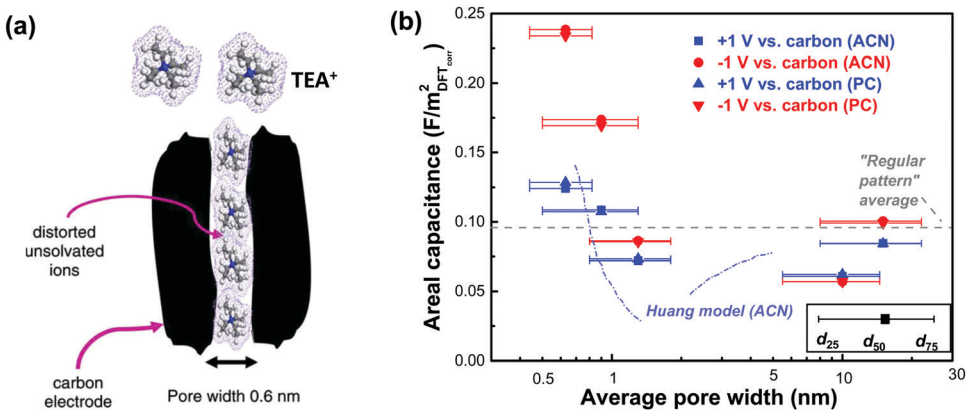

Fig. 5 (a) Illustration of the polarization-induced distortion of TEA^+ ions in pores with a size of 0.6 nm. Reprinted from ref. 135, with permission from Elsevier (copyright 2009). (b) Plot of differential specific surface-normalized capacitance *vs.* pore size of various carbons in organic electrolytes of 1 M $TEABF_4$ in ACN and PC. The plot is reproduced from ref. 137 with permission from 2016 American Chemical Society; the grey dashed line representing the regular pattern is from ref. 129, and the blue dashed line representing the Huang model is from ref. 134.

the absence of any capacitance dependence on the pore size highly questionable.[129,130,136] Instead, Jackel *et al.* proposed another model to investigate the capacitance of microporous carbons in organic electrolyte systems.[137] DFT kernels were used to extract the porosity of several porous carbons from N_2 and CO_2 adsorption isotherms. Instead of collecting the total capacitance of the cell, the differential capacitances at both positive and negative electrodes during polarization, which reflect the contribution to EDL capacitance from the anions and cations, were used to understand the correlation between *C*/*S* and pore size. Importantly, the surface area accessible to anions and cations was also defined differently, with the cutoff pore size of 0.4 ($S_{>0.4}$) and 0.6 ($S_{>0.6}$) nm being selected for BF_4^- and TEA^+, respectively, to take into account the difference in ion size. The pore sizes of d_{25} and d_{75} (representing the pore width at 25 and 75% of the total pore volume, respectively) were also added in complement to d_{50} (the pore width at 50% of the total pore volume) to capture a more reliable picture of the porosity than the mean diameter.[137] Fig. 5b shows the differential specific capacitance of porous carbons normalized by the accessible DFT SSA *vs.* pore size in both ACN and PC based electrolytes: a similar increasing trend of surface-normalized capacitance in the sub-nanometer range pores was observed.[137]

Finally, the capacitance increase in the sub-nanometer pore range was also studied from a theoretical point of view using DFT and molecular dynamics simulations, with various carbon structures and electrolyte combinations, and the details are presented in Section 3. Instead, Section 2.4 is focused on analytical analysis of the charge compensation process in cylindrical shaped pores, which has been proposed to depict the EDL charging in non-planar electrodes to represent the confined pores.

2.4 EDL models with surface curvature effects

The observed increase in specific capacitance in carbon nanopores has caught the interest of theoreticians to help in understanding the EDL formation in confined nanopores *via* advanced *in situ* techniques and simulation methods. Classical EDL models based on a 2D planar electrode were insufficient to describe the EDL formation in carbon nanopores since these 2D models do not take into account curvature and porous effects. Nanoporous carbons have pores of various shapes, including endohedral pores (cylindrical, slit, and spherical) and exohedral pores between the carbon nanoparticles (CNTs, OLCs).[29] Depending on different pore shapes, endohedral capacitors – when the electrolyte ions enter inside the pores (see Fig. 6a, b, and f) – and exohedral capacitors – ions located on the outer surfaces of carbons (see Fig. 6d and e) – were proposed.[29]

Endohedral capacitor models. Huang *et al.* proposed the first simple, heuristic model for nanoporous carbon-based

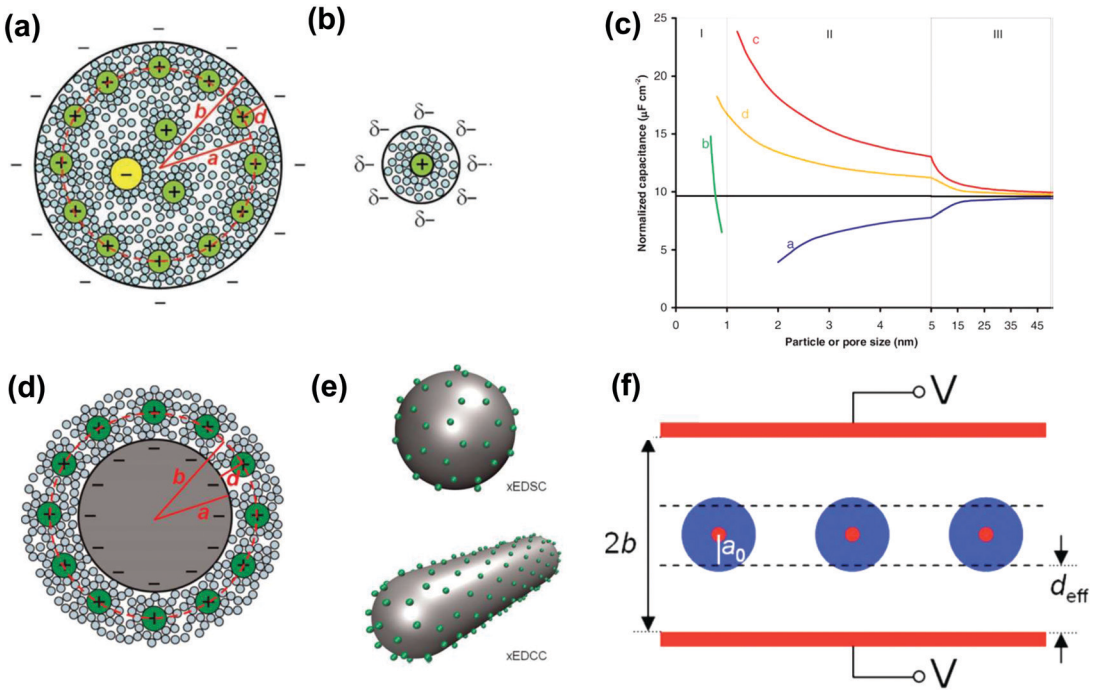

Fig. 6 Schematic illustrations (top views) of (a) an electric double-cylinder capacitor based on mesopores and (b) an electric wire-in-cylinder capacitor based on micropores. Reprinted from ref. 134, with permission from Wiley (copyright 2008). (c) Plot of specific surface-normalized capacitance *vs.* particle/pore size for endohedral capacitors (curves a and b for mesoporous and microporous carbons, respectively) and exohedral capacitors (curves c and d for 0D spheres and 1D tubes, respectively). The black line represents a parallel-plate capacitor. Schematic illustrations of (d) cross-section of an exohedral capacitor, and (e) steric views of 0D spheres (top) and 1D tubes (down) with counterions approaching the outer surface, respectively. Reproduced from ref. 140, Copyright 2010, Materials Research Society. (f) Schematic of a sandwich capacitor. Reproduced from ref. 139, Copyright 2010, American Chemical Society.

supercapacitors which include endohedral pore curvatures.[134,138] They first considered a cylindrical shaped mesopore, where the solvated ions could enter under polarization and approach the pore walls to form electric double-cylinder capacitors (EDCCs). Fig. 6a shows the schematic of the EDCC formed in a negatively charged mesopore, with the corresponding double-cylinder capacitance given by

$$C = \frac{2\pi\varepsilon_r\varepsilon_0 L}{\ln(b/a)} \quad (9)$$

where L is the pore length, and b (nm) and a (nm) are the radii of the outer and inner cylinders, respectively.

The capacitance normalized by the surface area A is given as

$$\frac{C}{A} = \frac{\varepsilon_r\varepsilon_0}{b\ln\left[\frac{b}{b-d}\right]} \quad (10)$$

where d (nm) can be viewed as the distance between the center of counterions and the carbon walls. When the pore size was reduced from mesopores to micropores, the limited space inside micropores does not allow the formation of a double cylinder; instead, the electric wire-in-cylinder-capacitors (EWCCs) were proposed by Huang *et al.* when assuming a cylindrical micropore filled with solvated (or desolvated) counterions (Fig. 6b). The corresponding capacitance is given as

$$\frac{C}{A} = \frac{\varepsilon_r\varepsilon_0}{b\ln\left(\frac{b}{a_0}\right)} \quad (11)$$

where b (nm) is the micropore radius and a_0 (nm) is the radius of the inner cylinder formed by the counterions. Note that both d from eqn (10) and a_0 from eqn (11) are approximately independent of pore size; instead, their values are related to the effective size of the counterions.[134] The EDCC/EWCC model can be further extended to porous carbons with bimodal porous distribution, which exhibit relatively narrow pore size distributions of micropores and mesopores (the contribution of macropores to the total SSA is neglected), and the capacitance is given by

$$C = \frac{\varepsilon_{r,micro}\varepsilon_0 A_{micro}}{b_{micro}\ln(b_{micro}/a_0)} + \frac{\varepsilon_{r,meso}\varepsilon_0 A_{meso}}{b_{meso}\ln\left[\frac{b_{meso}}{b_{meso}-d}\right]} \quad (12)$$

The EDCC/EWCC model was based on two assumptions: (i) the total charges of the carbon wall can be screened by the counterions inside the cylinder pore and (ii) the space charge capacitance of the carbon walls can be neglected owing to the high conductivity of carbon materials.[29] Eqn (10) and (11) indicate that the surface normalized capacitance depends on both the pore size of nanoporous carbon and electrolyte ion size. The linear *C vs. A* relationship suggested by the classical 2D model is not expected in the present EDCC/EWCC model, because of the curvature effects. Besides, the change of capacitance with carbon pore size predicted by the EDCC/EWCC model for various porous carbons in both aqueous and organic electrolyte systems (see Fig. 6c) agrees well with the experimental results (see Fig. 5b).[134,138]

Another sandwich capacitor model was proposed by Feng *et al.* by assuming the presence of slit-shaped pores.[139] Using MD simulation, K^+ ion distribution in the slit-shaped micropores was investigated by considering ion hydration and water–water interactions. As presented in Fig. 6f, the sandwich capacitor was formed by one layer of counterions located in the middle of two carbon walls with the same polarity, and the corresponding capacitance is given by

$$\frac{C}{A} = \frac{\varepsilon_r\varepsilon_0}{b-a_0} \quad (13)$$

where b (nm) is half of the slit-shaped pore width and a_0 (nm) is the effective ion radius of the counterions.[139]

Exohedral capacitor models. Exohedral capacitors can be formed on the outer surface of exohedral carbons. Fig. 6d gives the schematic illustration of a negatively charged exohedral capacitor, such as expected from the EDL charge of 0D OLCs and 1D CNTs (Fig. 6e).[140] For 0D OLCs, solvated counterions accumulate on the outer spherical surface under polarization to form an exohedral electric double-sphere capacitor (xEDSC). In the case of 1D CNTs, an exohedral electric double-cylinder capacitor (xEDCC) of solvated counterions was formed between the solvated counterions and carbon walls. The surface-area normalized capacitance of xEDSC and xEDCC is given by eqn (14) and (15):

$$\frac{C}{A} = \frac{\varepsilon_r\varepsilon_0(a+d)}{ad} \quad (14)$$

$$\frac{C}{A} = \frac{\varepsilon_r\varepsilon_0}{a\ln\left[\frac{a+d}{a}\right]} \quad (15)$$

where a (nm) is the radius of the inner sphere/cylinder charge layer, related to the carbon particle size, b (nm) is the radius of the outer sphere/cylinder charge layer, and d (nm) is the effective double-layer thickness (*i.e.* the difference between the outer and the inner diameter).

The C/A was calculated based on these two exohedral capacitor models by using a similar parameter as in the previously mentioned EDCC model, and the results are presented in Fig. 6c.[140] Interestingly, a similar increasing trend of capacitance was observed along with the decrease in carbon particle size for both exohedral capacitor models; the capacitance of the xEDSC is increased faster than that of the xEDCC. Moreover, the results obtained for the xEDCC were similar to experimental results obtained with CNTs.[141] The larger capacitance predicted from the xEDSC model compared to the experimental results obtained with OLCs[73] was explained by particle agglomeration during electrode preparation.[29]

Reasonable prediction can then be made using these simple xEDCC and xEDSC models. However, they consider the electrode charge to be entirely screened by a single layer of counterions on the carbon surface so that the electrolyte contribution to the EDL beyond the counterion single layer is negligible. This situation is unlikely to occur in solvent-free ionic liquid electrolytes where an overscreening effect arises due to the strong ion–ion correlations

in such concentrated electrolytes[36] leading to the formation of extra layers of counterions/co-ions, and improved models were proposed.[84]

Finally, although these models correctly depict the capacitance trend in carbon nanopores, the cylindrical and slit-shaped pores considered in these models are too simplistic to depict the electrode/electrolyte interface in amorphous, nanoporous carbons. To push further our understanding of the EDL formation in carbon nanopores, the combination of *in situ*, advanced experimental techniques together with modeling has been successfully proposed; this is described in the next section.

3. Understanding the charge storage mechanisms in nanoporous carbons

In this section, we broadly review the advanced *in situ* techniques and computational tools used to characterize the interfaces between carbon material and electrolyte, specially dedicated to the topic of ion confinement in nanoporous carbons during the last ten years. The *in situ* techniques include *in situ* nuclear magnetic resonance (NMR) spectroscopy, *in situ* small-angle X-ray scattering (SAXS), *in situ* infrared (IR) spectroscopy, gravimetric and dissipative electrochemical quartz crystal microbalance (EQCM) and other *in situ* and advanced *ex situ* techniques. Besides the experimental methods, simulation is an alternative and complementary approach. Here, we will simply introduce the use of some classic simulation methods, such as *ab initio*, Monte Carlo and Molecular Dynamics simulations which, in combination with experimental techniques, have pushed further the fundamental understanding of the carbon/electrolyte interface and the charging mechanisms of electrochemical double layer capacitors.

3.1 Electrochemical quartz crystal microbalance (EQCM)

EQCM is a powerful technique for monitoring the electrode/electrolyte interface and was developed by Sauerbrey in the 1950s.[142] EQCM is composed of a thin piezoelectric quartz crystal sandwiched between two metal electrodes used to apply an alternating electric field across the crystal, causing vibrational motion of the crystal at its resonance frequency. Under gravimetric mode (linear behavior), the shift of the quartz resonance frequency (Δf) can be converted into mass change (Δm) on the quartz crystal and electrodes by applying Sauerbrey's equation:

$$\Delta m = -C_f \Delta f \quad (16)$$

It has been used in different research fields due to its sensitive electrode/electrolyte interface measurement capability, such as the adsorption and detection of proteins for biology studies, the redox processes on electroactive polymer films, the electrochemical behaviors of electrolytes for lithium-ion batteries, and the details of complex electrochemical reactions.[143–146] In the last 10 years, a series of works have shown that EQCM can also serve as a useful and quantitative tool for studying the behavior of electroadsorbed ions and solvent molecules in porous carbon materials for supercapacitors.[147–152] The ion desolvation, achieved by stripping-off the solvent molecules present around the ion, was studied with porous carbons containing micropores in various electrolyte systems. The primary experimental results indicated that highly solvated Li^+ in an aprotic propylene carbonate electrolyte lost a part of its solvation shell while entering the micropores.[148] Later on, the solvation number of different cations and anions in an aqueous environment confined in nanopores was calculated.[151] By comparing with the bulk hydration number of each ion, partial desolvation was observed which agrees with the previous study in organic systems. In addition, an ion-sieving effect was observed by changing the size of cations and anions and the carbon perm-selectivity behavior was discussed by the same group.[151] In 2014, EQCM was used to study the direct relationship between ion size and pore size by using solvent-free ionic liquids (EMI^+, $TFSI^-$) and porous CDCs, whose pore size and pore size distribution can be finely tuned by controlling the chlorination temperature.[150] Two different pore sizes of 0.65 and 1 nm were selected. The results show that for CDCs with a pore size of 1 nm which is close to the size of cations and anions, cations are the only species involved in charge balance during negative polarization. Differently, under positive polarization, the ion exchange mechanism (exchange between anions and cations) is dominant at low charge density, while counterion (anion) adsorption occurs at high charge density. The experimental results are shown in Fig. 7. Similar experiments were conducted in the presence of a solvent, and the electrochemical behavior of porous CDCs was studied in 2 M EMITFSI in acetonitrile. Even in the presence of solvent molecules, the same trend has been observed: counterion (cation) adsorption at the negative electrode and mixed mechanism – so involving both co-ions (cations) and counterions (anions) – at the positive electrode. This asymmetry in the adsorption process with the electrode polarity is still under investigation and ion–carbon correlation should surely be considered.

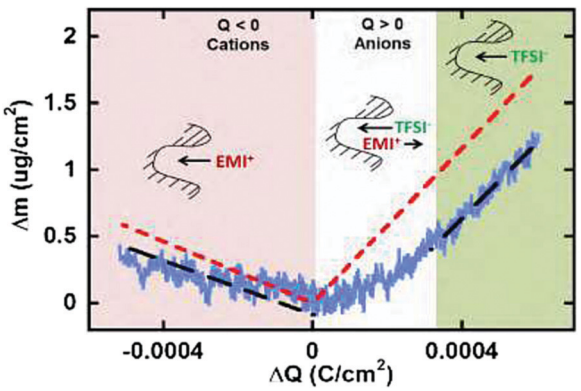

Fig. 7 Scheme of neat ionic liquid EMITFSI transport in CDC-1 nm pores during different charging states based on EQCM results. The blue solid lines represent the measured mass change (EQCM), and the red dashed lines represent the theoretical mass change of neat ions calculated from Faraday's law. The black dashed line shows the linear fitting of the measured mass change. Reproduced from ref. 150 with permission from American Chemical Society (copyright 2008).

Interestingly, the partial desolvation of ions was experimentally observed when entering carbon nanopores. EMI^+ ions enter 1 nm pores together with 3 to 4 solvent molecules around, while they are surrounded by 8 solvent molecules in the electrolyte bulk. In 0.65 nm pores, the solvent molecules number decreased down to 1–2. Additionally, apart from porous carbon materials, the ion dynamics of the EMITFSI ionic liquid has also been studied at two-dimensional single layer graphene by EQCM.[153] On this 2-D, pore-free carbon surface, an ion reorganization was assumed to be at the origin of the charging mechanisms during negative polarization.[153] These results somehow echo the previous finding of Antonietti *et al.*, who proposed that ion reorganization in neat ionic liquids could lead to increased capacitance.[154]

Since the EQCM technique appeared to be a powerful tool to characterize the electrode/electrolyte interface during operation, several improvements have been made during the past few years. The disadvantage of this technique is the drop of the quartz quality factor – because viscoelasticity – because of active material deposit, an important step is expected through the improvement of the deposition process. With this aim, recently a work has been published dealing with the development of a deposition process of different active materials onto a quartz crystal resonator. Instead of typical drop coating or spray coating, a new method by using vacuum filtration has been developed to prepare homogeneous coatings on the Au coated quartz.[155] The roughness and the homogeneity of the deposit being greatly improved, more accurate measurements are obtained with a lot less frequency noise.

Besides gravimetric EQCM, other advanced EQCM modes have been developed over the years. One of them is called EQCM with dissipation monitoring (EQCM-D). EQCM-D takes into account the mechanical properties of the film present on the quartz surface.[156–160] Basically, the mechanical properties of the deposited film on the quartz can lead to a change in the resonance frequency not in relation to a weight change of the film; as a result, Sauerbrey's equation does not apply anymore in such a situation. The dissipation factor D is the reciprocal of the quality factor and is defined by the following equation:[161–163]

$$D = \frac{W}{f} \tag{17}$$

where W is the full width at half maximum of the resonance peak (FWHM, in Hz) and f is the resonance frequency (in Hz). The loading of the coating film and the immersion in the electrolyte cause shifting of the resonance frequency and bandwidth. For example, in the case of a thin, stiff and nonporous solid electrode, there will be no change of the resonance peak width ($\Delta W = 0$), and the resonance frequency normalized by overtone order, n, is proportional to the mass change – it is worth noting that a resonator exhibits one fundamental frequency and several harmonic frequencies which usually is a multiplication of an odd number of the fundamental one. In this case, Sauerbrey's equation can be directly applied.[164,165] Differs from an ideal flat surface, in the case of a coating with porous morphology or one that is relatively soft, the viscoelastic behavior of the film will become important at higher harmonics (shorter wavelength) which results in the change of $\Delta f/n$ and $\Delta W/n$. Sauerbrey's equation cannot be used since the oscillation energy dissipates across the film's width.[162,163,165–167] This has raised the attention within the community since previous studies of EQCM did not consider the structural parameters of the coating. Another *in situ* technique which is an extension of EQCM-D is *in situ* hydrodynamics spectroscopy. This technique focuses on the trapped or movable liquid inside the porous materials by observing the change of penetration depth (δ_n) with $\Delta f/n$ and $\Delta W/n$.[168] The use of EQCM-D to study the electrode/interface in the electrode for energy storage materials has been pioneered by Levi and Aurbach.[145,147–149,151,169] By analyzing the mechanical properties of the deposited materials, studies have shown that the selection of a binder is crucial, whose viscoelastic behavior can vary based on the electrolyte environment, affecting in turn the accuracy of the EQCM results.[169–171] The analysis of EQCM-D signals and its subsequent modeling using complex equations and models allow for collecting textural, structural and mechanical data of the coating.[160]

Despite the fact additional mechanical information can be extracted by monitoring the dissipation, EQCM used in gravimetric and dissipation modes has still some limitations. For instance, since an electrolyte is a mixture, it is difficult to break down clearly the respective contribution of each single species: individual ions, solvent molecules. For this aspect, ac-electrogravimetry (ac-EQCM) has been shown to be a great tool to help deconvolute the role of each involved species in the charge exchange process; interestingly such a technique gives access to rate constants.[172–176] Escobar-Teran *et al.* used ac-EQCM to study the electrochemical behavior of carbon nanotubes in complex aqueous electrolytes.[173] In this work, the authors first established charge/potential and electrogravimetric transfer functions considering all ionic species involved. Then, the transfer functions were used to fit the experimental results by playing with two kinetic parameters: K_i and G_i, respectively, accounting for ion and solvent molecule transfer at the interface and conductance. Fig. 8a and b present the experimental transfer functions $\frac{\Delta q}{\Delta E}(\omega)$ and $\frac{\Delta m}{\Delta E}(\omega)$ fitted by theoretical equations. With the change of frequency, as shown in Fig. 8b, the different ionic species can be distinguished. From Fig. 8c, the result shows that the hydrated Na^+ ion mass transfer is surprisingly faster than that of protons, *i.e.* K_i ($Na^+ \cdot H_2O$) > K_i (H^+). Moreover, the relative concentration change of individual species can be estimated by ac-EQCM which allows distinguishing between the contributions of the different ionic species to charge storage in nanoporous carbon (Fig. 8d). Although this technique is complex to set up and use, the ionic fluxes in carbon nanopores during the charge/discharge process can be analyzed in detail.

3.2 Nuclear magnetic resonance spectroscopy (NMR)

To observe and quantify the ion environments in porous carbons, nuclear magnetic resonance spectroscopy (NMR) is one of the promising techniques to work with.[177–180] The working principle of NMR dedicated to the ion confinement in nanopores is based on the shift of resonance of the target electrolyte ions to lower

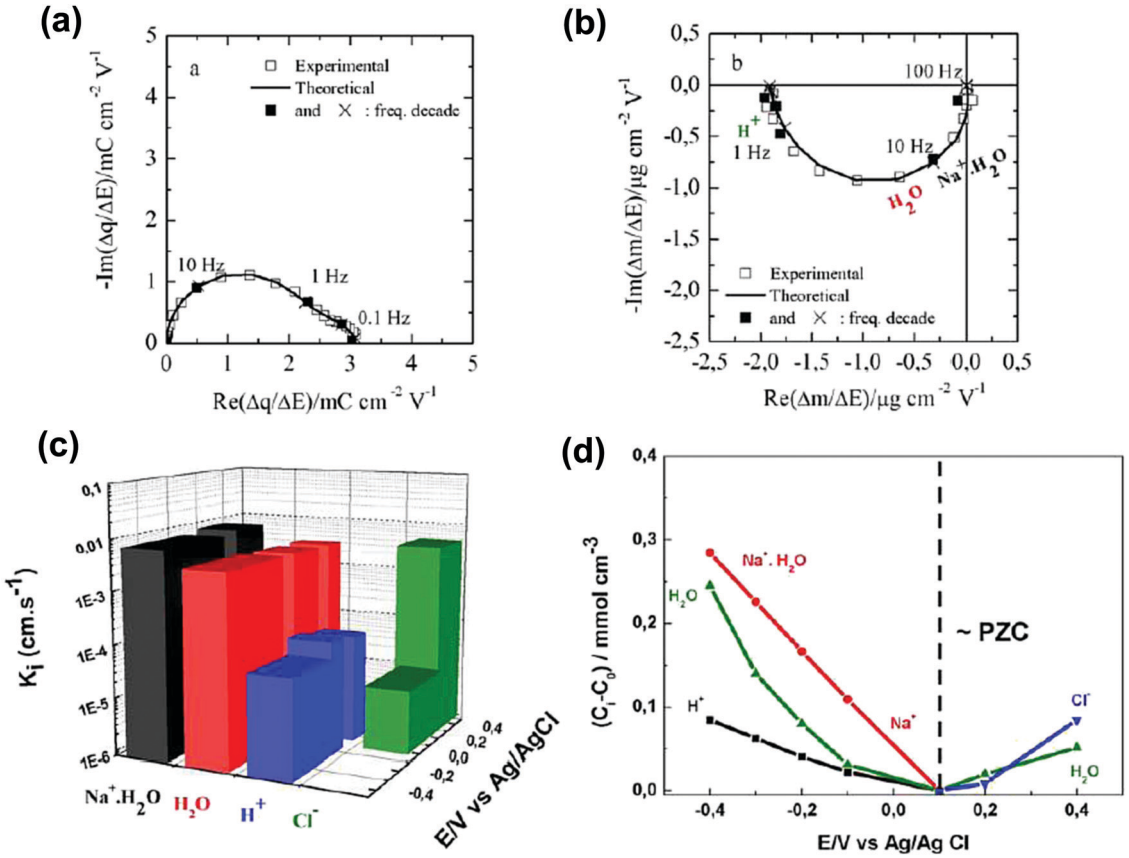

Fig. 8 (a) and (b) The transfer functions $\frac{\Delta q}{\Delta E}(\omega)$ and $\frac{\Delta m}{\Delta E}(\omega)$ at −0.4 V *vs.* Ag/AgCl, respectively. (c) The kinetic parameters K_i (cm s^{-1}) for each ion at different applied potentials. (d) Relative concentration variation of each ion in SWCNT based thin films as a function of potential in 0.5 M NaCl at pH = 7. Reproduced from ref. 173 with permission from Elsevier (copyright 2016).

frequency because of the delocalized electron distribution present at the carbon surface that shields the signal. The chemical shift difference between the resonances of ions confined inside nanopores and the neat electrolyte is defined as $\Delta\delta$. With the help of density functional theory (DFT) calculations, $\Delta\delta$ is found to be related to the intrinsic electronic structures of carbon, carbon structure and pore size distribution.[103,181,182] Studies show that this so-called nucleus-independent chemical shift (NICS) allows for distinguishing the ion confined within carbon pores, as well as the ion population.[181–185]

In 2006, Lee *et al.* used *ex situ* magic angle spinning (MAS) NMR to study ion adsorption in porous carbon in organic electrolytes.[186] Solid state ^{11}B NMR spectra could distinguish between the BF_4^- anions located outside and inside the pores at the open-circuit voltage (OCP), charged, and discharged stages. The same technique was used to obtain the relative concentrations of cations, anions, and solvents inside or outside the carbon porosity. Moreover, the exchange of ions from the adsorption site to the free state of the electrolyte can be characterized using two-dimensional ^{12}C and ^{11}B NMR exchange spectra.[187] To avoid cell dismantling needed for *ex situ* NMR analysis, *in situ* NMR has been developed by Grey's group which allows tracking the change of the local environment in porous carbon in real-time as well as the charge storage mechanisms *operando*.[180,188,189] A detailed work aiming at understanding the electric double layer structure in microporous carbon YP50F in tetraethylphosphonium tetrafluoroborate (PEt_4BF_4) with acetonitrile has been published by combining *in situ* NMR and EQCM.[185] *In situ* NMR results showed the evolution of the absolute ion population of cations and anions confined in carbon nanopores at various states of charge. Two charging mechanisms were identified, depending on the electrode polarity. During negative polarization, the charge is stored by counter-ion (cation) adsorption, while ion exchange was the charge storage mechanism during positive polarization. On the other hand, similar results were obtained by EQCM which suggests a concomitant solvent reorganization in the pores, with no net solvent flux in and out of the porous network. This combination provided a direct insight into the molecular level of the charging process in carbon micropores.

Another microporous carbon material TiC-CDC has also been studied by *ex situ* NMR, in 1 M NEt_4–BF_4 in an acetonitrile organic electrolyte. The NMR results show in-pore and ex-pore features of ions in NMR spectra.[182] Fig. 9a and b show the experimental results with the signals corresponding to in-pore NEt_4 and BF_4 ions highlighted in red. Furthermore, the structural characterization of TiC-CDC nanoporous carbons was realized by combining *ex situ* NMR and Raman techniques.[103]

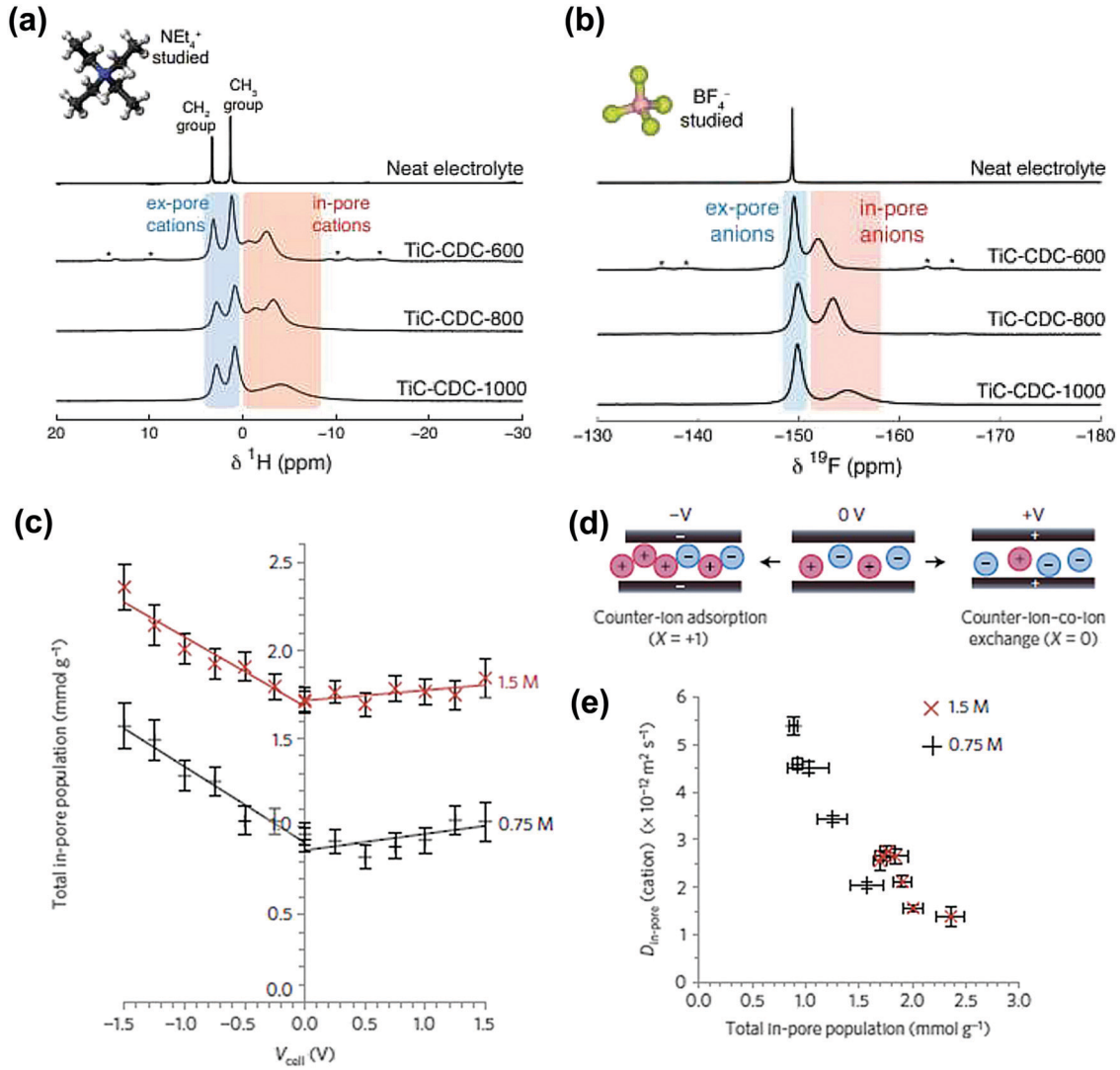

Fig. 9 (a) ^{1}H and (b) ^{19}F MAS (5 kHz) NMR spectra of cations and anions filled pores TiC-CDC soaked with NEt_4–BF_4 in acetonitrile. The figure is reproduced from ref. 182 with permission from Elsevier (copyright 2014). (c) Calculated total in-pore ion population of the YP-50F electrode in 1.5 M PEt_4BF_4 in ACN at different potentials. (d) Scheme of the charge storage mechanism at positive, 0 V and negative charge. At 0 V, there is an equal number of cations and anions in the pores of the carbon electrodes. (e) Correlation between $D_{in\text{-}pore}$ (cations) and total in-pore ion population. The figure is reproduced from ref. 190 with permission from Springer Nature (copyright 2017).

Lately, *in situ* pulsed field gradient NMR has been introduced to explore the ionic transport in porous carbon electrodes.[190] As can be seen from Fig. 9c, the total in-pore ion population increased from 0 V to negative potential while the in-pore diffusion coefficients ($D_{in\text{-}pore}$) decreased significantly for both cations and anions (Fig. 9d). In addition, the difference of electrolyte concentrations indicates that with less ions confined in nanopores, $D_{in\text{-}pore}$ will increase because of the reduced ion–ion interactions. This study emphasizes the strong correlation existing between the charging mechanisms and ion dynamics for microporous carbon electrodes.

3.3 Small angle scattering (SAS) techniques

SAS techniques are well-known to be efficient techniques for characterizing three-dimensional structures at the micro- and mesoscopic scale,[191–196] using X-rays or thermal neutrons. Small angle X-ray scattering (SAXS) has been widely used for porosity characterization for carbon materials.[197–199] Iiyama *et al.* firstly operated advanced *in situ* SAXS to study the formation of cluster-like water molecules adsorbed in activated carbon fiber micropores.[200] Further on, SAXS also demonstrated its ability to study the adsorption of gas molecules in nanoporous carbon.[201]

Since then, lots of studies based on *in situ* SAXS have revealed interesting facts during polarization of the nanoporous carbon electrode. For instance, some inaccessible micropores at OCP can be filled with the electrolyte under polarization, when the carbon electrode overpotential was large enough.[197,202] This mechanism was proposed since the electron density contrast decreased greatly and was barely reversible.

Besides, ion confinement in carbon micropores has also been studied with SAXS.[203] By combining *in situ* SAXS and Monte Carlo simulation the degree of confinement (DoC) of ions in micropores has been reported for an aqueous-based electrolyte.[128] Fig. 10a shows an illustration of an example of a different DoC. The calculated DoC is based on Monte Carlo simulated *in situ* SAXS data. For carbon with different pore sizes, the ion number and shape of the histogram at different DoC vary (see Fig. 10b). We can observe that at the positive or negative charge, more charge-induced ions were confined in smaller pores (with higher DoC). The influence of a confined environment on in-pore ion concentration was pointed out. From Fig. 10c, at higher DoC sites, the surface charge density is higher (red). Thus, comparing the dashed circles in Fig. 10c for AC1 and CDC samples, the counterions are more localized at higher DoC and higher charge density sites (darker red) for 0.65 nm pore size CDC. If more counterions moved to higher DoC sites during charging, the repulsion of counterions can be minimized reducing the energy cost. With DoC, the degree of desolvation of ions (DoDS) can also be obtained (from the first solvation shell). In this article, they summarized that pore size is not the only factor impacting the capacitance for carbon-based supercapacitors, and that DoC, DoDS and the size dispersity of the carbon electrode are required to be considered thoroughly.

Ionic liquids have been found to have a higher density of cations and anions confined at the center of the pore. With the help of molecular dynamics simulations, the authors concluded that the interaction between ionic liquid and carbon walls is stronger than the bonding of the ion pairs, resulting in a denser and less coordinated ions packed in the micropores. With the same methodology as the previous study, Futamura *et al.* revealed the structure of ionic liquids confined in TiC-CDC nanopores with the confirmation of a superionic state for EMIFSI and $EMIBF_4$ ionic liquids confined in small 0.7 nm nanopores.[204] The coulombic ordering was preserved in larger 1 nm nanopores under ion confinement. The partial breaking of the coulombic ordering – superionic state – was observed when monolayer confinement occurred due to the existence of image charges in the carbon walls that partially screen the repulsive electrostatic interaction between co-ions.

SAXS also provides information about the carbon structure and the electrolyte organization. Prehal *et al.* studied the structural and concentration change of ions confined in micropores during polarization, by acquiring the electron density

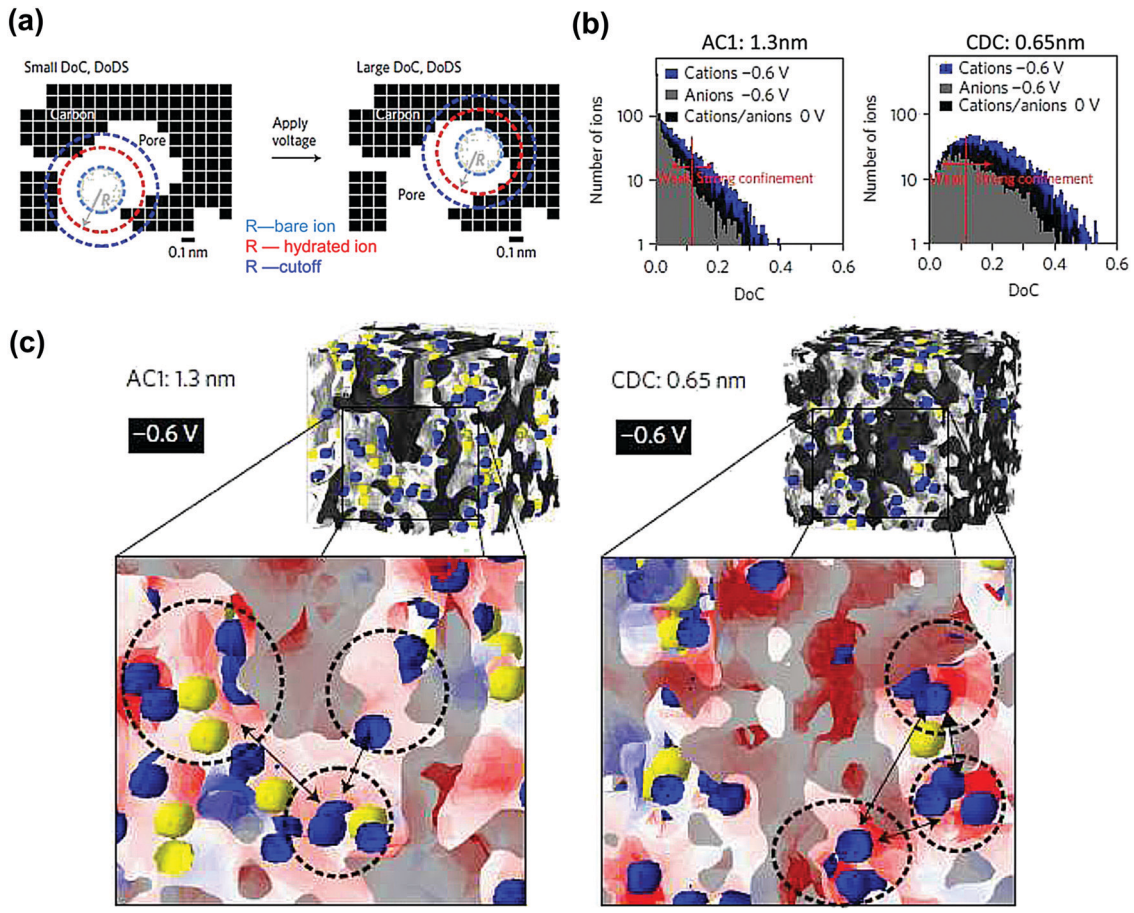

Fig. 10 (a) A 2-D cross-section drawing demonstrating the concept of degree of confinement (DoC) and degree of desolvation (DoDS) in 3-D micropores. (b) Histograms of ion number corresponding to selected DoC at different charge state for AC1 and CDC samples in 1 M CsCl. (c) A 3-D view of the distribution of cations (blue) and anions (yellow) at −0.6 V for AC1 and CDC samples. The red and white areas indicate high negative surface charge density and zero electric fields, respectively. The figure is reproduced from ref. 128 with permission from Springer Nature (copyright 2017).

profiles in various aqueous electrolytes, such as NaCl, KCl and CsCl.[205] They first evidenced three regions from SAXS curves, shown in Fig. 11a. At the small value of scattering vector modulus Q (<0.7 nm^{-1}), a part of the decay of the SAXS intensity is due to large pores between the activated particles. The second region between 0.7 and 5 nm^{-1} indicates the scattering from disordered micropores, which is described by the Debye–Anderson–Burmberger (DAB) model.[206] At a larger Q value (>5 nm^{-1}), the molecular structural factors of carbon and electrolyte govern. The intensity of the SAXS signal represents micropores filled with the electrolyte (blue line) is lower than that corresponding to empty pores (black line) until a large Q value is reached (WAXS signal). This result agrees with the literature: the SAXS contrast decreases once the micropores are filled with the electrolyte.[207] On the other hand, the increase of electron density contrast at higher Q values for the blue line is the consequence of the addition of the electrolyte molecular structure factor to the carbon structure factor. Since the value of the electrolyte structure factor depends on the type of ions and their concentration,[208] the intensities of different composition of ions in the three aqueous electrolytes are expected to vary at a larger Q value as shown in Fig. 11b. All aqueous electrolytes show a maximum intensity at positive and negative potentials (Fig. 11c–e). With the radius of gyration (R_g) obtained from Guinier analysis of the SAXS data and the average electrolyte electron density (ρ_{el}) measured by X-ray transmission, a model was proposed to fit the SAXS intensity changes *versus* potential which corresponds to the change of the electrolyte local environment near the micropore wall. At low charge density, ion swapping dominates the charge storage mechanism, while at higher charge density, not only counterion adsorption was involved in the charging process, but also local in-pore ion rearrangement took part. Counterions stay closer to the pore wall, resulting in a denser layer of ions and solvents.

The SAXS technique has also been useful to study the influence of the porous carbon texture and structure on the capacitive performance, especially the volume fraction of inaccessible pores, the shape of pores and the pore organization, which are key parameters controlling the ion confinement in nanopores.[209] In addition, Koczwara *et al.* proposed an advanced SAXS technique called *in situ* anomalous small angle X-ray scattering (ASAXS), for characterizing both the structural change of pores and the concentration change of the in-pore ions at the same time.[210] However, more equipment and theory are required to develop this technique for further electrolyte systems.

Small angle neutron scattering (SANS) involves scattering nuclei which may result in different scattering signals, especially the presence of micropores in carbon materials.[211] Compared with other scattering techniques, SANS is easier to use "contrast-matching" to detect the closed porosity inaccessible to electrolytes.[212,213] Some works have shown its ability to

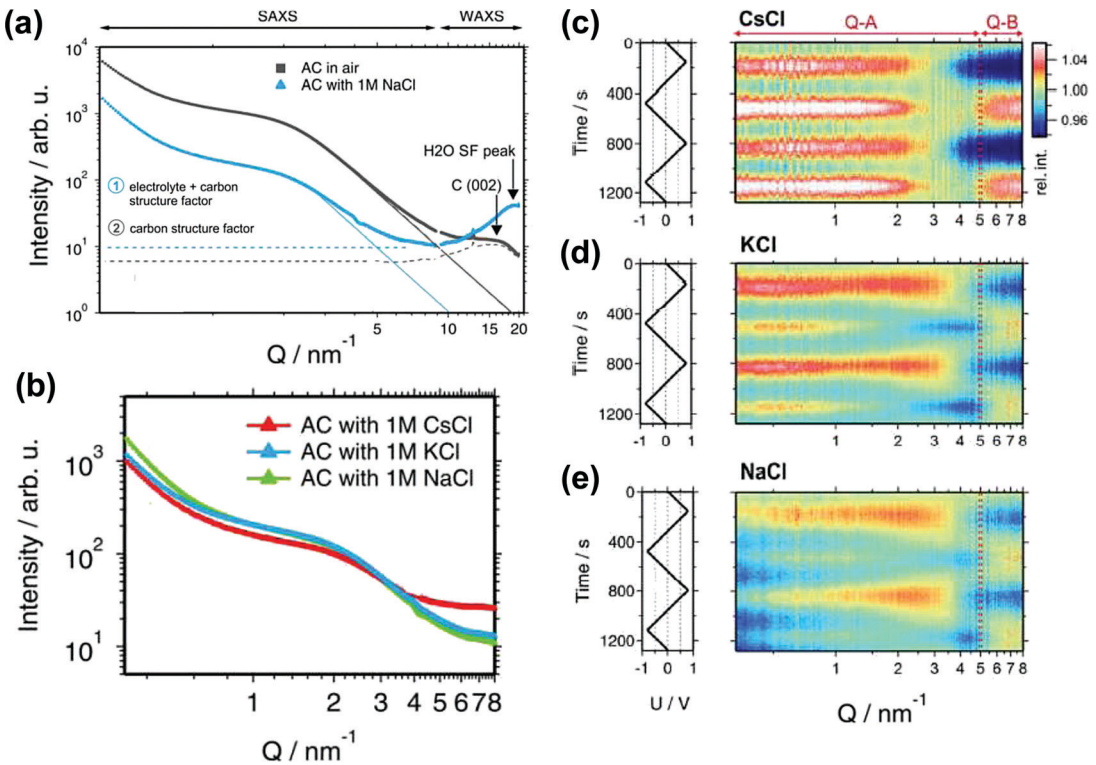

Fig. 11 (a) SAXS and WAXS intensity for the activated carbon in air (black) and filled with a 1 M NaCl electrolyte (blue). (b) SAXS intensity for the AC filled with three different electrolytes: 1 M CsCl, KCl and NaCl. (c)–(e) *In situ* SAXS results for various electrolytes. The left rows show the applied voltage signal as a function of time. The right rows are the scattering intensity normalized to the intensity at 0 V as a function of time and the scattering vector length Q. The figure is reproduced from ref. 205 with permission from Royal Society of Chemistry (copyright 2015).

characterize microporous carbon materials.[116,192,196] The variation of contrast was also observed when the micropores of carbon nanotubes were filled with a liquid.[214] Yushin's group pioneered *in situ* SANS to reveal the electroadsorption of organic electrolyte ions in carbon pores of different sizes in aqueous and organic systems.[215,216] They observed electrowetting – enhanced ion sorption in subnanometer pores under an applied potential – counterbalancing the high interfacial energy of the carbon/electrolyte interface in small pores.

In summary, the development of experimental *in situ* SAS techniques has been a key for pushing further our basic understanding of ion confinement in carbon nanopores and charging mechanisms of EDLCs.

3.4 Other *ex situ* and *in situ* characterization techniques

X-ray diffraction (XRD) is commonly used to describe the structural features of carbon materials.[217–221] Kaneko's group firstly demonstrated the use of XRD to study C_2H_5OH gas sorption in slit-shaped micropores of activated carbon.[222] Later, they used the same methodology to analyze organic electrolytes ($TEABF_4$ in propylene carbonate) confined in the micropores of CDC and activated carbon fiber (ACF).[223] Fig. 12a shows the synchrotron XRD patterns of porous carbons and porous carbons impregnated with the electrolyte. Fig. 12b represents the corrected XRD patterns, obtained by removing the contribution from the carbon in Fig. 12a. By comparing the bulk and the confined electrolyte signals and with the help of Monte Carlo simulations, a visual view of the ions confined in micropores was obtained. The simulated XRD patterns are comparable to the experimental results, as shown in Fig. 12c. This study shows the interest of synchrotron XRD to study the electrolyte confinement in microporous carbons.

In situ infrared spectroelectrochemistry, also known as attenuated total reflectance-surface-enhanced infrared adsorption spectroscopy (ATR-SEIRAS), has also delivered some key insights into the ion dynamics in porous carbon materials. This

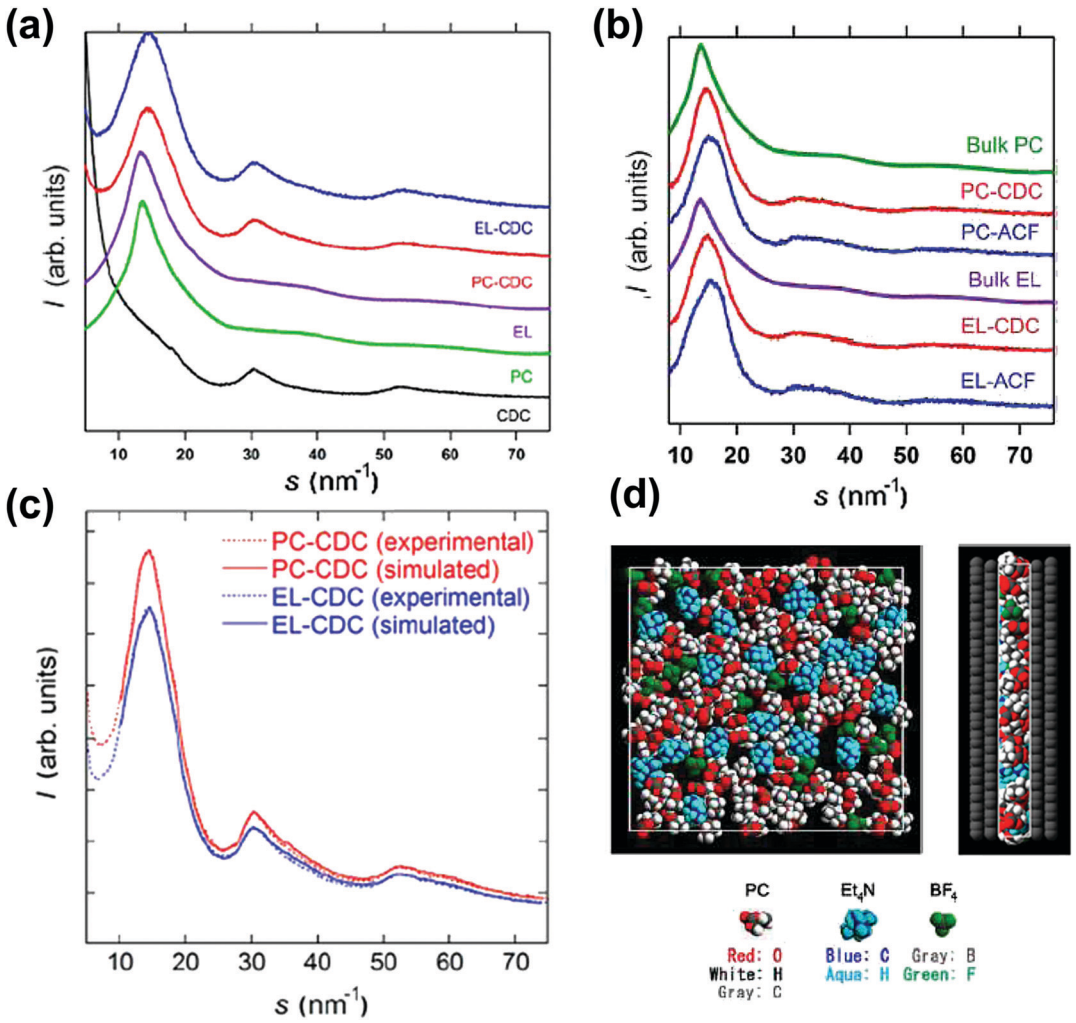

Fig. 12 (a) XRD patterns of CDCs, PC, EL, PC-impregnated carbon (PC-carbon), and $TEABF_4$–PC-impregnated carbon (EL-carbon). (b) Corrected XRD patterns of PC and $TEABF_4$–PC confined in the pores of CDC and ACF and the XRD pattern of bulk PC at 303 K. The same for EL carbons. (c) Experimental and RMC-simulated XRD patterns. (d) Top and side views of the snapshot of $TEABF_4$–PC confined in the pores of CDC from RMC simulation. The figure is reproduced from ref. 223 with permission from American Chemical Society (copyright 2008).

technique was first introduced by Richey *et al.* to study the interface between ionic liquid EMITFSI and pseudocapacitive RuO_2 electrode, for probing the ion dynamics during the charging process.[224] The technique is based on the infrared adsorption of the molecules at the solid/liquid interface, which is called surface enhanced infrared adsorption (SEIRA).[225] This results in a local increase of the electromagnetic field, so the chemical changes at the surface of the material can be detected.[226]

Carbon materials such as carbon onions, CDCs and nanoporous carbon nanofibers were studied in ionic liquid systems by combining electrochemical measurement and *in situ* infrared spectroelectrochemistry.[224,227,228] This technique allows for tracking the ion concentration change in the porous network. Infrared spectra were collected at different concentrations of cations and anions (Fig. 13a). This allows the calibration of the concentration of cations and anions, which can be plotted with the absorbance of infrared (Fig. 13b). As a result, the concentration of cations and anions can then be extracted from the infrared spectra during polarization. For example, from Fig. 13c, while the carbon nanotubes were charged from −0.5 to 1.5 V, the number of anions increases drastically compared with that of cations. As a result, it proposes that a larger concentration of anions is located in the nanopores of the nanofibers at higher voltage, although both ions are still present.

Another *in situ* technique that was recently used to characterize ion confinement in nanopores is *in situ* dilatometry. Hantel *et al.* pioneered the technique to study the pore expansion/extraction and ion sieving effect during cycling of different carbon materials.[229–231] They observed that the strain change at positive and negative polarization was asymmetric.[229,232] A study combining *in situ* SAXS and dilatometry showed that the strain increased with the increasing amount of micropores. This result is related to the combination of total ion concentration (cations and anions) change during charging with a higher amount of micropores and the electron/hole doping causing the elongation of C–C bonding.[233] A further study showed that in the ionic liquid system, with a different size of anions, the organization of ions confined in nanopores varies.[234] This can be observed by dilatometry because the strain of pores is sensitive to ion adsorption/desorption, orientation, and transportation. Also, this technique evidenced the importance of the ion valence state during electrosorption in carbon nanopores from aqueous electrolytes.[235] Rochefort's group used *in situ* dilatometry combined with solid state NMR to study ion fluxes in porous materials in biredox electrolytes.[236] In these experiments, the dilatometry measurements helped in resolving the charge storage mechanism in carbon pores, in the presence of redox moieties in the electrolyte. They confirmed the ion exchange mechanism at low potential and

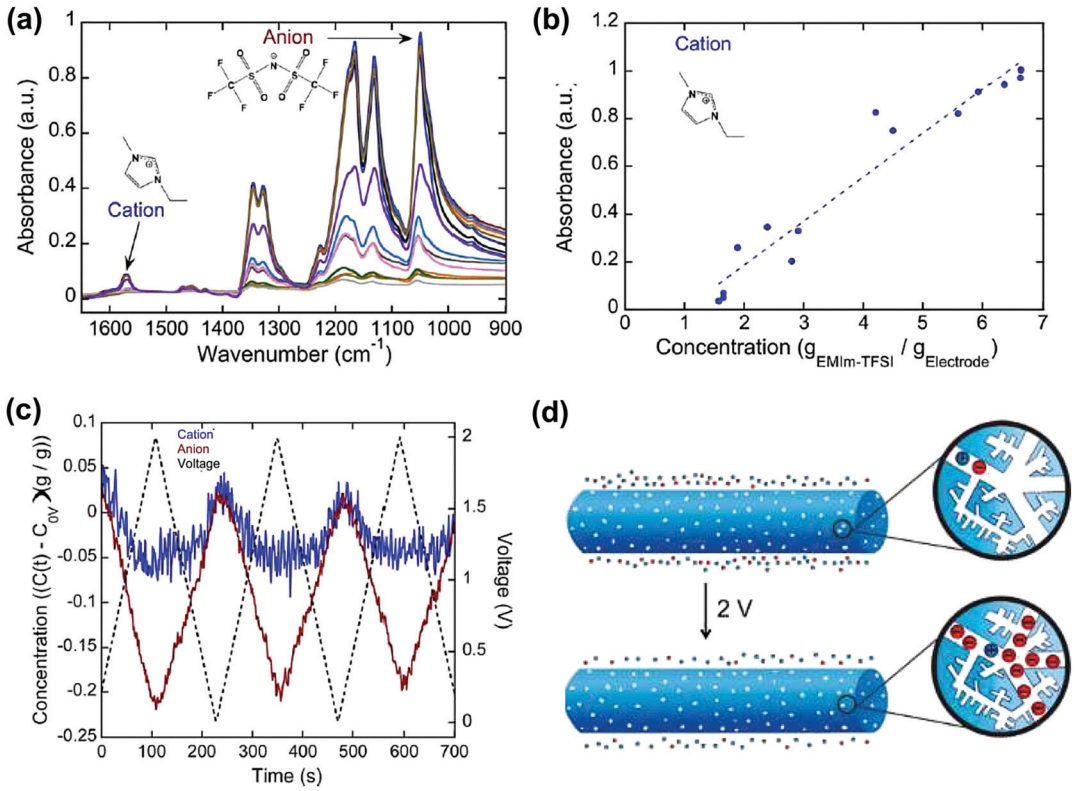

Fig. 13 (a) Infrared spectra of the NCNF electrodes with varying concentrations of the EMITFSI electrolyte (1.6 to 8.8 $g_{EMIm-TFSI}$ $g_{electrode}^{-1}$). (b) Concentration–absorbance calibrations of the cation. The dotted lines represent linear regressions. (c) *Operando* infrared spectroelectrochemical results show the initialized time-resolved concentration ($g_{EMI-TFSI}$ $g_{electrode}^{-1}$) of EMI^+ cations and $TFSI^-$ anions in NCNFs from 0 to 2 V at 20 mV s^{-1}. (d) Illustration showing that a larger concentration of $TFSI^-$ anions than EMI^+ cations is in the nanopores of the positively charged NCNF nanopores. The figure is reproduced from ref. 228 with permission from American Chemical Society (copyright 2008).

counterion adsorption at high potentials at the positive electrode, while only counterion adsorption occurred at the negative electrode.

During the recent past year, new *in situ* techniques were introduced to the community. *In situ* electrochemical atomic force microscopy (AFM) has shown the transition of layering of ionic liquids and the orientation of cations and anions from zero volt to the applied voltage on graphite materials.[237] Several studies carried out by *in situ* scanning tunneling microscopy (STM) demonstrated the interaction and structural change of ionic liquids at the surface of a polarized metal electrode.[238–240] These techniques are useful for investigating the electrode/electrolyte interface. To understand the EDL changes during polarization, *in situ* vibrational spectroscopy measurements were made in an organic electrolyte system.[241] Combined with MD simulation, the solvation shell of charged ions and the compositional change of the EDL were observed. This technique can serve to establish modern EDL models for ionic liquid and concentrated electrolyte systems. To study the ion dynamics, in complement to EQCM and classic *in situ* NMR techniques, *in situ* nuclear magnetic resonance imaging (MRI) has been proposed, pioneered by Grey's group for energy storage study.[242] A 1-dimensional ion concentration profile was recorded during the charge/discharge of a supercapacitor cell.[243] This approach gives a visual and realistic view of the interactions of ions and carbon electrodes inside the electrode and in the cell, which can be also useful for industrial purposes.

3.5 Modeling and simulation

A lot of work has been dedicated to modeling the interface of electrode materials and electrolytes. We will highlight in this section some works focusing on ion confinement in nanoporous carbon-based materials.

After the experimental discovery of the capacitance increase in carbon nanopores smaller than the solvated ion size, various nanoporous carbon structures and electrolytes have been used for modeling not only to improve the theoretical EDL models but also to resolve the underlying theory and predict optimized carbon structures.[36,82,83,138,139,244–249] For example, in aqueous electrolytes, the desolvation process of ions in nanopores has proven to be crucial to explain their transport properties using molecular dynamics (MD).[246,250,251] However, the origin for such a phenomenon was not yet clear until the group of Kornyshev brought up the "superionic state" of ions confined in nanopores.[252] A schematic overview is shown in Fig. 14a. The superionic state, recently confirmed by experimental SAXS measurements as mentioned before,[204] is attributed to two effects. Firstly, the metallic properties of carbon materials weaken the electrostatic interactions of ions, resulting in breaking the Coulombic ordering of ions in the nanopores, by the creation of image charges. Second, the negative free energy of ions entering the pores from the bulk due to the desolvation of ions favors the increase of ion density inside the pores. They applied mean field theory on a slit-shaped pore model and reproduced the capacitance increase *versus* pore width. The comparison results are displayed in Fig. 14b. In addition, the transition from ion-rich-

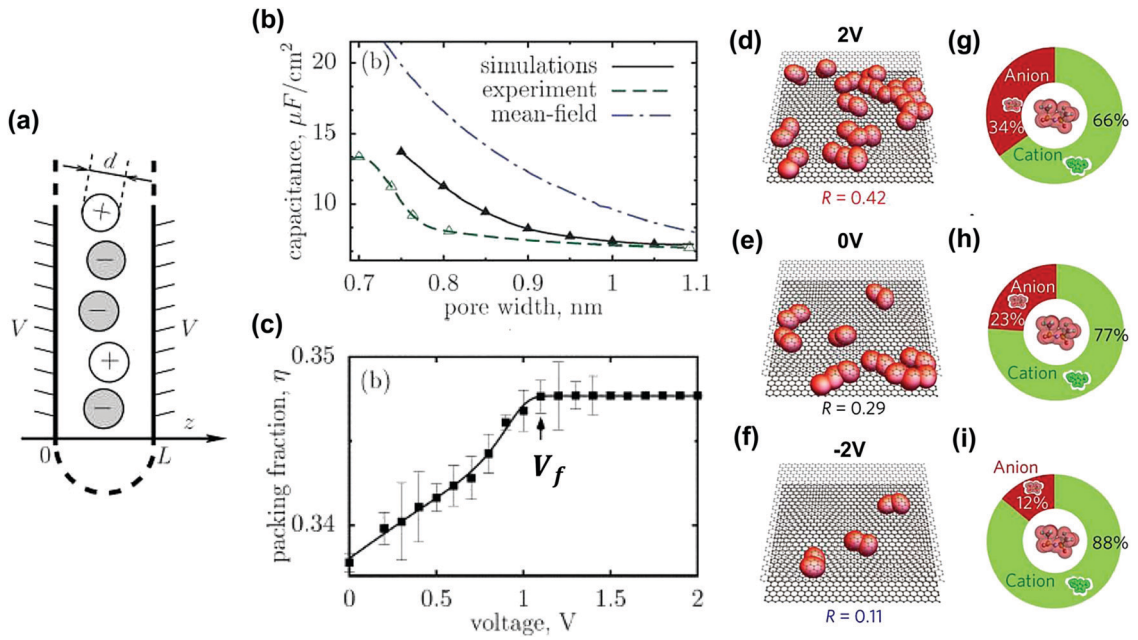

Fig. 14 (a) The cross-section of a single, laterally infinite, slit-like narrow pore as a part of a porous electrode (*L*: pore width; *V*: applied voltage; *d*: diameter of ions). (b) Differential capacitance per surface area *versus* pore width. Evidence of capacitance increase in carbon nanopores by using different approaches: (c) the packing ratio at different voltage. At V_f, the total ion density reaches its maximum. (d–f) Visual views of co-ion pairs of anions of EMITFSI (*R* is the anion–anion pair ratio) and (g–i) the population in the first coordination shell around a TFSI anion in the 0.7 nm pores under 2, 0 and −2 V. Reproduced from ref. 204, 252 and 253 with permission from IOP Publishing (copyright 2010), Royal Society of Chemistry (copyright 2011), and Springer Nature (copyright 2017), respectively.

to ion-deficient nanopores was observed when reaching a threshold voltage V_f as shown in Fig. 14c.[252] Further on, they modified and investigated deeply the same model using Monte Carlo simulation for ionic liquid systems and ended up with simulation results closer to experiments.[14,253] Experiments had proven the superionic state of ions in nanopores.[204] Fig. 14d–f shows different anion–anion pair ratios (R) at different applied potentials. In the first coordination shell of the $TFSI^-$ anion, there was also an existence of anions as calculated from Fig. 14g–i. For slit-shaped pores like carbon models, a fundamental work was proposed by Palmer *et al.* using quenched MD simulation.[254] They built up a realistic carbon model in which the carbon structure changes with chlorination temperature such as observed for TiC-CDC materials. This establishment pushed further the modeling closer to reality.

Differently from the slit-shaped pore structure of porous carbon, another model based on cylindrical micropores was one of the first models proposed to mimic the ion confinement effect in carbon nanopores.[138] Huang *et al.* simulated a series of organic electrolytes and their results aligned with the experimental results showing that the optimal capacitance was obtained when the ion size is close to the nanopore size. For both slit-shaped pore and cylindrical pore models, overscreening and crowding are not considered to happen in the ionic liquid system, such as can be observed when using a classic double layer model at planar electrodes.[38,138]

In a cylindrical model, the curvature of the electrode is an important difference compared to the slip-pore model. A few modeling works have mentioned the effect of curvature over the years.[84,140,255–257] Merlet *et al*. used MD simulation to characterize different sites with various morphology of CDC materials (edge, plane, hollow and pocket) and calculate the degree of confinement of the adsorbed ions.[256] The results showed that at the edge, plane, hollow and pocket sites (with the increased degree of confinement) of CDC samples, the degree of desolvation of anions varies compared to the bulk. Electrowetting of the smallest pores at high potential was also observed. This study not only raises the idea of a better way to confine ions in nanopores but also establishes the importance of how the carbon structure influences the ion confined environment, for further experimental and simulation works. To characterize precisely the porous structure of carbon materials, the DFT method is frequently used to estimate the pore size distribution and accessible surface area from gas sorption experiments.[111,258–260] For carbon materials, which are relatively rough and contain more functional groups on the surface, QSDFT is found to be preferable to characterize microporous and mesoporous carbons.[261–263] Classic DFT and molecular DFT (MDFT) can be used to calculate the free energy of solvent which is very useful information while discussing the desolvation of ions, especially for aqueous and organic electrolyte systems, confined in nanopores.[264–273] Following on, we will introduce in the next section a few simulation methods which are frequently used for modeling the ion confinement in nanopores, starting with Monte Carle simulations.

The working principle of MC is based on the statistic of the ion movements and sampling the probability of an organization based on anion and cation number, ion-pair number and potential energy of the system at the molecular level.[274–277] The potential energy considers the interaction between ions, ion and electrode, and electrodes. The movements of ions in this simulation include ion exchange, migration, insertion in electrodes, and also charge balance and transfer between anode and cathode. MC simulations run for million steps to reach the equilibrium of the system. Different electrode setups (planar to porous) and electrolyte systems have been studied by MC simulation.[204,252,253,275,278–281] As mentioned before, the superionic state of ionic liquids has been studied by this method, which was also used to evidence the oscillation of capacitance in the ionic liquid system.[282] Later on, Kornyshev's group used MC to discuss the effect of ionophilicity and ionophobicity of slit-like nanopores on the improvement of the energy density for supercapacitors.[281] Unlike DFT, the MC method can simulate three-dimensional porous carbon, leading to a better view of the electrode/electrolyte interface.[283–286]

Another method also achieved at the molecular level is MD simulation. For EDLC related topics, MD simulation models the system by simulating the ion movements according to Newton's second law.[287,288] There are two different ways to build up polarized electrodes. In the earlier time, most of the work based on MD simulations applied fixed charges to each carbon atom.[83,84,245,246,250,251,289] However, in 2012, Salanne's group pointed out that the electrolyte responses to constant charge and constant potential applied to an electrode are distinct.[290] Applying a constant potential, especially for porous carbon materials, results in a more realistic way to model the system by limiting energy dissipation (temperature increase is limited) and does not stray from equilibrium.[290–292] However, the cost remains an issue for further applications. After discovering the anomalous increase of capacitance with sub-nanometer-sized pores, MD simulation was used to provide an insight at the molecular level into the electrolyte organization in carbon pores. The ionic structure of an ionic liquid confined in disordered microporous carbon was shown by MD simulation in 2012.[293] Afterwards, the arrangement of ions in carbon micropores and mesopores was studied with various combinations of ionic liquids.[43,203,294–298] The greatest advantage of MD simulation is the possibility of modeling the charging dynamics in nanopores. As shown in the previous section, there are mainly three charging mechanisms: counter-ion adsorption, co-ion desorption, and ion exchange. Over the years, MD simulation has proven that ion dynamics and transport properties of ions play an important role in improving the performance of supercapacitors. The origin of the increase of capacitance in nanopores and further improvement (fast ion transport) is not only due to the structure and texture of the carbon but also due to the combination of ion exchange and ion adsorption mechanisms during charging.[293,299,300] The diffusion coefficients of the in-pore ions have also been related to the power performance of charging nanoporous carbon.[301–305] Interestingly, Kornyshev *et al.* suggested an accelerating charging dynamics of ionic liquids in subnanometer ionophobic pores,[301] and a recent simulation study observed a similar charging

behavior.[304] This enhanced charging dynamics in pores smaller than 1 nm was innovative compared to the conventional views that larger pores provide faster charging, and offered an exciting opportunity for designing ionophobic porous materials with both high energy and high power performance.

Classical coarse-grained simulation methods at the molecular level (MC and MD) share the disadvantage of considering ions as spheres, most of the time, for the sake of simplicity and cost. For a deeper investigation of the interaction between ions and carbons at the electrode/electrolyte interface, especially during polarization, more realistic atomistic approaches are required, such as *ab initio* simulations, which can capture molecular geometry and polarization. *Ab initio* simulation takes into account not only all the atoms or ions or molecules but also the electronic structure of carbon materials. During polarization, the screening potential and structure of the EDL are affected by the change of the electronic structure of the carbon electrode and the electrostatic interactions between ions. Classic DFT and other advanced DFT methods are mostly used for *ab initio* simulation. As mentioned above, DFT is useful to probe the porous carbon structure and texture. It also explains the origin of the capacitance increase in nanopores in terms of the positive curvature of carbon nanopores.[84,140] Apart from the morphology of porous carbon, during the last decade, DFT calculations were utilized to study the EDL structure and electrode/electrolyte interface and detailed reviews can be found in more specialized papers.[277,283]

Interestingly, a new mesoscopic model called lattice model has been recently used to predict the structural, dynamical and capacitive properties of electrochemical double layer capacitors.[300] A key advantage is that it is approximately 10 000 times faster than common molecular simulations. The model combines input from molecular and experimental results and has been used to study the effects of solvation and pore size on the quantity of adsorbed ions and capacitive properties in neat and solvated ionic liquid electrolytes. This approach has predicted the quantity of adsorbed ions, capacitances and diffusion coefficients in an efficient manner. Such type of model should rapidly develop in the near future.

Finally, an alternative way to predict the capacitance of carbon-based electrodes *via* artificial neural network and machine learning methods was proposed very recently.[306,307] By using the published data and adjusting several variables (such as SSA, PSD, voltage window, *etc.*), the machine learning approach can provide an acceptable prediction that is likely to benefit researchers in the selection of carbon materials for EDLC systems.

In summary, in academic research, experiments and simulations complement each other. Various advanced *in situ* techniques for experimental use and simulation methods at different time scales have been reviewed in this section. Owing to the advanced *in situ* techniques and simulations, the exploration of the insights into charge storage in porous carbon materials has stepped up over the years. We believe that the development of the present or new techniques will push further our basic understanding of ion dynamics and adsorption in porous carbon electrodes as well as the electrolyte structure in the porous networks. These results will be the key to boost the performance of the EDL cells or even create a new generation of supercapacitors with higher energy and power density.

4. Advanced electrolytes

The electrolyte is one of the most critical factors that determine the performance of EDLCs. Eqn (3) and (4) indicate the two main properties of the electrolytes used for EDLCs: (1) electrochemical stability, defining the voltage window, which is essential for energy density; (2) ionic conductivity related to the ESR, which limits the power performance. Electrolytes for supercapacitors can be classified into three main categories, depending on their nature: aqueous- and organic-based electrolytes and ionic liquids. For aqueous electrolytes, safety and low cost are key advantages from the industrial point of view. However, the operating voltage window for such electrolytes is limited by water electrolysis (1–1.2 V).[308] As a result, the energy density of aqueous-based EDLCs is still one magnitude smaller compared to devices operating in non-aqueous electrolytes.[309] To tackle the restriction of the limited voltage window of aqueous electrolytes, several approaches have been developed over the years. By combining a pseudocapacitive material (transition metal oxides or conducting polymers) as a positive electrode and carbon-based materials as a negative electrode, the potential of hydrogen evolution shifts which results in a wider potential window. Such asymmetric or hybrid configurations can enlarge the full cell voltage window up to 1.6–2 V.[310–313] For conventional carbon-based configuration, with optimized electrode mass balance operating in neutral aqueous electrolytes such as Na_2SO_4 or Li_2SO_4, the voltage window can be improved as well.[314–316]

In 2015, Suo *et al.* introduced the concept of ''water-in-salt'' electrolytes (WIS) for lithium-ion batteries where cell voltage beyond 2 V could be reached owing to the limited amount of free water molecules.[317] As a result, the stability of water molecules toward oxidation is higher compared to conventional salt-in-water electrolytes. Using 21 M LiTFSI electrolytes and activated carbon as electrodes, the operating voltage window broadens to 2.4 V.[318] Although the existing LiTFSI shows decent performance, the cost, high viscosity and limiting operating temperature of this kind of electrolyte still need to be solved. Some alternative salts to LiTFSI have been reported in recent years, such as NaTFSI or $NaClO_4$.[319,320] In addition, an idea of introducing a co-solvent is shown to be effective for improving the power performance of such electrolytes.[321] The charging mechanism at the interface was demonstrated by MD simulation.[322] The behavior of ions depending on the change of potential acted like ionic liquid, instead of solvated aqueous or organic electrolytes. The differences in the charging mechanisms are mentioned in the previous section. Although the approach sounds interesting, the WIS concept did not result in a major breakthrough in the energy storage field. Also, for supercapacitors, the porous structure of the electrode makes

the ion exchange and transfer at the electrolyte/electrode interface even more complex compared to conventional battery materials.

Generally speaking, organic-based electrolytes have a wider voltage window compared with aqueous electrolytes, which results in a great improvement of energy density. Most of the supercapacitors available on the market are using organic electrolytes, and their energy density can reach up to 10 W h kg^{-1}.[323] However, the drawbacks of these electrolytes are the flammable property, high requirement for purification and lower conductivity compared to aqueous electrolytes. For carbon-based supercapacitors, the most frequent formulation for industrial use is $TEABF_4$ in PC or ACN solvent.[324,325] Several works have focused on the degradation of organic electrolytes and the aging of carbon materials in such a system, for improving safety.[324,326–330] Although the reactions are complex, there is useful knowledge today about the degradation mechanisms and their impact on supercapacitor performance. On the other hand, to enhance the performance of supercapacitors in such an electrolyte system, the ionic dynamics and ion confinement in micropores have also been investigated,[128,150,190] including the effect of solvent and desolvation of ions while entering micropores.[127,286,331–334]

Recently, a computational method was proposed to boost the process to discover new organic solvents in an efficient and systematic way.[335,336] By screening the desirable properties of the solvent, such as voltage window, viscosity, and ion solubility, several combinations of new solvents (cyano ester-based and nitrile-based) and salts were proposed as alternative electrolytes.[336–339] Fig. 15 first shows the screening procedures, then an example of discovering new solvents.

In combination with the conventional $TEABF_4$ salt, an operating cell voltage up to 3.2 V was achieved which confirms the potential of the method and justifies further use of machine learning and artificial intelligence, owing to the large variety of combinations possible.[131] The same computation method was also applied for investigating new ionic liquids. In addition to organic electrolytes, ionic liquids are also a compatible choice that can exhibit a high energy density. Ionic liquids are solvent-free electrolytes which only contain cations and anions. The general properties of ionic liquids are good chemical stability, wide electrochemical voltage window, but low to moderate ionic conductivity and limited low temperature operation.[340–342] In the past decade, a lot of works have shown ionic liquids are safe and perform relatively well in a large range of temperature (80 to −50 °C).[76,91,343–345] Although the energy density has met the requirement for industrial use, because of their high viscosity (relatively low ionic conductivity compared to other electrolytes), the improvement of power density for such systems is a challenge.[346] A large amount of experimental and simulation works over the years have shown that with a mixture of different solvents and ionic liquids or ionic liquids with different viscosities, the general properties (viscosity, ionic conductivity, diffusion coefficient and so on) are improved; also the interaction of ionic liquids at an electrified surface can be modified.[347–356] As a kind of solvent in the salt approach, the wettability of ionic liquids with a small addition of solvent has been improved for porous materials.[357] Although this work did not yet result in a major breakthrough in terms of performance, it led to important advances in the scientific understanding of the ionic/carbon interaction in porous carbon electrodes. Recently, DFT calculation has been applied to predict the electrochemical potential windows for ionic liquids to accelerate the process for experimental selection.[358] Theoretical and experimental works have shown that unlike solvated electrolytes, the EDL structure of ionic liquids does not align with the classic EDL models (for details of the model see Section 2.1).[36,41,359] In ionic liquids, the existence of ion pairs and compact packing of ions result in a short- to long-range of electrostatic force based on the applied voltage.[38,44,245,360–363] Apart from the development of the classic two dimensional EDL models for ionic liquids, the ion

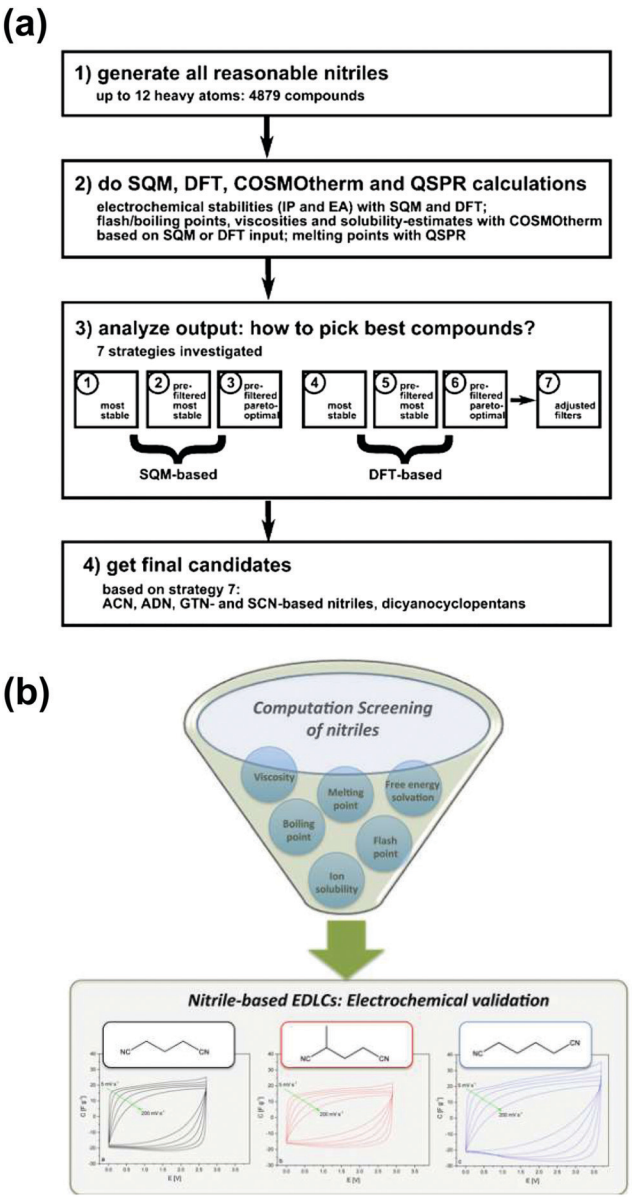

Fig. 15 (a) The screening strategy based on computational methods. (b) An illustration abstract for selecting a new solvent for supercapacitor applications. The figure is reproduced from ref. 336 with permission from 2008 American Chemical Society.

confinement and dynamics in nanoporous materials are also the main topic. Some experimental works, including basic electrochemical analysis and *in situ* techniques, such as *in situ* EQCM, *in situ* NMR, *in situ* SAXS, and simulation method at the molecular level, delivered some insights such as mentioned earlier.[203,228,284,294,296,332,364–366] The information of how ions are packed inside nanopores, the selectivity of ions, and the charging mechanisms in such an electrolyte system will hopefully help to develop porous materials with the optimized structure to boost the performance of EDLCs.

In addition, to store the charge at the surface of porous materials, a new strategy has been recently proposed to enhance energy density by involving redox species in the electrolyte, which is called the redox electrolyte. Electrons can be injected/removed into/from redox species dissolved in the electrolyte, then adding an additional faradaic contribution to the double layer capacitance and transforming the electrolyte into an active material.[131,367–371] The advantage of reactions occurring in an electrolyte medium is that the ion transport in solid materials is slower than that in liquids. In this case, the power performance will not be sacrificed while improving energy density. This concept was first applied for supercapacitors in aqueous-based electrolytes, including halide ions, quinones, and $VOSO_4$.[372–378] During these two years, some new strategies are proposed, for example, applying redox additive electrolytes for hybrid supercapacitors or choosing suitable supporting electrolytes.[379] However, because of their high diffusivity of ions in aqueous electrolytes, the self-discharge remains a great issue.[380]

A new concept proposed by Rochefort's[381] and Fontaine's group[382] uses a biredox ionic liquid as salt in an electrolyte to achieve bulk-like redox density with liquid-like fast kinetics. The cation and anion of these biredox ionic liquids bear moieties that undergo very fast reversible redox reactions. Mourad *et al.* synthesized an ionic liquid with two different redox active species anthraquinone (AQ) and 2,2,6,6-tetramethylpiperidinyl-1-oxyl (TEMPO) attached on perfluorosulfonate anions (PFS^-) and methyl imidazolium cations (MIm^+), respectively.[382] The structure and charge storage mechanisms are shown in Fig. 16. The capacitance in this biredox electrolyte was twice that of the biredox-free BMImTFSI ionic liquid electrolyte and remained stable for 2000 cycles. The power performance was similar in both electrolytes. Importantly, the leakage current measured for the biredox IL was two to three times lower than that for the biredox-free IL, which means a decreased self-discharge. This was explained by specific interactions inside the porous carbon network.

The biredox concept is certainly an interesting approach.[383–386] These redox-active electrolytes offer opportunities for improving the energy density of EDLC devices and there is little doubt that more work will appear in the next years to exploit this concept.

Differently from conventional supercapacitors, micro-supercapacitors and flexible supercapacitors are currently fast developing to meet the requirements for diverse applications such as the internet of things (IoT). In this field, work has been dedicated to the development of solid-state electrolytes (SSEs)

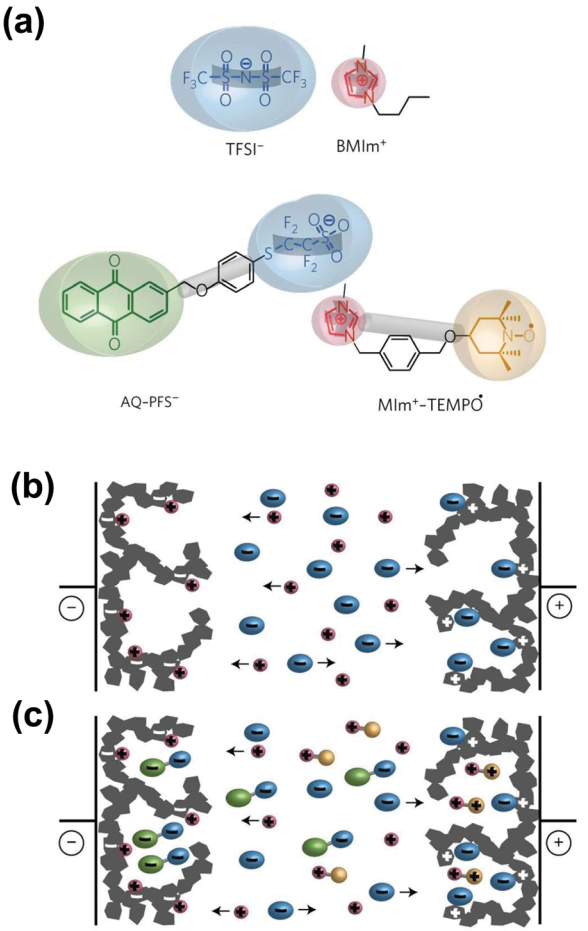

Fig. 16 (a) Structure of the biredox ionic liquid mentioned above. (b) and (c) Illustrations of the charge storage for pure IL and biredox IL, respectively. Reproduced from ref. 382 with permission from Springer Nature (copyright 2017).

to prevent the leakage of liquid electrolytes.[387–392] Like in batteries, a SSE acts as an electrolyte and a separator in the device. As a result, it requires high mechanical strength and wide operating temperature. Differently from batteries, a SSE cannot be prepared from ceramic (oxides or sulfur) because of the high surface area of the porous carbons used. Alternatively, SSEs for supercapacitors contain liquid electrolytes embedded inside the polymer or non-organic matrix (such as silica). For instance, a zwitterionic-type of polymer matrix has been proposed as an aqueous-based gel electrolyte, with high water content and fast ion migration, which result in decent volumetric capacitance for graphene-based supercapacitors (300 F cm^{-3} at 0.8 A cm^{-3}).[393] Ionogels, which combine an ionic liquid electrolyte entrapped in an inorganic silica matrix, have been successfully developed for this application.[391,394,395] A key feature of these SSEs is the possibility of the IL to diffuse by capillarity, and by hydrophobic interaction, to impregnate the nanoporous network of the carbon electrode.[396] As a result, the capacitance is close to that of IL electrolytes.

Another family of SSEs for supercapacitors deal with polymers. Polymers have been used as proton conducting electrolytes as well

as gel polymer electrolytes (GPEs). There has been a huge amount of work on these systems so that we will not go into the details and will refer to review papers where all key information can be found.[28,390,397] Basically, polymers offer interesting properties for designing proton conducting electrolytes and aqueous-based GPEs, but still fall short to provide a voltage window beyond 1.5 V with decent stability. As a result, the energy density is still low, but the absence of electrolyte leakage is an added value for micro-devices.

Last, a recent study proposed the design of an ''all-in-gel'' supercapacitor.[398] The idea is to produce gel-like electrodes by mixing carbon nanotubes, an ionic liquid and some additives so that the contact issue at the electrode/electrolyte interface can be solved. The mechanical strength of this type of electrolyte is high and it is easy to shape it in different forms so that this approach could be interesting to follow for solid state micro-devices.

5. Summary and perspectives

Electrochemical capacitors are currently key energy storage devices for high-power applications. The recent decade has witnessed the booming of novel electrode materials, for instance metal oxides or metal carbides/nitrides, and electrolyte concepts; yet porous carbon-based electrodes are still the leading materials in real applications. This review is dedicated to covering the recent progress in nanoporous carbon electrodes for electrochemical capacitive energy storage.

It has started up with detailing the fundamental basics of EDL formation from the view point of ion–electrode correlations at planar, 2D electrodes. However, this model falls short to describe correctly the charge mechanism in nanoporous carbons, for which a good picture of the porous structure is required. The refinement of gas sorption techniques turned out to be crucial to push further our basic understanding of the charge storage mechanism in porous carbon-based EDLCs. Ar and CO_2 gas probes are the ones to be recommended instead of N_2 for measuring the SSA and PSD of nanoporous carbons. Although high SSA is always beneficial for increasing capacitance, no direct trend has been established so far. Instead, it has been found that small pore size matters the most and leads to a capacitance increase for nanoporous carbons with pore size below 1 nm, due to the ion desolvation. Some authors, using simple analytical models, have succeeded in showing that, by means of ideal endo- and exo-hedral carbon, the local curvature of the carbon surface in nanopores can explain the capacitance increase in carbon nanopores.

Since then, new advanced *in situ* experimental setups and computational tools have been proposed to gain insights into the charge storage mechanisms. *In situ* EQCM is reviewed as a powerful tool for tracking ion and solvent molecule transfer across the porous carbon material/electrolyte interface, during the polarization of the electrode. This technique has been nicely complemented with *in situ* NMR, to obtain information on the ion environments in nanopores. *In situ* SAS techniques and other techniques like *in situ* XRD, *in situ* infrared spectroelectrochemistry, *etc.*, have turned out to be useful for investigating ion adsorption in nanoporous carbon. When coupled with advanced characterization techniques, modeling and simulation demonstrate great potential in resolving the underlying theory and predicting optimized carbon structures. For instance, MD simulation and DFT approach are capable of illustrating the origin of the capacitance increase in nanopores in terms of positive curvature of carbon nanopores.

Even though lots of efforts have been made on the carbon side, there has been still recent progress in developing advanced electrolytes. The ''water-in-salt'' electrolytes have made possible the obtention of aqueous-based electrolytes exhibiting an operating voltage as high as 2.4 V. In the meantime, an appealing class of ionic liquids has been given birth: the biredox ionic liquids with great potential in bringing redox reaction on the nanoporous carbon surface, which may highly enhance the capacitance. There is still room for improvement of this aspect, and computational approaches have been recently proposed to boost the process to discover new organic solvents in an efficient and systematic way.

Despite the aforementioned impressive progress, carbon-based supercapacitors are still limited by relatively low energy density. The design of nanoporous carbon with finely tuned, controlled pore size below 1 nm is still highly challenging. Therefore, new strategies for producing high-quality nanoporous carbon with controlled pore size in a more cost-effective and efficient way are needed. Alternatively, carbon with ionophobic pores was predicted to achieve high energy density without compensation of power performance, and this could be an effective way to improve the performance; however, the preparation of these ionophobic carbons remains highly challenging. Progress can also be made by optimizing the electrode composition, which goes beyond the limitation of carbon materials to enhance the performance of EDLCs. For instance, while electrochemically inactive binders and conducting additives are used for electrode preparation, recent works suggested that these components can be replaced with graphene or MXene materials, which can contribute to EDL capacitance.[399,400]

The fundamental understanding of the charge storage mechanism in nanopores has achieved considerable progress; however, the full picture remains unclear, especially when a complex pore structure is considered, or a redox reaction is involved. More advanced techniques are essential to gain more information about the electrolyte/electrode interface interaction. As many techniques are claimed as *in situ* or *operando* techniques, attention should be paid to the possible change of the electrochemical process that may be induced by the measurements themselves, and therefore, non-destructive techniques are recommended. The combination with simulation or modeling is another effective tool for digging extra information, such as ion distribution and population.

Developing new electrolytes is one of the most effective routes to push EDLCs to higher energy density. Aqueous electrolytes with a large operating potential range as well as redox electrolytes are promising. More related electrolytes with low cost, high stability, and good safety should be designed

with the assistance of computational methods. Considering the booming advancement of machine learning and artificial intelligence, there is no doubt that the computational methods will play a very important role in this field in the upcoming years.

Conflicts of interest

There are no conflicts to declare.

Acknowledgements

HS was supported by a grant from the China Scholarship Council (no. 201608370077). PS, PLT, YCW and HS thank the Agence Nationale de la Recherche (Labex STORE-EX) for financial support. ZL is supported by the Fundamental Research Funds for the Central Universities (YJ201886) and the National Natural Science Foundation of China (Grant No. 501902215).

References

1 S. Chu and A. Majumdar, *Nature*, 2012, **488**, 294.
2 B. Dunn, H. Kamath and J.-M. Tarascon, *Science*, 2011, **334**, 928–935.
3 V. Augustyn, P. Simon and B. Dunn, *Energy Environ. Sci.*, 2014, **7**, 1597–1614.
4 C. Choi, D. S. Ashby, D. M. Butts, R. H. DeBlock, Q. Wei, J. Lau and B. Dunn, *Nat. Rev. Mater.*, 2019, 1–15.
5 P. Simon and Y. Gogotsi, *Nat. Mater.*, 2008, **7**, 845–854.
6 M. Salanne, B. Rotenberg, K. Naoi, K. Kaneko, P.-L. Taberna, C. P. Grey, B. Dunn and P. Simon, *Nat. Energy*, 2016, **1**, 16070.
7 J. R. Miller and P. Simon, *Science*, 2008, **321**, 651–652.
8 H. v. Helmholtz, *Ann. Phys.*, 1853, **165**, 353–377.
9 G. P. Wang, L. Zhang and J. J. Zhang, *Chem. Soc. Rev.*, 2012, **41**, 797–828.
10 Y. Zhai, Y. Dou, D. Zhao, P. F. Fulvio, R. T. Mayes and S. Dai, *Adv. Mater.*, 2011, **23**, 4828–4850.
11 L. L. Zhang and X. Zhao, *Chem. Soc. Rev.*, 2009, **38**, 2520–2531.
12 B. E. Conway, *Electrochemical supercapacitors: scientific fundamentals and technological applications*, Kluwer Academic/Plenum, New York, 1999.
13 J. Schindall, *IEEE Spectrum*, 2007, **44**, 42–46.
14 J. Chmiola, G. Yushin, Y. Gogotsi, C. Portet, P. Simon and P.-L. Taberna, *Science*, 2006, **313**, 1760–1763.
15 E. Raymundo-Pinero, K. Kierzek, J. Machnikowski and F. Béguin, *Carbon*, 2006, **44**, 2498–2507.
16 H. Shi, *Electrochim. Acta*, 1996, **41**, 1633–1639.
17 G. Salitra, A. Soffer, L. Eliad, Y. Cohen and D. Aurbach, *J. Electrochem. Soc.*, 2000, **147**, 2486–2493.
18 Y. Gogotsi and P. Simon, *Science*, 2011, **334**, 917–918.
19 S. Zhang and N. Pan, *Adv. Energy Mater.*, 2015, **5**, 1401401.
20 A. Noori, M. F. El-Kady, M. S. Rahmanifar, R. B. Kaner and M. F. Mousavi, *Chem. Soc. Rev.*, 2019, **48**, 1272–1341.
21 A. Balducci, D. Belanger, T. Brousse, J. Long and W. Sugimoto, *J. Electrochem. Soc.*, 2017, **164**, A1487–A1488.
22 T. S. Mathis, N. Kurra, X. Wang, D. Pinto, P. Simon and Y. Gogotsi, *Adv. Energy Mater.*, 2019, 1902007.
23 K. Naoi, S. Ishimoto, J.-I. Miyamoto and W. Naoi, *Energy Environ. Sci.*, 2012, **5**, 9363–9373.
24 M. Armand, F. Endres, D. R. MacFarlane, H. Ohno and B. Scrosati, *Nat. Mater.*, 2009, **8**, 621–629.
25 M. V. Fedorov and A. A. Kornyshev, *Chem. Rev.*, 2014, **114**, 2978–3036.
26 J. Le Bideau, L. Viau and A. Vioux, *Chem. Soc. Rev.*, 2011, **40**, 907–925.
27 D. R. MacFarlane, N. Tachikawa, M. Forsyth, J. M. Pringle, P. C. Howlett, G. D. Elliott, J. H. Davis, M. Watanabe, P. Simon and C. A. Angell, *Energy Environ. Sci.*, 2014, **7**, 232–250.
28 C. Zhong, Y. Deng, W. Hu, J. Qiao, L. Zhang and J. Zhang, *Chem. Soc. Rev.*, 2015, **44**, 7484–7539.
29 M. Lu, *Supercapacitors: materials, systems, and applications*, John Wiley & Sons, 2013.
30 M.-M. Huang, Y. Jiang, P. Sasisanker, G. W. Driver and H. Weingärtner, *J. Chem. Eng. Data*, 2011, **56**, 1494–1499.
31 M. Gouy, *J. Phys. Theor. Appl.*, 1910, **9**, 457–468.
32 D. L. Chapman, *London, Edinburgh Dublin Philos. Mag. J. Sci.*, 1913, **25**, 475–481.
33 D. C. Grahame, *Chem. Rev.*, 1947, **41**, 441–501.
34 A. J. Bard, L. R. Faulkner, J. Leddy and C. G. Zoski, *Electrochemical methods: fundamentals and applications*, Wiley, New York, 1980.
35 O. Stern, *Z. Elektrochem.*, 1924, **30**, 1014–1020.
36 A. A. Kornyshev, *J. Phys. Chem. B*, 2007, **111**, 5545–5557.
37 W. Fawcett, *Isr. J. Chem.*, 1979, **18**, 3–16.
38 M. Z. Bazant, B. D. Storey and A. A. Kornyshev, *Phys. Rev. Lett.*, 2011, **106**, 046102.
39 M. M. Islam, M. T. Alam and T. Ohsaka, *J. Phys. Chem. C*, 2008, **112**, 16568–16574.
40 V. Lockett, R. Sedev, J. Ralston, M. Horne and T. Rodopoulos, *J. Phys. Chem. C*, 2008, **112**, 7486–7495.
41 M. V. Fedorov and A. A. Kornyshev, *J. Phys. Chem. B*, 2008, **112**, 11868–11872.
42 M. Trulsson, J. Algotsson, J. Forsman and C. E. Woodward, *J. Phys. Chem. Lett.*, 2010, **1**, 1191–1195.
43 C. Merlet, B. Rotenberg, P. A. Madden and M. Salanne, *Phys. Chem. Chem. Phys.*, 2013, **15**, 15781–15792.
44 M. Mezger, H. Schröder, H. Reichert, S. Schramm, J. S. Okasinski, S. Schöder, V. Honkimäki, M. Deutsch, B. M. Ocko and J. Ralston, *Science*, 2008, **322**, 424–428.
45 X. Mao, P. Brown, C. Červinka, G. Hazell, H. Li, Y. Ren, D. Chen, R. Atkin, J. Eastoe and I. Grillo, *Nat. Mater.*, 2019, 1–8.
46 C. Merlet, M. Salanne, B. Rotenberg and P. A. Madden, *J. Phys. Chem. C*, 2011, **115**, 16613–16618.
47 J. Vatamanu, O. Borodin and G. D. Smith, *J. Am. Chem. Soc.*, 2010, **132**, 14825–14833.
48 S. Baldelli, *J. Phys. Chem. Lett.*, 2012, **4**, 244–252.
49 S. Baldelli, *Acc. Chem. Res.*, 2008, **41**, 421–431.

50 M. A. Gebbie, M. Valtiner, X. Banquy, E. T. Fox, W. A. Henderson and J. N. Israelachvili, *Proc. Natl. Acad. Sci. U. S. A.*, 2013, **110**, 9674–9679.
51 K. Kirchner, T. Kirchner, V. Ivaništšev and M. V. Fedorov, *Electrochim. Acta*, 2013, **110**, 762–771.
52 K. S. Sing, *Pure Appl. Chem.*, 1985, **57**, 603–619.
53 J. Gamby, P. L. Taberna, P. Simon, J. F. Fauvarque and M. Chesneau, *J. Power Sources*, 2001, **101**, 109–116.
54 L. Wei, M. Sevilla, A. B. Fuertes, R. Mokaya and G. Yushin, *Adv. Energy Mater.*, 2011, **1**, 356–361.
55 L. Wei, M. Sevilla, A. B. Fuertes, R. Mokaya and G. Yushin, *Adv. Funct. Mater.*, 2012, **22**, 827–834.
56 J. Yan, Q. Wang, T. Wei and Z. Fan, *Adv. Energy Mater.*, 2014, **4**, 1300816.
57 C. Peng, X.-B. Yan, R.-T. Wang, J.-W. Lang, Y.-J. Ou and Q.-J. Xue, *Electrochim. Acta*, 2013, **87**, 401–408.
58 Y. Gogotsi, A. Nikitin, H. Ye, W. Zhou, J. E. Fischer, B. Yi, H. C. Foley and M. W. Barsoum, *Nat. Mater.*, 2003, **2**, 591.
59 P. Simon and Y. Gogotsi, *Acc. Chem. Res.*, 2012, **46**, 1094–1103.
60 C. Largeot, C. Portet, J. Chmiola, P.-L. Taberna, Y. Gogotsi and P. Simon, *J. Am. Chem. Soc.*, 2008, **130**, 2730–2731.
61 C. Portet, G. Yushin and Y. Gogotsi, *J. Electrochem. Soc.*, 2008, **155**, A531–A536.
62 Y. Korenblit, M. Rose, E. Kockrick, L. Borchardt, A. Kvit, S. Kaskel and G. Yushin, *ACS Nano*, 2010, **4**, 1337–1344.
63 H. J. Liu, J. Wang, C. X. Wang and Y. Y. Xia, *Adv. Energy Mater.*, 2011, **1**, 1101–1108.
64 M. Rose, Y. Korenblit, E. Kockrick, L. Borchardt, M. Oschatz, S. Kaskel and G. Yushin, *Small*, 2011, **7**, 1108–1117.
65 J. Chmiola, G. Yushin, R. Dash and Y. Gogotsi, *J. Power Sources*, 2006, **158**, 765–772.
66 H. Nishihara and T. Kyotani, *Adv. Mater.*, 2012, **24**, 4473–4498.
67 H. Nishihara, H. Itoi, T. Kogure, P.-X. Hou, H. Touhara, F. Okino and T. Kyotani, *Chem. – Eur. J.*, 2009, **15**, 5355–5363.
68 H. Itoi, H. Nishihara, T. Kogure and T. Kyotani, *J. Am. Chem. Soc.*, 2011, **133**, 1165–1167.
69 V. L. Kuznetsov, A. L. Chuvilin, Y. V. Butenko, I. Y. Mal'kov and V. M. Titov, *Chem. Phys. Lett.*, 1994, **222**, 343–348.
70 M. Zeiger, N. Jäckel, V. N. Mochalin and V. Presser, *J. Mater. Chem. A*, 2016, **4**, 3172–3196.
71 J. K. McDonough and Y. Gogotsi, *Electrochem. Soc. Interface*, 2013, **22**, 61–66.
72 M. Zeiger, N. Jäckel, M. Aslan, D. Weingarth and V. Presser, *Carbon*, 2015, **84**, 584–598.
73 C. Portet, G. Yushin and Y. Gogotsi, *Carbon*, 2007, **45**, 2511–2518.
74 E. Bushueva, P. Galkin, A. Okotrub, L. Bulusheva, N. Gavrilov, V. Kuznetsov and S. Moiseekov, *Phys. Status Solidi B*, 2008, **245**, 2296–2299.
75 D. Pech, M. Brunet, H. Durou, P. Huang, V. Mochalin, Y. Gogotsi, P.-L. Taberna and P. Simon, *Nat. Nanotechnol.*, 2010, **5**, 651.
76 R. Lin, P.-L. Taberna, S. Fantini, V. Presser, C. R. Pérez, F. Malbosc, N. L. Rupesinghe, K. B. Teo, Y. Gogotsi and P. Simon, *J. Phys. Chem. Lett.*, 2011, **2**, 2396–2401.
77 K. Jost, C. R. Perez, J. K. McDonough, V. Presser, M. Heon, G. Dion and Y. Gogotsi, *Energy Environ. Sci.*, 2011, **4**, 5060–5067.
78 N. Jäckel, D. Weingarth, M. Zeiger, M. Aslan, I. Grobelsek and V. Presser, *J. Power Sources*, 2014, **272**, 1122–1133.
79 R. H. Baughman, A. A. Zakhidov and W. A. De Heer, *Science*, 2002, **297**, 787–792.
80 Z. Yang, J. Tian, Z. Yin, C. Cui, W. Qian and F. Wei, *Carbon*, 2019, **141**, 467–480.
81 A. Peigney, C. Laurent, E. Flahaut, R. Bacsa and A. Rousset, *Carbon*, 2001, **39**, 507–514.
82 Y. Shim and H. J. Kim, *ACS Nano*, 2010, **4**, 2345–2355.
83 L. Yang, B. H. Fishbine, A. Migliori and L. R. Pratt, *J. Am. Chem. Soc.*, 2009, **131**, 12373–12376.
84 G. Feng, R. Qiao, J. Huang, S. Dai, B. G. Sumpter and V. Meunier, *Phys. Chem. Chem. Phys.*, 2011, **13**, 1152–1161.
85 M. F. El-Kady, Y. Shao and R. B. Kaner, *Nat. Rev. Mater.*, 2016, **1**, 16033.
86 F. Bonaccorso, L. Colombo, G. Yu, M. Stoller, V. Tozzini, A. C. Ferrari, R. S. Ruoff and V. Pellegrini, *Science*, 2015, **347**, 1246501.
87 J. Xia, F. Chen, J. Li and N. Tao, *Nat. Nanotechnol.*, 2009, **4**, 505.
88 H. Banda, S. Périé, B. Daffos, P.-L. Taberna, L. Dubois, O. Crosnier, P. Simon, D. Lee, G. De Paëpe and F. Duclairoir, *ACS Nano*, 2019, **13**, 1443–1453.
89 X. Yang, C. Cheng, Y. Wang, L. Qiu and D. Li, *Science*, 2013, **341**, 534–537.
90 Y. Zhu, S. Murali, M. D. Stoller, K. Ganesh, W. Cai, P. J. Ferreira, A. Pirkle, R. M. Wallace, K. A. Cychosz and M. Thommes, *Science*, 2011, **332**, 1537–1541.
91 W. Y. Tsai, R. Y. Lin, S. Murali, L. L. Zhang, J. K. McDonough, R. S. Ruoff, P. L. Taberna, Y. Gogotsi and P. Simon, *Nano Energy*, 2013, **2**, 403–411.
92 Y. Xu, Z. Lin, X. Zhong, X. Huang, N. O. Weiss, Y. Huang and X. Duan, *Nat. Commun.*, 2014, **5**, 4554.
93 L. A. Jurado and R. M. Espinosa-Marzal, *Sci. Rep.*, 2017, **7**, 1–12.
94 M. Zeiger, N. Jäckel, D. Weingarth and V. Presser, *Carbon*, 2015, **94**, 507–517.
95 J. Xu, N. Yuan, J. M. Razal, Y. Zheng, X. Zhou, J. Ding, K. Cho, S. Ge, R. Zhang, Y. Gogotsi and R. H. Baughman, *Energy Storage Mater.*, 2019, **22**, 323–329.
96 H.-J. Liu, W.-J. Cui, L.-H. Jin, C.-X. Wang and Y.-Y. Xia, *J. Mater. Chem.*, 2009, **19**, 3661–3667.
97 H.-J. Liu, X.-M. Wang, W.-J. Cui, Y.-Q. Dou, D.-Y. Zhao and Y.-Y. Xia, *J. Mater. Chem.*, 2010, **20**, 4223–4230.
98 W. Chaikittisilp, M. Hu, H. Wang, H.-S. Huang, T. Fujita, K. C.-W. Wu, L.-C. Chen, Y. Yamauchi and K. Ariga, *Chem. Commun.*, 2012, **48**, 7259–7261.
99 O. Kimizuka, O. Tanaike, J. Yamashita, T. Hiraoka, D. N. Futaba, K. Hata, K. Machida, S. Suematsu, K. Tamamitsu and S. Saeki, *Carbon*, 2008, **46**, 1999–2001.
100 A. K. Geim and K. S. Novoselov, *Nat. Mater.*, 2007, **6**, 183–191.
101 L. L. Zhang, X. Zhao, H. Ji, M. D. Stoller, L. Lai, S. Murali, S. Mcdonnell, B. Cleveger, R. M. Wallace and R. S. Ruoff, *Energy Environ. Sci.*, 2012, **5**, 9618–9625.

102 J. Jagiello and J. P. Olivier, *Carbon*, 2013, **55**, 70–80.
103 A. C. Forse, C. Merlet, P. K. Allan, E. K. Humphreys, J. M. Griffin, M. Aslan, M. Zeiger, V. Presser, Y. Gogotsi and C. P. Grey, *Chem. Mater.*, 2015, **27**, 6848–6857.
104 K. A. Cychosz, R. Guillet-Nicolas, J. Garcia-Martinez and M. Thommes, *Chem. Soc. Rev.*, 2017, **46**, 389–414.
105 M. Thommes and K. A. Cychosz, *Adsorption*, 2014, **20**, 233–250.
106 S. Lowell, J. E. Shields, M. A. Thomas and M. Thommes, *Characterization of porous solids and powders: surface area, pore size and density*, Springer Science & Business Media, 2012.
107 J. Rouquerol, F. Rouquerol, P. Llewellyn, G. Maurin and K. S. Sing, *Adsorption by powders and porous solids: principles, methodology and applications*, Academic Press, 2013.
108 D. Cazorla-Amorós, J. Alcaniz-Monge and A. Linares-Solano, *Langmuir*, 1996, **12**, 2820–2824.
109 J. Rouquerol, P. Llewellyn and F. Rouquerol, *Stud. Surf. Sci. Catal.*, 2007, **160**, 49–56.
110 M. Thommes, K. Kaneko, A. V. Neimark, J. P. Olivier, F. Rodriguez-Reinoso, J. Rouquerol and K. S. Sing, *Pure Appl. Chem.*, 2015, **87**, 1051–1069.
111 J. Landers, G. Y. Gor and A. V. Neimark, *Colloids Surf., A*, 2013, **437**, 3–32.
112 C. Lastoskie, K. E. Gubbins and N. Quirke, *J. Phys. Chem.*, 1993, **97**, 4786–4796.
113 P. A. Monson, *Microporous Mesoporous Mater.*, 2012, **160**, 47–66.
114 A. V. Neimark, Y. Lin, P. I. Ravikovitch and M. Thommes, *Carbon*, 2009, **47**, 1617–1628.
115 G. Laudisio, R. K. Dash, J. P. Singer, G. Yushin, Y. Gogotsi and J. E. Fischer, *Langmuir*, 2006, **22**, 8945–8950.
116 L. He, S. M. Chathoth, Y. B. Melnichenko, V. Presser, J. McDonough and Y. Gogotsi, *Microporous Mesoporous Mater.*, 2012, **149**, 46–54.
117 M. Endo, T. Maeda, T. Takeda, Y. J. Kim, K. Koshiba, H. Hara and M. S. Dresselhaus, *J. Electrochem. Soc.*, 2001, **148**, A910.
118 O. Barbieri, M. Hahn, A. Herzog and R. Kötz, *Carbon*, 2005, **43**, 1303–1310.
119 H. X. Ji, X. Zhao, Z. H. Qiao, J. Jung, Y. W. Zhu, Y. L. Lu, L. L. Zhang, A. H. MacDonald and R. S. Ruoff, *Nat. Commun.*, 2014, **5**, 3317.
120 C. Lin, J. A. Ritter and B. N. Popov, *J. Electrochem. Soc.*, 1999, **146**, 3639–3643.
121 D. Lozano-Castello, D. Cazorla-Amorós, A. Linares-Solano, S. Shiraishi, H. Kurihara and A. Oya, *Carbon*, 2003, **41**, 1765–1775.
122 L. Eliad, G. Salitra, A. Soffer and D. Aurbach, *J. Phys. Chem. B*, 2001, **105**, 6880–6887.
123 L. Eliad, G. Salitra, A. Soffer and D. Aurbach, *Langmuir*, 2005, **21**, 3198–3202.
124 B. Kastening and S. Spinzig, *J. Electroanal. Chem. Interfacial Electrochem.*, 1986, **214**, 295–302.
125 C. Vix-Guterl, E. Frackowiak, K. Jurewicz, M. Friebe, J. Parmentier and F. Béguin, *Carbon*, 2005, **43**, 1293–1302.
126 T. Ohkubo, T. Konishi, Y. Hattori, H. Kanoh, T. Fujikawa and K. Kaneko, *J. Am. Chem. Soc.*, 2002, **124**, 11860–11861.
127 J. Chmiola, C. Largeot, P. L. Taberna, P. Simon and Y. Gogotsi, *Angew. Chem.*, 2008, **120**, 3440–3443.
128 C. Prehal, C. Koczwara, N. Jäckel, A. Schreiber, M. Burian, H. Amenitsch, M. A. Hartmann, V. Presser and O. Paris, *Nat. Energy*, 2017, **2**, 16215.
129 T. A. Centeno, O. Sereda and F. Stoeckli, *Phys. Chem. Chem. Phys.*, 2011, **13**, 12403–12406.
130 A. García-Gómez, G. Moreno-Fernández, B. Lobato and T. A. Centeno, *Phys. Chem. Chem. Phys.*, 2015, **17**, 15687–15690.
131 F. Béguin, V. Presser, A. Balducci and E. Frackowiak, *Adv. Mater.*, 2014, **26**, 2219–2251.
132 S. Kondrat, C. Perez, V. Presser, Y. Gogotsi and A. Kornyshev, *Energy Environ. Sci.*, 2012, **5**, 6474–6479.
133 D. T. Galhena, B. C. Bayer, S. Hofmann and G. A. Amaratunga, *ACS Nano*, 2015, **10**, 747–754.
134 J. Huang, B. G. Sumpter and V. Meunier, *Chem. – Eur. J.*, 2008, **14**, 6614–6626.
135 C. O. Ania, J. Pernak, F. Stefaniak, E. Raymundo-Piñero and F. Béguin, *Carbon*, 2009, **47**, 3158–3166.
136 B. Lobato, L. Suárez, L. Guardia and T. A. Centeno, *Carbon*, 2017, **122**, 434–445.
137 N. Jackel, P. Simon, Y. Gogotsi and V. Presser, *ACS Energy Lett.*, 2016, **1**, 1262–1265.
138 J. Huang, B. G. Sumpter and V. Meunier, *Angew. Chem., Int. Ed.*, 2008, **47**, 520–524.
139 G. Feng, R. Qiao, J. Huang, B. G. Sumpter and V. Meunier, *ACS Nano*, 2010, **4**, 2382–2390.
140 J. Huang, B. G. Sumpter, V. Meunier, G. Yushin, C. Portet and Y. Gogotsi, *J. Mater. Res.*, 2010, **25**, 1525–1531.
141 Y. Honda, T. Haramoto, M. Takeshige, H. Shiozaki, T. Kitamura, K. Yoshikawa and M. Ishikawa, *J. Electrochem. Soc.*, 2008, **155**, A930–A935.
142 G. Sauerbrey, *Z. Phys.*, 1959, **155**, 206–212.
143 R. Etchenique and E. Calvo, *Electrochem. Commun.*, 1999, **1**, 167–170.
144 C. Eickes, J. Rosenmund, S. Wasle, K. Doblhofer, K. Wang and K. Weil, *Electrochim. Acta*, 2000, **45**, 3623–3628.
145 M. Moshkovich, M. Cojocaru, H. Gottlieb and D. Aurbach, *J. Electroanal. Chem.*, 2001, **497**, 84–96.
146 H. Stadler, M. Mondon and C. Ziegler, *Anal. Bioanal. Chem.*, 2003, **375**, 53–61.
147 M. D. Levi, G. Salitra, N. Levy, D. Aurbach and J. Maier, *Nat. Mater.*, 2009, **8**, 872.
148 M. D. Levi, N. Levy, S. Sigalov, G. Salitra, D. Aurbach and J. Maier, *J. Am. Chem. Soc.*, 2010, **132**, 13220–13222.
149 M. D. Levi, S. Sigalov, D. Aurbach and L. Daikhin, *J. Phys. Chem. C*, 2013, **117**, 14876–14889.
150 W.-Y. Tsai, P.-L. Taberna and P. Simon, *J. Am. Chem. Soc.*, 2014, **136**, 8722–8728.
151 M. D. Levi, S. Sigalov, G. Salitra, R. Elazari and D. Aurbach, *J. Phys. Chem. Lett.*, 2011, **2**, 120–124.
152 Y.-C. Wu, P.-L. Taberna and P. Simon, *Electrochem. Commun.*, 2018, **93**, 119–122.

153 J. Ye, Y.-C. W, K. Xu, K. Ni, N. Shu, P.-L. Taberna, Y. Zhu and P. Simon, *J. Am. Chem. Soc.*, 2019, **141**, 16559–16563.
154 R. Yan, M. Antonietti and M. Oschatz, *Adv. Energy Mater.*, 2018, **8**, 1800026.
155 Q. Zhang, M. D. Levi, Y. Chai, X. Zhang, D. Xiao, Q. Dou, P. Ma, H. Ji and X. Yan, *Small Methods*, 2019, 1900246.
156 Z. Yang, M. C. Dixon, R. A. Erck and L. Trahey, *ACS Appl. Mater. Interfaces*, 2015, **7**, 26585–26594.
157 N. Shpigel, M. D. Levi, S. Sigalov, D. Aurbach, L. Daikhin and V. Presser, *J. Phys.: Condens. Matter*, 2016, **28**, 114001.
158 M. D. Levi, N. Shpigel, S. Sigalov, V. Dargel, L. Daikhin and D. Aurbach, *Electrochim. Acta*, 2017, **232**, 271–284.
159 M. D. Levi, M. R. Lukatskaya, S. Sigalov, M. Beidaghi, N. Shpigel, L. Daikhin, D. Aurbach, M. W. Barsoum and Y. Gogotsi, *Adv. Energy Mater.*, 2015, **5**, 1400815.
160 N. Shpigel, M. D. Levi and D. Aurbach, *Energy Storage Mater.*, 2019, **21**, 399–413.
161 A. Arnau, *Sensors*, 2008, **8**, 370–411.
162 M. C. Dixon, *J. Biomol. Tech.*, 2008, **19**, 151.
163 N. B. Eisele, F. I. Andersson, S. Frey and R. P. Richter, *Biomacromolecules*, 2012, **13**, 2322–2332.
164 A. R. Hillman, M. A. Mohamoud and I. Efimov, *Anal. Chem.*, 2011, **83**, 5696–5707.
165 D. Johannsmann, *Fundamentals and modeling*, Springer International Publishing, Switzerland, 2015.
166 A. R. Hillman, I. Efimov and M. Skompska, *Faraday Discuss.*, 2002, **121**, 423–439.
167 F. Höök, B. Kasemo, T. Nylander, C. Fant, K. Sott and H. Elwing, *Anal. Chem.*, 2001, **73**, 5796–5804.
168 N. Shpigel, M. D. Levi, S. Sigalov, O. Girshevitz, D. Aurbach, L. Daikhin, P. Pikma, M. Marandi, A. Jänes and E. Lust, *Nat. Mater.*, 2016, **15**, 570.
169 N. Shpigel, S. Sigalov, M. D. Levi, T. Mathis, L. Daikhin, A. Janes, E. Lust, Y. Gogotsi and D. Aurbach, *Joule*, 2018, **2**, 988–1003.
170 N. Jäckel, V. Dargel, N. Shpigel, S. Sigalov, M. D. Levi, L. Daikhin, D. Aurbach and V. Presser, *J. Power Sources*, 2017, **371**, 162–166.
171 N. Shpigel, M. R. Lukatskaya, S. Sigalov, C. E. Ren, P. Nayak, M. D. Levi, L. Daikhin, D. Aurbach and Y. Gogotsi, *ACS Energy Lett.*, 2017, **2**, 1407–1415.
172 S. Bourkane, C. Gabrielli and M. Keddam, *Electrochim. Acta*, 1989, **34**, 1081–1092.
173 F. Escobar-Teran, A. Arnau, J. Garcia, Y. Jiménez, H. Perrot and O. Sel, *Electrochem. Commun.*, 2016, **70**, 73–77.
174 C. Gabrielli, J. J. García-Jareño, M. Keddam, H. Perrot and F. Vicente, *J. Phys. Chem. B*, 2002, **106**, 3182–3191.
175 C. Gabrielli, M. Keddam, N. Nadi and H. Perrot, *J. Electroanal. Chem.*, 2000, **485**, 101–113.
176 T. Le, D. Aradilla, G. Bidan, F. Billon, M. Delaunay, J.-M. Gérard, H. Perrot and O. Sel, *Electrochem. Commun.*, 2018, **93**, 5–9.
177 R. K. Harris, T. V. Thompson, P. R. Norman, C. Pottage and A. N. Trethewey, *J. Chem. Soc., Faraday Trans.*, 1995, **91**, 1795–1799.
178 R. K. Harris, T. V. Thompson, P. R. Norman and C. Pottage, *J. Chem. Soc., Faraday Trans.*, 1996, **92**, 2615–2618.
179 R. K. Harris, T. V. Thompson, P. R. Norman and C. Pottage, *Carbon*, 1999, **37**, 1425–1430.
180 H. Wang, T. K. J. Köster, N. M. Trease, J. Ségalini, P.-L. Taberna, P. Simon, Y. Gogotsi and C. P. Grey, *J. Am. Chem. Soc.*, 2011, **133**, 19270–19273.
181 P. Ren, A. Zheng, X. Pan, X. Han and X. Bao, *J. Phys. Chem. C*, 2013, **117**, 23418–23424.
182 A. C. Forse, J. M. Griffin, V. Presser, Y. Gogotsi and C. P. Grey, *J. Phys. Chem. C*, 2014, **118**, 7508–7514.
183 D. Sebastiani, *ChemPhysChem*, 2006, **7**, 164–175.
184 M. Kibalchenko, M. C. Payne and J. R. Yates, *ACS Nano*, 2010, **5**, 537–545.
185 J. M. Griffin, A. C. Forse, W.-Y. Tsai, P.-L. Taberna, P. Simon and C. P. Grey, *Nat. Mater.*, 2015, **14**, 812–819.
186 S.-I. Lee, K. Saito, K. Kanehashi, M. Hatakeyama, S. Mitani, S.-H. Yoon, Y. Korai and I. Mochida, *Carbon*, 2006, **44**, 2578–2586.
187 M. Deschamps, E. Gilbert, P. Azais, E. Raymundo-Piñero, M. R. Ammar, P. Simon, D. Massiot and F. Béguin, *Nat. Mater.*, 2013, **12**, 351.
188 F. Blanc, M. Leskes and C. P. Grey, *Acc. Chem. Res.*, 2013, **46**, 1952–1963.
189 H. Wang, A. C. Forse, J. M. Griffin, N. M. Trease, L. Trognko, P.-L. Taberna, P. Simon and C. P. Grey, *J. Am. Chem. Soc.*, 2013, **135**, 18968–18980.
190 A. C. Forse, J. M. Griffin, C. Merlet, J. Carretero-Gonzalez, A.-R. O. Raji, N. M. Trease and C. P. Grey, *Nat. Energy*, 2017, **2**, 16216.
191 H. D. Bale and P. W. Schmidt, *Phys. Rev. Lett.*, 1984, **53**, 596.
192 L. Feigin and D. I. Svergun, *Structure analysis by small-angle X-ray and neutron scattering*, Springer, 1987.
193 M. Gardner, A. North, J. C. Dore, C. S.-M. de Lecea and D. Cazorla-Amoros, *Studies in Surface Science and Catalysis*, Elsevier, 1994, vol. 87, pp. 273–281.
194 D. Lozano-Castelló, E. Raymundo-Piñero, D. Cazorla-Amorós, A. Linares-Solano, M. Müller and C. Riekel, *Carbon*, 2002, **40**, 2727–2735.
195 D. Lozano-Castelló, D. Cazorla-Amorós, A. Linares-Solano, P. J. Hall, D. Gascon and C. Galan, *Carbon*, 2001, **39**, 1343–1354.
196 J. Calo and P. Hall, *Carbon*, 2004, **42**, 1299–1304.
197 D. Stevens and J. Dahn, *J. Electrochem. Soc.*, 2000, **147**, 4428–4431.
198 F. Ehrburger-Dolle, I. Morfin, E. Geissler, F. Bley, F. Livet, C. Vix-Guterl, S. Saadallah, J. Parmentier, M. Reda and J. Patarin, *Langmuir*, 2003, **19**, 4303–4308.
199 R. Kyutt, E. Smorgonskaya, A. Danishevskii, S. Gordeev and A. Grechinskaya, *Phys. Solid State*, 1999, **41**, 1359–1363.
200 T. Iiyama, Y. Kobayashi, K. Kaneko and S. Ozeki, *Colloids Surf., A*, 2004, **241**, 207–213.
201 T. Ohba, T. Omori, H. Kanoh and K. Kaneko, *J. Phys. Chem. B*, 2004, **108**, 27–30.
202 P. Ruch, M. Hahn, D. Cericola, A. Menzel, R. Kötz and A. Wokaun, *Carbon*, 2010, **48**, 1880–1888.
203 J. L. Bañuelos, G. Feng, P. F. Fulvio, S. Li, G. Rother, S. Dai, P. T. Cummings and D. J. Wesolowski, *Chem. Mater.*, 2013, **26**, 1144–1153.

204 R. Futamura, T. Iiyama, Y. Takasaki, Y. Gogotsi, M. J. Biggs, M. Salanne, J. Ségalini, P. Simon and K. Kaneko, *Nat. Mater.*, 2017, 1225–1232.
205 C. Prehal, D. Weingarth, E. Perre, R. T. Lechner, H. Amenitsch, O. Paris and V. Presser, *Energy Environ. Sci.*, 2015, **8**, 1725–1735.
206 P. Debye, H. Anderson Jr and H. Brumberger, *J. Appl. Phys.*, 1957, **28**, 679–683.
207 O. Glatter and O. Kratky, *Small angle X-ray scattering*, Academic Press, 1982.
208 C. Pings and J. Waser, *J. Chem. Phys.*, 1968, **48**, 3016–3018.
209 D. Saurel, J. Segalini, M. Jauregui, A. Pendashteh, B. Daffos, P. Simon and M. Casas-Cabanas, *Energy Storage Mater.*, 2019, **21**, 162–173.
210 C. Koczwara, C. Prehal, S. Haas, P. Boesecke, N. Huesing and O. Paris, *ACS Appl. Mater. Interfaces*, 2019, **11**, 42214–42220.
211 P. J. Hall, S. Brown, J. Fernandez and J. Calo, *Carbon*, 2000, **38**, 1257.
212 J. S. Gethner, *J. Appl. Phys.*, 1986, **59**, 1068–1085.
213 H. B. Stuhrmann, *Acta Crystallogr., Sect. A: Found. Crystallogr.*, 2008, **64**, 181–191.
214 K. Yurekli, C. A. Mitchell and R. Krishnamoorti, *J. Am. Chem. Soc.*, 2004, **126**, 9902–9903.
215 S. Boukhalfa, L. He, Y. B. Melnichenko and G. Yushin, *Angew. Chem., Int. Ed.*, 2013, **52**, 4618–4622.
216 S. Boukhalfa, D. Gordon, L. He, Y. B. Melnichenko, N. Nitta, A. Magasinski and G. Yushin, *ACS Nano*, 2014, **8**, 2495–2503.
217 A. Sharma, T. Kyotani and A. Tomita, *Carbon*, 2000, **38**, 1977–1984.
218 H. Takagi, K. Maruyama, N. Yoshizawa, Y. Yamada and Y. Sato, *Fuel*, 2004, **83**, 2427–2433.
219 K. Xia, Q. Gao, J. Jiang and J. Hu, *Carbon*, 2008, **46**, 1718–1726.
220 F. Fina, S. K. Callear, G. M. Carins and J. T. Irvine, *Chem. Mater.*, 2015, **27**, 2612–2618.
221 A. Thess, R. Lee, P. Nikolaev, H. Dai, P. Petit, J. Robert, C. Xu, Y. H. Lee, S. G. Kim and A. G. Rinzler, *Science*, 1996, **273**, 483–487.
222 T. Ohkubo, T. Iiyama, K. Nishikawa, T. Suzuki and K. Kaneko, *J. Phys. Chem. B*, 1999, **103**, 1859–1863.
223 M. Fukano, T. Fujimori, J. Segalini, E. Iwama, P.-L. Taberna, T. Iiyama, T. Ohba, H. Kanoh, Y. Gogotsi and P. Simon, *J. Phys. Chem. C*, 2013, **117**, 5752–5757.
224 F. W. Richey and Y. A. Elabd, *J. Phys. Chem. Lett.*, 2012, **3**, 3297–3301.
225 M. Osawa and M. Ikeda, *J. Phys. Chem.*, 1991, **95**, 9914–9919.
226 M. Osawa, K.-I. Ataka, K. Yoshii and Y. Nishikawa, *Appl. Spectrosc.*, 1993, **47**, 1497–1502.
227 F. W. Richey, B. Dyatkin, Y. Gogotsi and Y. A. Elabd, *J. Am. Chem. Soc.*, 2013, **135**, 12818–12826.
228 F. W. Richey, C. Tran, V. Kalra and Y. A. Elabd, *J. Phys. Chem. C*, 2014, **118**, 21846–21855.
229 M. Hantel, V. Presser, R. Kötz and Y. Gogotsi, *Electrochem. Commun.*, 2011, **13**, 1221–1224.
230 M. M. Hantel, V. Presser, J. K. McDonough, G. Feng, P. T. Cummings, Y. Gogotsi and R. Kötz, *J. Electrochem. Soc.*, 2012, **159**, A1897–A1903.
231 M. Hantel, D. Weingarth and R. Kötz, *Carbon*, 2014, **69**, 275–286.
232 L.-H. Shao, J. Biener, D. Kramer, R. N. Viswanath, T. F. Baumann, A. V. Hamza and J. Weissmüller, *Phys. Chem. Chem. Phys.*, 2010, **12**, 7580–7587.
233 C. Koczwara, S. Rumswinkel, C. Prehal, N. Jäckel, M. S. Elsässer, H. Amenitsch, V. Presser, N. Hüsing and O. Paris, *ACS Appl. Mater. Interfaces*, 2017, **9**, 23319–23324.
234 N. Jäckel, S. Patrick Emge, B. Krüner, B. Roling and V. Presser, *J. Phys. Chem. C*, 2017, **121**, 19120–19128.
235 D. Moreno, Y. Bootwala, W.-Y. Tsai, Q. Gao, F. Shen, N. Balke, K. B. Hatzell and M. C. Hatzell, *Environ. Sci. Technol. Lett.*, 2018, **5**, 745–749.
236 J. Ming, Z. Cao, Q. Li, W. Wahyudi, W. Wang, L. Cavallo, K.-J. Park, Y.-K. Sun and H. N. Alshareef, *ACS Energy Lett.*, 2019, **4**, 1584–1593.
237 W.-Y. Tsai, J. Come, W. Zhao, R. Wang, G. Feng, B. P. Thapaliya, S. Dai, L. Collins and N. Balke, *Nano Energy*, 2019, **60**, 886–893.
238 S. Liu, J. Peng, L. Chen, P. Sebastián, J. M. Feliu, J. Yan and B. Mao, *Electrochim. Acta*, 2019, **309**, 11–17.
239 Y. Fu and A. V. Rudnev, *Curr. Opin. Electrochem.*, 2017, **1**, 59–65.
240 R. Wen, B. Rahn and O. M. Magnussen, *Angew. Chem., Int. Ed.*, 2015, **54**, 6062–6066.
241 J. H. Raberg, J. Vatamanu, S. J. Harris, C. H. M. van Oversteeg, A. Ramos, O. Borodin and T. Cuk, *J. Phys. Chem. Lett.*, 2019, **10**, 3381–3389.
242 A. J. Ilott, M. Mohammadi, H. J. Chang, C. P. Grey and A. Jerschow, *Proc. Natl. Acad. Sci. U. S. A.*, 2016, **113**, 10779–10784.
243 G. Oukali, E. Salager, M. R. Ammar, C.-E. Dutoit, V. Sarou-Kanian, P. Simon, E. Raymundo-Piñero and M. Deschamps, *ACS Nano*, 2019, **13**, 12810–12815.
244 J. Martí, G. Nagy, E. Guàrdia and M. C. Gordillo, *J. Phys. Chem. B*, 2006, **110**, 23987–23994.
245 S. A. Kislenko, I. S. Samoylov and R. H. Amirov, *Phys. Chem. Chem. Phys.*, 2009, **11**, 5584–5590.
246 H. Liu, C. J. Jameson and S. Murad, *Mol. Simul.*, 2008, **34**, 169–175.
247 J. Vatamanu, Z. Hu, D. Bedrov, C. Perez and Y. Gogotsi, *J. Phys. Chem. Lett.*, 2013, **4**, 2829–2837.
248 J. Vatamanu, M. Vatamanu and D. Bedrov, *ACS Nano*, 2015, **9**, 5999–6017.
249 J. Vatamanu, O. Borodin, M. Olguin, G. Yushin and D. Bedrov, *J. Mater. Chem. A*, 2017, **5**, 21049–21076.
250 Q. Shao, L. Huang, J. Zhou, L. Lu, L. Zhang, X. Lu, S. Jiang, K. E. Gubbins and W. Shen, *Phys. Chem. Chem. Phys.*, 2008, **10**, 1896–1906.
251 R. K. Kalluri, D. Konatham and A. Striolo, *J. Phys. Chem. C*, 2011, **115**, 13786–13795.
252 S. Kondrat and A. Kornyshev, *J. Phys.: Condens. Matter*, 2010, **23**, 022201.

253 S. Kondrat, N. Georgi, M. V. Fedorov and A. A. Kornyshev, *Phys. Chem. Chem. Phys.*, 2011, **13**, 11359–11366.
254 J. Palmer, A. Llobet, S.-H. Yeon, J. Fischer, Y. Shi, Y. Gogotsi and K. Gubbins, *Carbon*, 2010, **48**, 1116–1123.
255 H. Wang and L. Pilon, *J. Power Sources*, 2013, **221**, 252–260.
256 C. Merlet, C. Péan, B. Rotenberg, P. A. Madden, B. Daffos, P. L. Taberna, P. Simon and M. Salanne, *Nat. Commun.*, 2013, **4**, 2701.
257 J. Seebeck, P. Schiffels, S. Schweizer, J.-R. Hill and R. H. Meissner, *J. Phys. Chem. C*, 2020, **124**, 5515–5521.
258 Z. Ryu, J. Zheng, M. Wang and B. Zhang, *Carbon*, 1999, **37**, 1257–1264.
259 J. Jagiello and M. Thommes, *Carbon*, 2004, **42**, 1227–1232.
260 T. Centeno and F. Stoeckli, *Carbon*, 2010, **48**, 2478–2486.
261 X. Hu, M. Radosz, K. A. Cychosz and M. Thommes, *Environ. Sci. Technol.*, 2011, **45**, 7068–7074.
262 M. Sevilla, J. B. Parra and A. B. Fuertes, *ACS Appl. Mater. Interfaces*, 2013, **5**, 6360–6368.
263 K. T. Klasson, M. Uchimiya and I. M. Lima, *Chemosphere*, 2014, **111**, 129–134.
264 J.-P. Hansen and I. R. McDonald, *Theory of simple liquids: with applications to soft matter*, Academic Press, 2013.
265 G. Jeanmairet, M. Levesque and D. Borgis, *J. Chem. Phys.*, 2013, **139**, 154101.
266 Y. Liu, S. Zhao and J. Wu, *J. Chem. Theory Comput.*, 2013, **9**, 1896–1908.
267 R. Ramirez, R. Gebauer, M. Mareschal and D. Borgis, *Phys. Rev. E: Stat., Nonlinear, Soft Matter Phys.*, 2002, **66**, 031206.
268 R. Ramirez and D. Borgis, *J. Phys. Chem. B*, 2005, **109**, 6754–6763.
269 L. Gendre, R. Ramirez and D. Borgis, *Chem. Phys. Lett.*, 2009, **474**, 366–370.
270 S. Zhao, R. Ramirez, R. Vuilleumier and D. Borgis, *J. Chem. Phys.*, 2011, **134**, 194102.
271 M. Levesque, R. Vuilleumier and D. Borgis, *J. Chem. Phys.*, 2012, **137**, 034115.
272 G. Jeanmairet, M. Levesque, R. Vuilleumier and D. Borgis, *J. Phys. Chem. Lett.*, 2013, **4**, 619–624.
273 C. Zhan, M. R. Ceron, S. A. Hawks, M. Otani, B. C. Wood, T. A. Pham, M. Stadermann and P. G. Campbell, *Nat. Commun.*, 2019, **10**, 4858.
274 *The Monte Carlo Method*, ed. Y. A. Shreider, N. P. Buslenko, D. I. Golenko, I. M. Sobol and V. G. Sragovich, Pergamon, 1966, pp. 1–90.
275 K. Kiyohara and K. Asaka, *J. Chem. Phys.*, 2007, **126**, 214704.
276 R. Burt, G. Birkett and X. Zhao, *Phys. Chem. Chem. Phys.*, 2014, **16**, 6519–6538.
277 Y. Bu, T. Sun, Y. Cai, L. Du, O. Zhuo, L. Yang, Q. Wu, X. Wang and Z. Hu, *Adv. Mater.*, 2017, **29**, 1700470.
278 K.-L. Yang, S. Yiacoumi and C. Tsouris, *J. Chem. Phys.*, 2002, **117**, 8499–8507.
279 K. Kiyohara and K. Asaka, *J. Phys. Chem. C*, 2007, **111**, 15903–15909.
280 T. Ohba, S. Yamamoto, A. Takase, M. Yudasaka and S. Iijima, *Carbon*, 2015, **88**, 133–138.
281 S. Kondrat and A. A. Kornyshev, *Nanoscale Horiz.*, 2016, **1**, 45–52.
282 S. R. Varanasi, A. H. Farmahini and S. K. Bhatia, *J. Phys. Chem. C*, 2015, **119**, 28809–28818.
283 A. Hartel, *J. Phys.: Condens. Matter*, 2017, **29**, 423002.
284 M. Dudka, S. Kondrat, A. Kornyshev and G. Oshanin, *J. Phys.: Condens. Matter*, 2016, **28**, 464007.
285 D.-E. Jiang, Z. Jin and J. Wu, *Nano Lett.*, 2011, **11**, 5373–5377.
286 T. Ohba and K. Kaneko, *J. Phys. Chem. C*, 2013, **117**, 17092–17098.
287 J. M. Haile, *Molecular dynamics simulation: elementary methods*, Wiley, New York, 1992.
288 F.-R. C. Chang, N. Skipper and G. Sposito, *Langmuir*, 1998, **14**, 1201–1207.
289 G. Feng and P. T. Cummings, *J. Phys. Chem. Lett.*, 2011, **2**, 2859–2864.
290 C. Merlet, C. Péan, B. Rotenberg, P. A. Madden, P. Simon and M. Salanne, *J. Phys. Chem. Lett.*, 2012, **4**, 264–268.
291 P. M. Vora, P. Gopu, M. Rosario-Canales, C. R. Pérez, Y. Gogotsi, J. J. Santiago-Avilés and J. M. Kikkawa, *Phys. Rev. B: Condens. Matter Mater. Phys.*, 2011, **84**, 155114.
292 A. C. Forse, C. l. Merlet, J. M. Griffin and C. P. Grey, *J. Am. Chem. Soc.*, 2016, **138**, 5731–5744.
293 C. Merlet, B. Rotenberg, P. A. Madden, P.-L. Taberna, P. Simon, Y. Gogotsi and M. Salanne, *Nat. Mater.*, 2012, **11**, 306–310.
294 N. N. Rajput, J. Monk, R. Singh and F. R. Hung, *J. Phys. Chem. C*, 2012, **116**, 5169–5181.
295 S. Li, K. S. Han, G. Feng, E. W. Hagaman, L. Vlcek and P. T. Cummings, *Langmuir*, 2013, **29**, 9744–9749.
296 L. Xing, J. Vatamanu, O. Borodin and D. Bedrov, *J. Phys. Chem. Lett.*, 2013, **4**, 132–140.
297 J. N. Neal, K. L. Van Aken, Y. Gogotsi, D. J. Wesolowski and J. Wu, *Phys. Rev. Appl.*, 2017, **8**, 34018.
298 K. Xu, Z. Lin, C. Merlet, P. L. Taberna, L. Miao, J. Jiang and P. Simon, *ChemSusChem*, 2018, **11**, 1892–1899.
299 Y. M. Liu, C. Merlet and B. Smit, *ACS Cent. Sci.*, 2019, **5**, 1813–1823.
300 A. Belhboub, E. H. Lahrar, P. Simon and C. Merlet, *Electrochim. Acta*, 2019, **327**, 135022.
301 S. Kondrat, P. Wu, R. Qiao and A. A. Kornyshev, *Nat. Mater.*, 2014, **13**, 387.
302 O. N. Kalugin, V. V. Chaban, V. V. Loskutov and O. V. Prezhdo, *Nano Lett.*, 2008, **8**, 2126–2130.
303 C. Péan, B. Rotenberg, P. Simon and M. Salanne, *J. Power Sources*, 2016, **326**, 680–685.
304 T. Mo, S. Bi, Y. Zhang, V. Presser, X. Wang, Y. Gogotsi and G. Feng, *ACS Nano*, 2020, **14**, 2395–2403.
305 S. Delmerico and J. G. McDaniel, *Carbon*, 2020, **161**, 550–561.
306 S. Zhu, J. Li, L. Ma, C. He, E. Liu, F. He, C. Shi and N. Zhao, *Mater. Lett.*, 2018, **233**, 294–297.
307 H. Su, S. Lin, S. Deng, C. Lian, Y. Shang and H. Liu, *Nanoscale Adv.*, 2019, **1**, 2162–2166.
308 X. Zhang, X. Wang, L. Jiang, H. Wu, C. Wu and J. Su, *J. Power Sources*, 2012, **216**, 290–296.

309 A. Lewandowski, A. Olejniczak, M. Galinski and I. Stepniak, *J. Power Sources*, 2010, **195**, 5814–5819.
310 T. Cottineau, M. Toupin, T. Delahaye, T. Brousse and D. Bélanger, *Appl. Phys. A: Solids Surf.*, 2005, **82**, 599–606.
311 J. Suárez-Guevara, V. Ruiz and P. Gomez-Romero, *J. Mater. Chem. A*, 2014, **2**, 1014–1021.
312 V. Khomenko, E. Raymundo-Pinero, E. Frackowiak and F. Beguin, *Appl. Phys. A: Solids Surf.*, 2006, **82**, 567–573.
313 F. Wang, S. Xiao, Y. Hou, C. Hu, L. Liu and Y. Wu, *RSC Adv.*, 2013, **3**, 13059.
314 V. Khomenko, E. Raymundo-Piñero and F. Béguin, *J. Power Sources*, 2010, **195**, 4234–4241.
315 L. Demarconnay, E. Raymundo-Piñero and F. Béguin, *Electrochem. Commun.*, 2010, **12**, 1275–1278.
316 K. Fic, G. Lota, M. Meller and E. Frackowiak, *Energy Environ. Sci.*, 2012, **5**, 5842–5850.
317 L. Suo, O. Borodin, T. Gao, M. Olguin, J. Ho, X. Fan, C. Luo, C. Wang and K. Xu, *Science*, 2015, **350**, 938–943.
318 G. Hasegawa, K. Kanamori, T. Kiyomura, H. Kurata, T. Abe and K. Nakanishi, *Chem. Mater.*, 2016, **28**, 3944–3950.
319 D. Reber, R.-S. Kühnel and C. Battaglia, *Sustainable Energy Fuels*, 2017, **1**, 2155–2161.
320 X. Bu, L. Su, Q. Dou, S. Lei and X. Yan, *J. Mater. Chem. A*, 2019, **7**, 7541–7547.
321 Q. Dou, S. Lei, D.-W. Wang, Q. Zhang, D. Xiao, H. Guo, A. Wang, H. Yang, Y. Li, S. Shi and X. Yan, *Energy Environ. Sci.*, 2018, **11**, 3212–3219.
322 C. Cheng, G. Jiang, G. P. Simon, J. Z. Liu and D. Li, *Nat. Nanotechnol.*, 2018, **13**, 685.
323 B. Pal, S. Yang, S. Ramesh, V. Thangadurai and R. Jose, *Nanoscale Adv.*, 2019, **1**, 3807–3835.
324 P. Azaïs, L. Duclaux, P. Florian, D. Massiot, M.-A. Lillo-Rodenas, A. Linares-Solano, J.-P. Peres, C. Jehoulet and F. Béguin, *J. Power Sources*, 2007, **171**, 1046–1053.
325 M. Conte, *Fuel Cells*, 2010, **10**, 806–818.
326 B. Ricketts and C. Ton-That, *J. Power Sources*, 2000, **89**, 64–69.
327 P. Kurzweil and M. Chwistek, *J. Power Sources*, 2008, **176**, 555–567.
328 H. Gualous, R. Gallay, G. Alcicek, B. Tala-Ighil, A. Oukaour, B. Boudart and P. Makany, *Microelectron. Reliab.*, 2010, **50**, 1783–1788.
329 D. Cericola, R. Kötz and A. Wokaun, *J. Power Sources*, 2011, **196**, 3114–3118.
330 Y. Liu, B. Réty, C. M. Ghimbeu, B. Soucaze-Guillous, P.-L. Taberna and P. Simon, *J. Power Sources*, 2019, **434**, 226734.
331 D. E. Jiang, Z. Jin, D. Henderson and J. Wu, *J. Phys. Chem. Lett.*, 2012, **3**, 1727–1731.
332 R. Lin, P. Huang, J. Segalini, C. Largeot, P.-L. Taberna, J. Chmiola, Y. Gogotsi and P. Simon, *Electrochim. Acta*, 2009, **54**, 7025–7032.
333 R. Lin, P. L. Taberna, J. Chmiola, D. Guay, Y. Gogotsi and P. Simon, *J. Electrochem. Soc.*, 2009, **156**, A7–A12.
334 C. Decaux, C. M. Ghimbeu, M. Dahbi, M. Anouti, D. Lemordant, F. Beguin, C. Vix-Guterl and E. Raymundo-Pinero, *J. Power Sources*, 2014, **263**, 130–140.
335 T. Husch, N. D. Yilmazer, A. Balducci and M. Korth, *Phys. Chem. Chem. Phys.*, 2015, **17**, 3394–3401.
336 C. Schütter, T. Husch, M. Korth and A. Balducci, *J. Phys. Chem. C*, 2015, **119**, 13413–13424.
337 C. Schütter, T. Husch, V. Viswanathan, S. Passerini, A. Balducci and M. Korth, *J. Power Sources*, 2016, **326**, 541–548.
338 J. Krummacher, C. Schütter, S. Passerini and A. Balducci, *ChemElectroChem*, 2017, **4**, 353–361.
339 C. Schütter, S. Passerini, M. Korth and A. Balducci, *Electrochim. Acta*, 2017, **224**, 278–284.
340 K. R. Seddon, *J. Chem. Technol. Biotechnol.*, 1997, **68**, 351–356.
341 M. Ue and M. Takeda, *J. Korean Electrochem. Soc.*, 2002, **5**, 192–196.
342 M. Galiński, A. Lewandowski and I. Stępniak, *Electrochim. Acta*, 2006, **51**, 5567–5580.
343 K. Yuyama, G. Masuda, H. Yoshida and T. Sato, *J. Power Sources*, 2006, **162**, 1401–1408.
344 A. Balducci, R. Dugas, P.-L. Taberna, P. Simon, D. Plee, M. Mastragostino and S. Passerini, *J. Power Sources*, 2007, **165**, 922–927.
345 C. Arbizzani, M. Biso, D. Cericola, M. Lazzari, F. Soavi and M. Mastragostino, *J. Power Sources*, 2008, **185**, 1575–1579.
346 A. Brandt and A. Balducci, *J. Power Sources*, 2014, **250**, 343–351.
347 V. Ruiz, T. Huynh, S. R. Sivakkumar and A. G. Pandolfo, *RSC Adv.*, 2012, **2**, 5591.
348 J. Wang, H. Tang, L. Zhang, H. Ren, R. Yu, Q. Jin, J. Qi, D. Mao, M. Yang, Y. Wang, P. Liu, Y. Zhang, Y. Wen, L. Gu, G. Ma, Z. Su, Z. Tang, H. Zhao and D. Wang, *Nat. Energy*, 2016, **1**, 16050.
349 E. Frackowiak, G. Lota and J. Pernak, *Appl. Phys. Lett.*, 2005, **86**, 164104.
350 A. Krause and A. Balducci, *Electrochem. Commun.*, 2011, **13**, 814–817.
351 A. Brandt, C. Ramirez-Castro, M. Anouti and A. Balducci, *J. Mater. Chem. A*, 2013, **1**, 12669.
352 K. N. Marsh, J. A. Boxall and R. Lichtenthaler, *Fluid Phase Equilib.*, 2004, **219**, 93–98.
353 H. Kurig, M. Vestli, A. Jänes and E. Lust, *Electrochem. Solid-State Lett.*, 2011, **14**, A120.
354 H. Lu, L. He, X. Li, W. Zhang, J. Che, X. Liu, Z. Hou, H. Du and Y. Qu, *J. Mater. Sci.: Mater. Electron.*, 2019, **30**, 13933–13938.
355 C. Lian, K. Liu, K. L. Van Aken, Y. Gogotsi, D. J. Wesolowski, H. L. Liu, D. E. Jiang and J. Z. Wu, *ACS Energy Lett.*, 2016, **1**, 21–26.
356 M. W. Thompson, R. Matsumoto, R. L. Sacci, N. C. Sanders and P. T. Cummings, *J. Phys. Chem. B*, 2019, **123**, 1340–1347.
357 R.-S. Kühnel, S. Obeidi, M. Lübke, A. Lex-Balducci and A. Balducci, *J. Appl. Electrochem.*, 2013, **43**, 697–704.
358 C. Lian, H. Liu, C. Li and J. Wu, *AIChE J.*, 2019, **65**, 804–810.
359 S. Perkin, M. Salanne, P. Madden and R. Lynden-Bell, *Proc. Natl. Acad. Sci. U. S. A.*, 2013, **110**, E4121–E4121.

360 B. Skinner, M. Loth and B. Shklovskii, *Phys. Rev. Lett.*, 2010, **104**, 128302.
361 Z. A. Goodwin and A. A. Kornyshev, *Electrochem. Commun.*, 2017, **82**, 129–133.
362 M. A. Gebbie, A. M. Smith, H. A. Dobbs, G. G. Warr, X. Banquy, M. Valtiner, M. W. Rutland, J. N. Israelachvili, S. Perkin and R. Atkin, *Chem. Commun.*, 2017, **53**, 1214–1224.
363 K. Ma, C. Lian, C. E. Woodward and B. Qin, *Chem. Phys. Lett.*, 2020, **739**, 137001.
364 A. C. Forse, J. M. Griffin, C. L. Merlet, P. M. Bayley, H. Wang, P. Simon and C. P. Grey, *J. Am. Chem. Soc.*, 2015, **137**, 7231–7242.
365 X. Wang, H. Zhou, E. Sheridan, J. C. Walmsley, D. Ren and D. Chen, *Energy Environ. Sci.*, 2016, **9**, 232–239.
366 J. N. Neal, D. J. Wesolowski, D. Henderson and J. Wu, *J. Chem. Phys.*, 2017, **146**, 174701.
367 T. Brousse, D. Bélanger and J. W. Long, *J. Electrochem. Soc.*, 2015, **162**, A5185–A5189.
368 P. Simon, Y. Gogotsi and B. Dunn, *Science*, 2014, **343**, 1210–1211.
369 B. E. Conway, *J. Electrochem. Soc.*, 1991, **138**, 1539–1548.
370 K. Fic, E. Frackowiak and F. Béguin, *J. Mater. Chem.*, 2012, **22**, 24213–24223.
371 B. Akinwolemiwa, C. Peng and G. Z. Chen, *J. Electrochem. Soc.*, 2015, **162**, A5054–A5059.
372 G. Lota, K. Fic and E. Frackowiak, *Electrochem. Commun.*, 2011, **13**, 38–41.
373 G. Lota and E. Frackowiak, *Electrochem. Commun.*, 2009, **11**, 87–90.
374 S. Roldán, M. Granda, R. Menéndez, R. Santamaría and C. Blanco, *J. Phys. Chem. C*, 2011, **115**, 17606–17611.
375 S. Roldán, C. Blanco, M. Granda, R. Menéndez and R. Santamaría, *Angew. Chem., Int. Ed.*, 2011, **50**, 1699–1701.
376 S. Senthilkumar, R. K. Selvan and J. Melo, *J. Mater. Chem. A*, 2013, **1**, 12386–12394.
377 S. Senthilkumar, R. K. Selvan, N. Ponpandian, J. Melo and Y. Lee, *J. Mater. Chem. A*, 2013, **1**, 7913–7919.
378 S. Senthilkumar, R. K. Selvan, Y. Lee and J. Melo, *J. Mater. Chem. A*, 2013, **1**, 1086–1095.
379 B. Gorska, E. Frackowiak and F. Beguin, *Curr. Opin. Electrochem.*, 2018, **9**, 95–105.
380 S. Sathyamoorthi, V. Suryanarayanan and D. Velayutham, *J. Power Sources*, 2015, **274**, 1135–1139.
381 H. J. Xie, B. Gélinas and D. Rochefort, *Electrochem. Commun.*, 2016, **66**, 42–45.
382 E. Mourad, L. Coustan, P. Lannelongue, D. Zigah, A. Mehdi, A. Vioux, S. A. Freunberger, F. Favier and O. Fontaine, *Nat. Mater.*, 2017, **16**, 446–453.
383 E. Mourad, L. Coustan, S. A. Freunberger, A. Mehdi, A. Vioux, F. Favier and O. Fontaine, *Electrochim. Acta*, 2016, **206**, 513–523.
384 O. Fontaine, *Energy Storage Mater.*, 2019, **21**, 240–245.
385 C. Bodin, E. Mourad, D. Zigah, S. Le Vot, S. A. Freunberger, F. Favier and O. Fontaine, *Faraday Discuss.*, 2018, **206**, 393–404.
386 K. Wang, J. Wang, S. Zhao, Z. Wang and S. Wang, *J. Power Sources*, 2019, **434**, 226745.
387 Y. Yoon, W. Cho, J. Lim and D. J. Choi, *J. Power Sources*, 2001, **101**, 126–129.
388 P. Sivaraman, V. Hande, V. Mishra, C. S. Rao and A. Samui, *J. Power Sources*, 2003, **124**, 351–354.
389 K. Wang, W. Zou, B. Quan, A. Yu, H. Wu, P. Jiang and Z. Wei, *Adv. Energy Mater.*, 2011, **1**, 1068–1072.
390 H. Gao and K. Lian, *RSC Adv.*, 2014, **4**, 33091–33113.
391 L. Nègre, B. Daffos, P.-L. Taberna and P. Simon, *J. Electrochem. Soc.*, 2015, **162**, A5037–A5040.
392 A. A. Łatoszyńska, G. Z. Żukowska, I. A. Rutkowska, P.-L. Taberna, P. Simon, P. J. Kulesza and W. Wieczorek, *J. Power Sources*, 2015, **274**, 1147–1154.
393 X. Peng, H. Liu, Q. Yin, J. Wu, P. Chen, G. Zhang, G. Liu, C. Wu and Y. Xie, *Nat. Commun.*, 2016, **7**, 11782.
394 B. Hsia, S. Wang, M.-S. Kim, C. Carraro and R. Maboudian, All solid-state micro-supercapacitors using ionogel electrolyte, 2013 Transducers & Eurosensors XXVII: The 17th International Conference on Solid-State Sensors, Actuators and Microsystems (TRANSDUCERS & EUROSENSORS, XXVII), Barcelona, 2013, pp. 1328–1331.
395 L. Yu and G. Z. Chen, *Front. Chem.*, 2019, **7**, 272.
396 L. Nègre, B. Daffos, V. Turq, P.-L. Taberna and P. Simon, *Electrochim. Acta*, 2016, **206**, 490–495.
397 S. Alipoori, S. Mazinani, S. H. Aboutalebi and F. Sharif, *J. Energy Storage*, 2020, **27**, 101072.
398 C. Yin, X. Liu, J. Wei, R. Tan, J. Zhou, M. Ouyang, H. Wang, S. J. Cooper, B. Wu, C. George and Q. Wang, *J. Mater. Chem. A*, 2019, **7**, 8826–8831.
399 B. Xu, H. Wang, Q. Zhu, N. Sun, B. Anasori, L. Hu, F. Wang, Y. Guan and Y. Gogotsi, *Energy Storage Mater.*, 2018, **12**, 128–136.
400 L. Yu, L. Hu, B. Anasori, Y.-T. Liu, Q. Zhu, P. Zhang, Y. Gogotsi and B. Xu, *ACS Energy Lett.*, 2018, **3**, 1597–1603.